UNIVERSITY OF SOUTHAMPTON

AN INTERFEROMETRIC MEASUREMENT OF THE 1S-2S TRANSITION FREQUENCY IN ATOMIC HYDROGEN.

BY

JOHN RICHARD MCALPINE BARR.

MAY 1986

Contents.

Contents Page

1. Introduction.

Contents.

Contents.

Contents.

UNIVERSITY OF SOUTHAMPTON

ABSTRACT

FACULTY OF SCIENCE

PHYSICS

Doctor of Philosophy

AN INTERFEROMETRIC MEASUREMENT OF THE 1S-2S TRANSITION FREQUENCY IN ATOMIC HYDROGEN

by John Richard McAlpine Barr.

Two photon Doppler free laser spectroscopy has been used to measure the $1S_{\frac{1}{2}}-2S_{\frac{1}{2}}$ transition frequency in atomic hydrogen by interferometric comparison with a reference line in $^{130}Te_2$. The measured $1S_{\frac{1}{2}}-2S_{\frac{1}{2}}$ transition frequency of 2 466 061 397 (25) MHz is in good agreement with the theoretical value 2 466 061 405.5 (2.9) MHz. This measurement can be used to deduce a value for the ground state Lamb shift giving 8182(25) MHz, which may be compared with a theoretical value 8173.248(81) MHz. Alternatively a value of the Rydberg constant can be deduced as 10 973 731.50 (11) m^{-1} which is consistent with other measurements but with a slightly larger uncertainty. This is the first time that the Rydberg constant has been measured on a transition in atomic hydrogen other than Balmer α using techniques of laser spectroscopy.

Acknowledgements.

I would like to thank all those who have assisted me during the course of my postgradute work. My supervisor, Dr. A.I. Ferguson, who stimulated my interest in the spectroscopy of hydrogen and allowed me to carry out this work. The other members of the laser group, in particular I. Alcock, S. Bramwell, J.M. Girkin, Dr. D.M. Kane and J.M. Tolchard, who made working at Southampton such a pleasure. The expert assistance of the electronic and mechanical workshops from R. Garnent, M. Finn, M. Hill and B. Heath is gratefully acknowledged. Finally I would like to thank my wife Rebecca for typing this manuscript.

Chapter 1. Introduction.

Ever since Rydberg described the relatively simple hydrogen spectral line structure using an empirical formula in 1889, hydrogen has been used to test and refine theories of atomic structure. The major discovery which stimulated the development of quantum electrodynamics (QED) was the observation of the Lamb shift by Lamb and Retherford in 1947 [1]. The agreement between QED and experiment is impressive; nevertheless, in experiments where the accuracy is comparable with the theoretical calculations, some discrepancies do remain [2,3,4,5].

Until the early seventies, experiments which achieved accuracies approaching the theoretical values were mainly limited to examining fine structure transitions. For example, Lamb and Retherford [1] measured the $2P_{1/2}-2S_{1/2}$ transition by applying a radio frequency electric field to a beam of metastable H atoms. This method works well for all fine structure levels with principle quantum numbers n=2 and greater. The ground state of hydrogen, being an S state, has a large Lamb shift, but since there is no adjacent P state the methods of radio-frequency spectroscopy cannot be applied. The first attempt to measure the ground state Lamb shift was carried out by Herzberg [6] in 1956. The wavelength of the 1S-2P transition in deuterium was measured; the precision was severely limited by the large Doppler width of this transition. (The results of this and other Lamb shift measurements are detailed in Appendix A). A resolution of 1.3 parts in 10 was obtained which has to be compared with a resolution of 2 parts in 10^5 achieved in the most recent $2P_{\frac{1}{2}}-2S_{\frac{1}{2}}$ measurements.

Since the early seventies, laser systems which can be used in high precision measurements in hydrogen have been under continuous development. These measurements were pioneered by Hänsch [7]. The initial experiments determined the ground state Lamb shift by comparing one quarter of the 1S-2S frequency with one of the n=2, n=4 Balmer β transitions [7,8]. This can be done conveniently since the 1S-2S transition is a two photon transition requiring light at 243 nm which can be generated by frequency doubling 486 nm light. Since the hydrogen atom energy levels scale as n^{-2}, the 486 nm light can be used to perform a single photon experiment on the Balmer β transition. The 1S-2S transition was suggested as an interesting candidate for high resolution Doppler free spectroscopy by Baklanov and Chebotaev [9].

It is useful to consider why this approach was adopted. In all measurements where a theory is compared with experiment, the theoretical value has two sources of uncertainty. The first contribution is due to the approximations made in deriving the relevant result. For QED this is at the few parts in 10^{11} level for the 1S-2S transition frequency or 1.3 parts in 10^5 for the ground state Lamb shift [2]. These uncertainties are only estimates based on the order of magnitude of uncalculated terms. If the experimental aim is to measure fundamental constants, for example the Rydberg constant, then ideally the QED uncertainty should be small compared with the experimental constants used in numerical evaluations. For the 1S-2S transition this is indeed the case. The predominant uncertainty arises from the Rydberg constant, which is at present known to 1 part in 10^9 [10,11,12,13]. Using this value the 1S-2S frequency can be calculated to ±2.5 MHz. Measuring the 1S-2S frequency to this precision or better would only enable the Lamb shift to be determined to ±2.5 MHz or 3 parts in 10^4. However, in the early seventies when this series of experiments commenced, the Rydberg constant had not yet been measured accurately using laser spectroscopic techniques and was only known to 8 parts in 10^8 giving an uncertainty in a calculation of the 1S-2S frequency of ±197 MHz [9]. The comparison method outlined above involves the difference between two transitions, one quarter of the 1S-2S frequency and one of the Balmer β lines. This small difference can be calculated theoretically and is effected by the uncertainty in the Rydberg constant to 8 parts in 10^8 if the Cohen and Taylor value of the Rydberg is used [10]. This is to be compared with the uncertainty in the QED calculations for the ground state Lamb shift of 1 part in 10^5, which is larger than the uncertainty due to the fundamental constants. So for this case the theoretical uncertainty is larger than the experimental contribution to the uncertainty and the experiment could provide a stringent test of theory. Another more practical reason for using the comparison method is that determining the ground state Lamb shift by measuring the absolute 1S-2S frequency requires a frequency standard for comparision. This was not available at the time. The development of a suitable standard is discussed in Chapter 4.

There are other reasons, in addition to testing QED by measuring the ground state Lamb shift, why the 1S-2S frequency is of interest to physicists. The 2S level is well known to be metastable with a lifetime of approximately 1/7 s [9,14] which implies a natural lifetime of 1 Hz. This feature makes it very attractive to metrologists who are interested in measuring fundamental constants since it predicts an ideal resolution of a few parts in 10^{14}. This is far narrower than the linewidth of the Balmer α transitions in hydrogen which have been used for measuring the Rydberg constant. The most recent Rydberg measurement involved locating the centre of the 2S-3P transitions which have a linewidth of about 50 MHz to within one hundredth of that width [13]. If the 1S-2S transition frequency can be measured to better than ± 2.5 MHz then the Rydberg constant can be used as an adjustable parameter in the QED expression in order to obtain a better value. This would provide a check on both the internal consistency of QED calculations and also on systematic errors that may exist in Rydberg constant measurements since the constant has only been measured on the Balmerα transitions using techniques of laser spectroscopy. Additionally, a comparison between the deuterium and hydrogen 1S-2S frequencies could provide information on the ratio of the mass of the electron to the mass of the proton via the isotope shift [8].

The importance of measurements on hydrogen cannot be too highly stressed. It provides a dual role whereby theory can be tested and fundamental constants measured. To meet this twofold aim the transition frequencies of various levels should be determined so that there are more results than adjustable parameters. There are a variety of measurements in progress throughout the world.

1.1. $2S_{\frac{1}{2}}-4P_{\frac{1}{2},\frac{3}{2}}$ Balmerβ transitions.

Examination of the Balmerβ transitions using laser spectroscopy requires H atoms prepared in the metastable 2S level. The simplest method is to dissociate the molecular hydrogen in a Woods discharge [7] and probe the Balmerβ transitions in the discharge environment. This can lead to systematic energy level shifts due to the electric field in the discharge which can be difficult to measure and control

[7,8]. To avoid this problem metastable hydrogen beams can be used which enable spatial separation of the dissociation discharge, excitation to the 2S level and the interaction regions. The influence of strong electric fields can be reduced which simplifies the experimental analysis.

A metastable atomic hydrogen is under construction at Southampton. This will be used in an experiment designed to measure the absolute frequency of the $2S_{\frac{1}{2}}-4P_{\frac{1}{2}},_{\frac{3}{2}}$ transitions. The frequency standard used in this experiment will be $^{130}Te_2$ vapour as described in Chapter 4 [15]. Ultimately this could lead to a Rydberg constant measurement. The Balmer β transitions are more attractive than the Balmer α since the natural linewidth is 13 MHz as opposed to 30 MHz, [16]. Alternatively, the frequency of the $2S_{\frac{1}{2}}-4P_{\frac{1}{2}},_{\frac{3}{2}}$ could be compared with one quarter of the 1S-2S frequency in order to measure the ground state Lamb shift using the comparison method.

1.2. $2S_{\frac{1}{2}}-8S_{\frac{1}{2}},8D_{\frac{3}{2}},_{\frac{5}{2}}$ two photon transitions.

Another interesting experiment makes use of the very narrow linewidths possible in transitions to Rydberg states in hydrogen. The $2S_{\frac{1}{2}}-8S_{\frac{1}{2}},8D_{\frac{3}{2}},_{\frac{5}{2}}$ transitions have been observed with linewidths of the order of 3 MHz in a metastable atomic hydrogen beam [17]. It is intended to make a measurement of the Rydberg constant in this experiment. One of the fundamental problems to be overcome in using this type of system to measure fundamental constants is its extreme sensitivity to the D.C. Stark shifts. For example, a field of 50 mV/cm causes a shift of -3 MHz in this experiment which must be compared with a field of 50 V/cm in the case of 1S-2S transition (see Chapter 3).

1.3. Double quantum excitation of the $2S_{\frac{1}{2}}-3S_{\frac{1}{2}}$ transition.

One method to reduce the large Balmer α linewidth mentioned in 1.1. is to use a double quantum method with one optical photon and one r.f. photon [18]. The natural linewidth is expected to be about 1 MHz. This experiment is in an early stage and the measured linewidth is about 20 MHz. Again the aim is to measure the Rydberg constant.

1.4. C.W. excitation of the $1S_{1/2}-2S_{1/2}$ transition.

There are at least two independent schemes for producing c.w. 243 nm radiation for a 1S-2S experiment. One method involves mixing light at 351 nm from an argon ion laser with light from a 790 nm dye laser in potassium dihydrogen phosphate (K.D.P.),[19]. This method has resulted in 1-2 mw of 243 nm light which has been enhanced by a factor of 10 using a resonant cavity about the H cell. Linewidths of 8 MHz at 243 nm have been observed. However, no measurements have been reported with this system.

One method of overcoming the low efficiency of frequency doubling c.w. 486 nm light is to place the doubling crystal within the laser cavity [20]. This is limited by poor beam quality and optical damage to the doubling crystal. No measurements on hydrogen have been reported yet.

1.5. Pulsed excitation of the $1S_{\frac{1}{2}}$-$2S_{\frac{1}{2}}$ transition.

An experiment which is similar to the one described in this thesis is underway at Stanford University. Recent results seem to be slightly more accurate than the values obtained here [21,22].

In both experiments pulsed amplification of c.w. light at 486 nm was used to overcome the low efficiency frequency doubling of c.w. 486 nm light to 243 nm. To reduce the linewidth the pulsed output was passed through a confocal Fabry-Perot etalon stabilised to the c.w. light. Frequency doubling was carried out in urea and Doppler free two photon resonant three photon ionisation was used to observe the $1S_{\frac{1}{2}}$-$2S_{\frac{1}{2}}$ transition. Simultaneously a Doppler free saturated absorbtion experiment was carried out on $^{130}Te_2$

vapour and the frequency separation between a line of known frequency in the $^{130}Te_2$ spectrum and the hydrogen two photon resonance was measured. These measurement constitute the first frequency measurement of the $1S_{\frac{1}{2}}-2S_{\frac{1}{2}}$ transition in hydrogen.

2. Thesis outline.

The second and third chapters of this thesis deal with the hydrogen atom and its interaction with electromagnetic fields. The second chapter gives a simple outline of the present status of the theoretical predictions for the hydrogen energy levels. Detailed information is given for the structure of the 1S-2S transition. Finally the measurement described in this thesis is discussed and related to theory. In the third chapter the influence of external fields is examined. The basic question to be resolved here is how to relate the measured value of the 1S-2S transition which is made on a perturbed atom to a fictitious atom which is not influenced by external fields. Various numerical estimates are made.

The next three chapters discuss the experimental process in detail. Chapter 4 is devoted to the frequency standard. A brief description is given of the measurement of this frequency, which was made in conjunction with J. Girkin, and the National Physical Laboratory. Chapter 5 involves a detailed discussion of the laser system which was developed for this measurement. This includes the production of atomic hydrogen and the data collection methods. In Chapter 6 the results are analysed.

References are given after each chapter. This increases the ease by which entries of interest may be found. The appendices contain a large amount of information which, while not of immediate relevance to the main subject matter of this thesis, is of some interest if only for reference.

References.

[1] W. Lamb, R. Retherford. Phys. Rev. 72 241. (1947).

[2] G. Erickson. J. Phys. Chem. Ref. Data. 6 831. (1977).

[3] P. Mohr. Phys. Rev. Lett. 34 1050. (1975).

[4] S. Lundeen, F. Pipkin. Phys. Rev. Lett. 46 232. (1980).

[5] S. Sokolov, V. Yakovlev. Sov. Phys. J.E.T.P. 56 7. (1982).

[6] G. Herzberg. Proc. Roy. Soc. 234A 516. (1956).

[7] T.W. Hänsch, S.A. Lee, R. Wallenstein, C. Wieman. Phys. Rev. Lett. 34 307. (1975).

[8] C. Wieman, T.W. Hänsch. Phys. Rev. 22 192. (1980).

[9] E. Backlanov, V. Chebotaev. Opt. Spect. 38 215. (1975).

[10] E. Cohen, B. Taylor. J. Phys. Chem. Ref. Data. 2 663. (1973).

[11] J.E.M. Goldsmith, E.W. Weber, T.W. Hänsch. Phys. Rev Lett. 41 1525. (1978).

[12] B.W. Petley, K. Morris, R.E. Shawyer. J. Phys. B. 13 3099. (1980).

[13] S.R. Amin, C.D. Caldwell, W. Lichten, Phys. Rev. Lett. 47 1234. (1981).

[14] F.A. Parpia, W.R. Johnson. Phys. Rev. A. 26 1142. (1982).

Chapter 1.

[15] J.R.M. Barr, J.M. Girkin, A.I. Ferguson, G.P. Barwood, P. Gill, W.R.C. Rowley, R.C. Thompson. Opt. Comm. 54 217. (1985).

[16] H.Bethe, E.Saltpeter. "Quantum Mechanics of One- and Two- Electron Atoms". Plenum. (1977).

[17] F. Biraben, L. Julien. Opt. Comm. 53 319. (1985).

[18] D. Shiner, C. Wieman. "Precision Measurements and Fundamental Constants 11". p123. B. Taylor and W. Phillips Eds. Natl. Bur. Stand. (U.S.), Spec. Publ. 617. (1984).

[19] C.J. Foot, B. Couillaud, R. Beausoleil, T. Hänsch. Phys. Rev. Lett. 54 1913. (1985).

[20] C.J. Foot, P.E.G. Baird, M.G. Boshier, D.N. Stacey, G.K. Woodgate Opt. Comm. 50 199. (1984).

[21] E.A. Hildum, U. Boesl, D.H. McIntyre, R.G. Beausoleil, T.W. Hänsch. Phys. Rev. Lett. 56 576. (1986).

[22] J.R.M. Barr, J.M. Girkin, J.M. Tolchard, A.I. Ferguson. Phys. Rev. Lett. 56 580. (1986).

Chapter 2. The Lamb shift in hydrogen-like atoms.

This chapter discusses the energy levels of hydrogen-like atoms calculated by QED techniques [1], which apply to an unperturbed atom. In order to make a real measurement, the atom is of necessity perturbed in some manner by both the actions of the experimenter and the state in which the atom is prepared. An example of the former is the laser beam used to excite the atom, while the latter can occur through the presence of other hydrogen atoms in the gaseous sample used in the experiment. The small corrections caused by these perturbations are examined in Chapter 3.

A computer program has been written which enables the Lamb shift to be calculated for the levels of interest in hydrogen and deuterium. The program was initially written by Dr.J. Hey of Cape Town University and adapted and corrected by myself. This enables the effect of varying the values of fundamental constants to be examined simply. The constants used in the calculations are shown in Table 2.1. The program was used to generate the theoretical values for the Lamb shift quoted in this chapter. A listing of the program is given in Appendix A.

2.1. Dirac contribution to the energy levels of hydrogen-like atoms.

The Dirac contributions to the energy of one electron atoms arises from the use of a relativistically correct Hamiltonian [2]. The result, which is derived in any standard text, eg. [3], for an electron orbiting a fixed nucleus is:

$$\left(\frac{m_e}{\mu}\right) E_D(n,j) = m_e c^2 \left[1 + \left(\frac{\alpha Z}{n-(j+1/2)+\sqrt{(j+1/2)^2-\alpha^2 Z^2}} \right)^2 \right]^{-\frac{1}{2}} - m_e c^2$$

$$= -\frac{2hcR_\infty}{\alpha^2} \left[1 - \left\{ 1 + \left(\frac{\alpha Z}{n-(j+1/2)+\sqrt{(j+1/2)^2-\alpha^2 Z^2}} \right)^2 \right\}^{-\frac{1}{2}} \right]$$

(2.1,1)

where the alternative expression for the electron rest mass has been used to re-express $\left(\frac{m_e}{\mu}\right) E_D(n,j)$:

$$m_e c^2 = \frac{2hc}{\alpha^2}$$

Notice that the energy for a given principal quantum number n depends only on the total orbital angular momentum $j = \ell \pm \frac{1}{2}$ and not on the orbital angular momentum l. For the n=2 levels the fine structure splitting between the $2P_{\frac{3}{2}}$ and the $2S_{\frac{1}{2}}$, $2P_{\frac{1}{2}}$ states is correctly given (to this level of approximation) while the $2S_{\frac{1}{2}}$ and $2P_{\frac{1}{2}}$ levels are degenerate.

In practise the nucleus does not have an infinite mass and so is not fixed. In non-relativistic quantum theory this is taken account of by replacing m_e by μ, the reduced mass. This can be done formally by replacing m_e on the rhs of (2.1,1) by μ or replacing R_∞ by R_M . Such a procedure cannot be justified theoretically since the Dirac equation is not separable in terms of a reduced mass.

Table 2.1.

Rydberg Constant R_{∞} - 10973731 m^{-1}

Goldstein et. al.	[14]	0.500 (32)
Petley et. al.	[15]	0.521 (64)
Amin et. al.	[16]	0.539 (12)
Weighted average		0.534 (13)

Fine Structure Constant	137.035988 (10)
Proton electron mass ratio	1836.152 701 (37)
Radius of the proton	0.862 (12) fm

Values of the constants used in calculations relating to the energy levels of hydrogen. The values given (apart from the proton radius) were communicated by B.Taylor and arise from the most recent rationalisation of the fundamental constants [17].

A detailed discussion of this point is given in [1] and [2]. The following corrections have to be added to $E_D(n,j)$

{RM/n4} $$E_R(n,\ell,j) = -\frac{(Z\alpha)^4 \mu^2 c^2}{8n^4(M+m_e)} - \frac{\mu^2}{M^2}\frac{(Z\alpha)^4 \mu c^2}{2n^3}\frac{C_{\ell j}}{2\ell+1}(1-\delta_{\ell 0})$$

(2.1,2)

where

$$C_{\ell j} = \begin{cases} \frac{1}{\ell + 1/2} & j = \ell + 1/2 \\ -\frac{1}{\ell} & j = \ell - 1/2 \end{cases}$$

The second correction term only acts on non S states. The expression in curly brackets to the left of this and other equations gives the label under which the corrections are displayed in the program print out shown in Table 2.2. The labels are chosen for uniformity with Erickson's print outs. Notice that the degeneracy with respect to l of the Dirac energy levels is broken by the reduced mass correction although only slightly. The dominant l dependent correction is the Lamb shift which is discussed in the next section.

An additional recoil correction arises from a full co-variant calculation. Appendix A gives a complete account of all necessary corrections. Table 2.2 gives the Dirac energy differences $E_D(2,\frac{1}{2})-E_D(1,\frac{1}{2})$ for n=1,2 and $j=\frac{1}{2}$ for H.

Table 2.2 (a).

Dirac Contribution	-2467411574.203 MHz
Reduced Mass	+1343062.867 MHz
Nuclear Recoil {RM/N4}	-22.325 MHz
$1S_{\frac{1}{2}}$ Lamb Shift	-8173.248 MHz
$2S_{\frac{1}{2}}$ Lamb Shift	+1045.077 MHz

$1S_{\frac{1}{2}}$ $-2S_{\frac{1}{2}}$ Frequency	2466061405.5 (2.9) MHz

Contributions To The Lamb Shift (MHz).

	$1S_{\frac{1}{2}}$	$2S_{\frac{1}{2}}$
{IR LOG}	7925.168	1013.987
{MAG MOM}	406.266	50.783
{VAC POL}	-216.675	-27.084
{ZA}	55.177	6.897
{ZA2 LL}	-4.196	-0.524
{ZA2 L}	2.311	0.316
{ZA2 ETC}	-1.105	0.126
{(HTOT)}	52.187	6.562
{HO VP}	1.866	0.233
{A L}	3.554	0.444
{A MM}	-0.614	-0.076
{A VP}	-1.913	-0.239
{RM/BS}	2.409	0.341
{NUC STR}	0.998	0.124
{TOTAL}	8173.248(81)	1045.077(3)

Table 2.2 (b).

Hyperfine Splitting.

$1S_{\frac{1}{2}}$	1420 405 751.786 ± 0.028 Hz
$2S_{\frac{1}{2}}$	177.551 MHz

Theoretical contributions to the $1S_{\frac{1}{2}}$ $-2S_{\frac{1}{2}}$ frequency. The weighted mean of the Rydberg constants from Table 2.1 is used in these calculations. The value for the $1S_{\frac{1}{2}}$ hyperfine spliting is the experimental value, while the 2S value is deduced by noting that the splittings scale as n^{-3}.

2.2 QED contribution.

The preceding results for the energy levels of a hydrogen-like atom result from a treatment in which electromagnetic fields are considered classically. A further correction to $E_D(n,j)$ arises when the electromagnetic field is quantised. This quantity is called the Lamb shift and is defined as the correction that has to be added to

$$E_D(n,j) + E_R(n,\ell,j)$$

to give the correct energy. This definition differs from Erickson's where the recoil correction $E_R(n,\ell,j)$ was included as part of the Lamb shift [1].

A simple physical picture for the origin of QED corrections is given by Welton [4]. Quantisation of the radiation field results in fluctuating field strengths even in empty space. Such fluctuations are responsible for spontaneous emission of atoms in excited states. The effects of fluctuations on an electron in a bound state in an atom results in the dominant QED correction to the energy levels.

Consider an electron in free space. It is acted upon by the zero point field of the quantised electromagnetic field. For a fluctuation of frequency $\omega = kc$, the energy is

$\frac{1}{2}\hbar k c$. The total energy density can be written either as a volume integral over the electromagnetic energy density or as a sum over normal modes:

$$\frac{1}{2}\left\{\varepsilon_0\langle E^2\rangle_{av}+\mu_0\langle H^2\rangle_{av}\right\}V=\int_0^\infty\left(\frac{1}{2}\hbar k c\right)\cdot 2\cdot\frac{4\pi k^2\,dk}{\frac{8\pi^3}{V}} \qquad (2.2,1)$$

since $\varepsilon_0\langle E^2\rangle_{av}=\mu_0\langle H^2\rangle_{av}$

$$\langle E^2\rangle_{av}=\frac{2\hbar c}{(4\pi\varepsilon_0)\pi}\int_0^\infty k^3\,dk \qquad (2.2,2)$$

This enables the average value of a frequency component of the field to be defined as

$$\langle E^2\rangle_\omega=\frac{2\hbar\omega^3}{(4\pi\varepsilon_0)\pi c^2} \qquad (2.2,3)$$

If the electron is assumed to move with nonrelativistic velocities, then the influence of the fluctuations of frequency ω on the electron position vector $\underline{q}$ obey:

$$m_e\frac{d^2q}{dt^2}=eE \qquad (2.2,4)$$

For a given harmonic $\underline{E_\omega}$ the solution is

$$\underline{q}_\omega=\frac{eE_\omega}{m_e\,\omega^2} \qquad (2.2,5)$$

or

$$\langle q_\omega^2\rangle=\left(\frac{e^2}{m_e^2\,\omega^4}\right)\frac{2\hbar\omega^3}{(4\pi\varepsilon_0)\pi c^2}=\frac{2\alpha\hbar^2}{\pi m_e^2}\,\frac{1}{k} \qquad (2.2,6)$$

The mean square fluctuation is given by

$$\langle(\Delta q)^2\rangle_{av} = \frac{2\alpha\hbar^2}{m_e^2\pi}\int_{K_0}^{K}\frac{dk}{k} \tag{2.2,7}$$

Upper and lower limits are introduced to prevent the integral diverging. The justification being that at sufficiently high frequencies there is a longitudinal as well as transverse recoil of the electron. This occurs when K= Compton wavelength of the electron, $K = \frac{m_e c}{\hbar}$ and at this point (2.2,4) is not valid. At low frequencies the fluctuation energy is infinite for a free electron but not a bound electron. A bound electron is constrained to positions close to the atom and cannot undergo the large slow fluctuations predicted by (2.2,5). K_0 will be related to the bound state in the atom. The effective potential seen by the electron undergoing fluctuation is

$$V(\underline{q}+\Delta\underline{q}) = \left[1+\Delta\underline{q}\cdot\nabla+\frac{1}{2}(\Delta\underline{q}\cdot\nabla)^2+\ldots\right]V(\underline{q})$$

since $\langle\Delta\underline{q}\rangle=0$, averaging over all $\Delta\underline{q}$ gives

$$\langle V(\underline{q}+\Delta\underline{q})\rangle = \left[1+\frac{1}{6}(\Delta q)^2\nabla^2+\ldots\right]V(\underline{q})$$

For a coulomb potential the change in $V(\underline{q})$ due to fluctuations is

$$\Delta V(\underline{q}) = -\left(\frac{ze^2}{4\pi\mathcal{E}_0}\right)\frac{1}{6}\cdot\frac{2\alpha\hbar^2}{m_e^2\pi}\ln\left(\frac{m_e c^2}{\hbar K_0 c}\right)\left[-4\pi\delta(\underline{q})\right]$$

Using perturbations theory to obtain the first order change in the energy levels the result is

$$E_L(n,\ell) = \frac{4\alpha\,(\alpha Z)^4 m_e c^2}{3\pi n^3}\,\ln\left(\frac{m_e c^2}{\hbar K_0 c}\right)\delta_{\ell 0} \qquad (2.2,8)$$

The $\delta_{\ell 0}$ arises from the $\delta(\underline{q})$ in the previous equation and means that the energy correction $E_L(n,\ell)$ is only appreciable for those states with wavefunctions which are non zero at the origin. The effect of the fluctuation is to weaken the coulombic potential and causes an upward shift in energy levels. Consequently (2.2,8) predicts that the $2S_{1/2}$ lies above the $2P_{1/2}$ as found by Lamb and Retherford [5]. Welton's result (2.2,8) also correctly predicts that the QED corrections scale as n^{-3}. This means that the ground state Lamb shift is approximately 8 times larger than the $2S_{1/2}$ Lamb shift. A value for the Lamb shift may be deduced from (2.2,8) by using a value for the Lower cut off, K_0, calculated by Bethe [9], $\hbar c K_0 = 3.88\times10^{-17}$ J

$$E_L(n,\ell) = \frac{(8\times10^9\ \mathrm{Hz})\,h\,Z^4}{n^3} \qquad (2.2,9)$$

This value is close to the more precise calculations outlined in Appendix A.

Returning to Erickson's results, the dominant radiative correction due to the Dirac energy level structure is the vacuum fluctuation contribution:

{IR LOG}

$$\frac{4\alpha(\alpha Z)^4 m_e c^2}{3\pi n^3}\left(\frac{\mu}{m_e}\right)^3\left[\left\{\ln\left(\frac{1}{\alpha Z}\right)^2 + \ln\left(\frac{m_e}{\mu}\right) + \frac{11}{24}\right\}\delta_{\ell 0} + L_n\right] \qquad (2.2,10)$$

This term, together with the anomalous magnetic moment of the electron $(+\frac{3}{8})$ and vacuum polarisation effects $(-\frac{1}{5})$ which change the $\frac{11}{24}$ term in (2.2,10) to $\frac{11}{24}+\frac{3}{8}-\frac{1}{5}$, contribute over 90% of S state Lamb shifts. The contribution L_n is the αZ and $\frac{m_e}{M}$ independent part of the Bethe Logarithm and is given in Table B of [1].

The next largest contribution arises from higher order self energy and magnetic moment terms left uncalculated in (2.2,10). Representing these terms by

{ (H TOT) } $$\frac{4\alpha(\alpha Z)^4 m_e c^2}{3\pi n^3} H(\alpha Z)$$

$H(\alpha Z)$ is given by

$$H(\alpha Z) = C_5 Z\alpha + (Z\alpha)^2\left[C_{62}\ln^2(Z\alpha)^2 + C_{61}\ln\left(\frac{1}{Z\alpha}\right)^2 + C_{60} + C_7 Z\alpha\right]$$

In this expression the coefficients C are given in Table C, [1]. C_5, C_{61} and C_{62} are terms calculated exactly for small αZ. The form of $H(\alpha Z)$ given above retains the known behaviour at small αZ while introducing C_{60} and C_7 in order to provide an approximation valid for large αZ. These coefficients are discussed fully in [1,6,7]. The coefficient C_{60} is the origin of the discrepency between the theoretical works of Erickson [1] and Mohr [6]. The difference between the two predictions for the 1S-2S frequency is approximately 300 kHz (1 part in 10^{10}), see Appendix A, Table A.3. Notice that to choose between the two theoretical values in hydrogen by measuring the $1S_{1/2}$-$2S_{1/2}$ frequency would require an accuracy better than 1 part in 10^{10} and that the uncertainty in the Rydberg constant be less than this level. The discrepancy increases in high atoms and experiments are underway to test these predictions in many places [8] and references therein.

A number of other terms which are all relatively small contribute to the Lamb shift. A list of the contributions for the $1S_{1/2}$ and $2S_{1/2}$ Lamb shift are given in Table 2.2 for H.

2.3. Structure of the $1S_{\frac{1}{2}}$-$2S_{\frac{1}{2}}$ transition.

It has been assumed so far in this chapter that the energy levels in a hydrogen like atom are completely specified by the quantum numbers n, ℓ and j through the following expression:

$$E_D(n,j) + E_R(n,\ell,j) + E_L(n,\ell) \qquad (2.3,1)$$

where $E_L(n,\ell)$ is the Lamb shift as defined in Section 2.2. This is not strictly true since the influence of the magnetic moment of the nucleus on the energy level structure has been ignored. The nuclear magnetic dipole moment $\underline{\mu}_I$ is related to the nuclear spin angular momentum $\hbar\underline{I}$ by

$$\underline{\mu}_I = g_I \frac{m_e}{M} \mu_B \underline{I}$$

Here g_I is the nuclear g factor and μ_B is the Bohr magneton, $\mu_B = \frac{e\hbar}{2m_e}$. The energy of interaction arises through a magnetic field experienced by the nucleus and caused by the orbiting electrons. There are three contributions to this field.

(1). The orbiting electrons constitute a current which induces a magnetic field at the origin. For spherically symmetric charge distributions (ie. closed shells or S state valence electrons) this contribution vanishes.

(11). The spin magnetic moment of the electrons can interact directly with the magnetic moment of the nucleus. This is analogous to the interaction between two classical magnetic dipole moments. This contribution again vanishes for S states.

(111). For S states the interaction is given by the Fermi contact potential. The non-zero probability of finding the electron at the nucleus gives rise to a magnetisation $\underline{M} = \underline{\mu}_S |\Psi(0)|^2$. From classical magnetostatics [10], the field inside a magnetised sphere $\underline{H} = -\frac{\underline{M}}{3}$. Thus the magnetic field

$$\underline{B} = \mu_0 (\underline{H} + \underline{M}) = \frac{2}{3} \mu_0 \underline{M}$$

and

$$H_{hf} = -\underline{\mu}_I \cdot \underline{B} = -\frac{2}{3}\mu_0 \, \underline{\mu}_I \cdot \underline{\mu}_s \, |\psi(0)|^2 \tag{2.3,2}$$

Notice that this contribution vanishes for non S states.

For the case of hydrogen-like atoms the interaction Hamiltonian can be summarised by

$$H_{hf} = A(J) \, \underline{I} \cdot \underline{J}$$

since the magnetic field experienced by the nucleus is in all cases proportional to $\underline{J}$ [11,12,13]. The energy level shift can be represented by

$$E_{hf}(n, F, J, I) = \frac{A(J)}{2}\left[F(F+1) - I(I+1) - J(J+1)\right] \tag{2.3,3}$$

where $F = I + J$ and F takes values from $|J - I|$ to $J + I$. Using the useful property, which is valid for all hydrogen-like atoms, that $A(J)$ is the same for all states independent of ℓ

$$A(J) = \frac{8}{3}\left(\frac{\mu_0}{4\pi}\right) g_I \, g_s \, \frac{Z^3}{n^3 a_0^3}\left(\frac{m_e}{M}\right)\mu_B^2 \tag{2.3,4}$$

is obtained from (2.3,2) together with $|\psi(0)|^2 = \frac{Z^3}{\pi n^3 a_0^3}$. Thus

$$E_{hf}(n, F, J, I) = \left(\frac{m_e}{M}\right) g_I \left(\frac{g_s}{2}\right) h\, c\, R_\infty \left(\frac{\alpha^2 Z^3}{n^3}\right)\left\{\frac{F(F+1) - I(I+1) - J(J+1)}{J(J+1)(2\ell+1)}\right\} \tag{2.3,5}$$

Two corrections have to be applied to $E_{hf}(n,F,J,I)$. The reduced mass correction arises from the a_0^{-3} term since the effect of the reduced mass is to increase a_0 to $\frac{m_e}{\mu}a_0$. So

$$E_{hf}(n,F,J,I) = \left(\frac{\mu}{m_e}\right)^3\left(\frac{m_e}{M}\right) g_I \frac{g_s}{2} \frac{h c R_\infty}{n^3} \alpha^2 Z^3 \left\{\frac{F(F+1) - I(I+1) - J(J+1)}{J(J+1)(2L+1)}\right\}$$

(2.3,6)

If the electron was a pure Dirac particle of spin $1/2$ the electron g factor g_s would precisely equal 2. It is found that

$$\frac{g_s}{2} = \left\{1 + \frac{\alpha}{2\pi} - 0.328\frac{\alpha^2}{\pi^2} + \dots\right\}$$

(2.3,7)

It is of historical interest to note that it was the discrepancy between theory and experiment on measurements of the ground state hyperfine structure of hydrogen that lead to the discovery of the anomalous magnetic moment of the electron. Table 2.2 (b) gives values of the hyperfine splitting for the $1S_{1/2}$ and $2S_{1/2}$ levels of H . Figure 2.1 outlines the level structure as so far described.

The reason why it is convenient to neglect the hyperfine splitting arises directly from the selection rules of a two photon transition. For an S→S transition the rules are $\Delta F=0$ and $\Delta M=0$, and the intensities are proportional to the statistical weights of the transition. It can be shown that the centroid of the $1S_{1/2}-2S_{1/2}$ transition defined by

$$\nu_{1S-2S} = \frac{3\nu_{F=1\rightarrow F=1} + \nu_{F=0\rightarrow F=0}}{4}$$

is simply the frequency predicted by the Dirac theory including the Lamb shift and unperturbed by the hyperfine interaction. This result is only of importance when the hyperfine components are not clearly resolved. In the present experiment the hydrogen hyperfine structure was well resolved.

2.4. Summary.

The experiment described in this thesis aims to make a measurement of the 1S-2S two photon transition frequency. To be more precise, one quarter of the 1S-2S frequency is compared with a calibrated line in $^{130}Te_2$ vapour (see Chapter 4). From this measurement a number of deductions may be made.

Firstly the predicted value of the 1S-2S frequency is given by

$$\frac{1}{h}\left\{E_D(2,\tfrac{1}{2}) - E_D(1,\tfrac{1}{2}) + E_R(2,0,\tfrac{1}{2}) - E_R(1,0,\tfrac{1}{2}) + E_L(2,0) - E_L(1,0)\right\} \qquad (2.4,1)$$

where the hyperfine splitting has been neglected. This number may be compared directly with the experimental value. This is the most obvious method of analysing the data.

Alternatively, it may be accepted that the Dirac contributions are exact at least to within the experimental uncertainty of the Rydberg constant. That being the case, the Dirac contribution (Table 2.2) may be subtracted from eq.(2.4,1) leaving the Lamb shift. The Dirac contribution is also subtracted from the experimentally determined 1S-2S frequency. This enables a test of the QED predictions to be made. Notice that in carrying out this process the experimental uncertainty of the measurement is increased slightly because the uncertainty in the theoretical value of the Dirac levels due to the Rydberg constant has to be combined with it.

Finally, if the experimental value of the 1S-2S frequency is sufficiently accurate, a new value of the Rydberg constant could be deduced from this measurement. That will not be done in this experiment, but the required increase in accuracy is possible. It is remarkable that the precision from a pulsed experiment can approach the results obtained from essentially c.w. experiments.

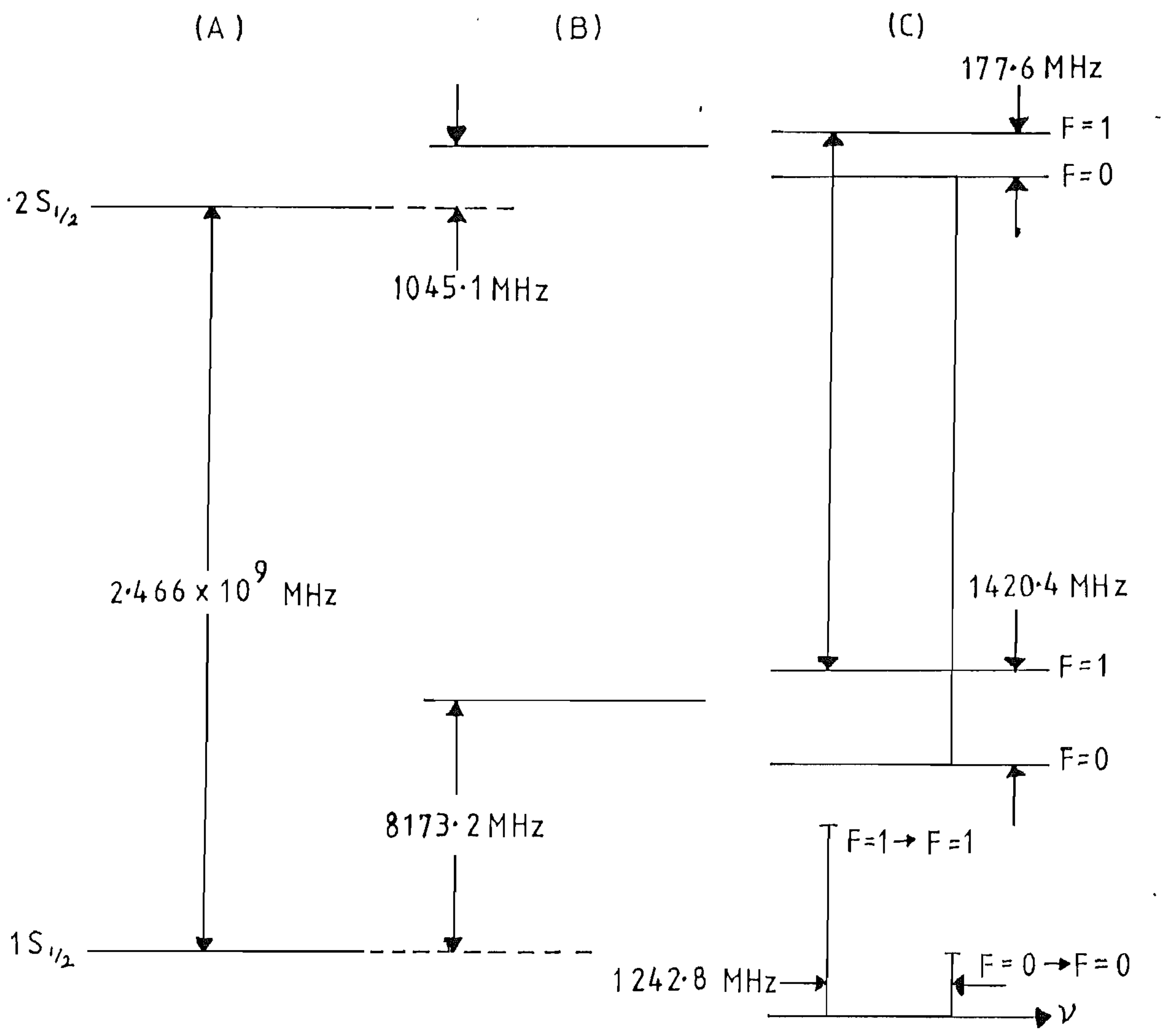

Figure 2.1. The n=1 and n=2 levels of atomic hydrogen.

(A). The Dirac energy levels with l=0. For clarity the 2 $P_{1/2}$ and the 2 $P_{3/2}$ levels have been omitted.

(B). The 2 $S_{1/2}$ and 1 $S_{1/2}$ levels shifted by the Lamb shift.

(C). The energy levels including the hyperfine structure and showing therelative intensities of the allowed two photon transitions obeying $\Delta F=0$.

References.

[1] G. Erickson. J. Phys. Chem. Ref. Data. 6 831. (1977).

[2] P.A.M. Dirac. "Principles of Quantum Mechanics". 3rd. ed. Clarendon Press. (1947).

[3] H. Bethe, E. Saltpeter. "Quantum Mechanics of One- and Two- Electron Atoms". p83. Plenum. (1977).

[4] T.A. Welton. Phys. Rev. 74 1157. (1948).

[5] W. Lamb, R. Retherford. Phys. Rev. 79 549. (1950).

[6] P. Mohr. Phys. Rev. Lett. 34 1050. (1975).

[7] J. Saperstein. Phys. Rev. Lett. 47 1723. (1981).

[8] P. Pellegrin, Y.El. Masri, L. Palfry. Phys. Rev. A. 31 5. (1985).

[9] H.A. Bethe. Phys. Rev. 72 339. (1947).

[10] P. Lorrain, D. Corson. "Electromagnetic Fields and Waves". p391. Freeman. 2nd. Ed. (1970).

[11] H. Bethe, E. Saltpeter. "Quantum Mechanics of One- and Two- Electron Atoms". p107. Plenum. (1977).

[12] A. Corney. "Atomic and Laser Spectroscopy". p708. Clarendon Press. (1979).

[13] G.K. Woodgate. "Elementary Atomic Structure". p168. Clarendon Press. (1980).

[14] J.E.M. Goldsmith, E.W. Weber, T.W. Hänsch. Phys. Rev. Lett. 41 1525. (1978).

[15] B.W. Petley, K. Morris, R.E. Schawyer. J. Phys. B. 13 3099. (1980).

[16] S.R. Amin, C.D. Caldwell, W.Lichten. Phys. Rev. Lett.

18 1234. (1981).

[17] B.N. Taylor. Private communication of works carried out in connection with the 1985 least squares adjustment of fundamental constants.

Chapter 3. The hydrogen atom in external fields.

This chapter examines in detail the effects which perturb the energy levels of a real hydrogen atom from the fictitious isolated atom described in Chapter 2. The initial discussion covers the Doppler free two photon excitation and derives results which enable transition rates to be estimated. Ionisation rates from the $2S_{1/2}$ level are also discussed. The shifts of energy levels due to the A.C. and D.C. Stark effects are covered in Sections 3.5 and 3.6 respectively. Section 3.7 covers perturbations such as pressure which are less well known for two photon Doppler free spectroscopy of the hydrogen atom. Experimentally these shifts are found to be small, but if the ultimate resolution possible on the $1S_{1/2}$-$2S_{1/2}$ transition is to be achieved, these perturbations will have to be known accurately both theoretically and experimentally.

3.1. Time varying electromagnetic fields.

Under certain circumstances an atom can absorb energy from an electromagnetic field and undergo a transition. For single photon transitions one requirement is that the frequency of the field corresponds to the energy difference between the initial and final levels. Two photon transitions are also possible and these will be examined in detail. This will be done by deriving equations which describe two photon transition probabilities. This problem is well covered in the literature [1,2,3], but a better physical insight can be obtained by examining the problem of interest rather than by quoting general results.

The starting point for this discussion will be the nonrelativistic Hamiltonian for the interaction of an electromagnetic field with an isolated atom. The approach is semi-classical since no information useful for calculating transition rates would be obtained by quantising the radiation field in this case. The non relativistic Hamiltonian is

$$H(\underline{r},t) = \frac{1}{2m_e}\left(\underline{p} + e\underline{A}\right)^2 - e\phi + V(\underline{r}) \tag{3.1,1}$$

where $\underline{A}$ is the vector potential of the electromagnetic field, and ϕ is the scalar potential of the same field. The Hamiltonian

$$H_o(\underline{r},t) = \frac{\underline{p}^2}{2m_e} + V(\underline{r}) \tag{3.1,2}$$

represents the unperturbed atom in the absence of an electromagnetic field. The potential $V(\underline{r})$ is assumed to commute with $\dot{\underline{r}}$. If $V(\underline{r})$ is a coulombic potential then this is the case. Consequently

$$\underline{r} H_0 - H_0 \underline{r} = i \frac{\hbar}{m_e} \underline{p} \tag{3.1,3}$$

The remainder of $H(\underline{r},t)$ will be used as a perturbation.

$$H_1(\underline{r},t) = \frac{e}{2m_e}\left(\underline{p}\cdot\underline{A} + \underline{A}\cdot\underline{p}\right) + \frac{e^2}{2m_e}\underline{A}\cdot\underline{A} - e\phi \tag{3.1,4}$$

$H_1(\underline{r},t)$ may be simplified by making some assumptions which apply to an atom irradiated by a nearly monochromatic unidirectional mode of the electromagnetic field. The term in $\underline{A}\cdot\underline{A}$ will be neglected in this problem. The ratio of the $\underline{A}\cdot\underline{A}$ term to the $\underline{A}\cdot\underline{P}$ term is approximately

$$e\frac{\underline{A}\cdot\underline{A}}{\underline{p}\cdot\underline{A}} \approx \frac{e a_0 E}{\left(\frac{e^2}{4\pi\varepsilon_0 a_0}\right)} \tag{3.1,5}$$

where a_0 is the radius of the first Bohr orbit in hydrogen. Typical values may be estimated for the pulsed laser used in this experiment by assuming a pulse energy of 50 μJ in 5 ns passing through a spot size of 100 μm. The intensity is $3\times10^{11}\,\mathrm{Wm}^{-2}$ corresponding to an electric field $E \sim 1.5\times10^{6}\,\mathrm{Vm}^{-1}$. Evaluating eq.(3.1,5), which is the ratio of the dipole interaction energy to the potential energy of an electron in the first Bohr orbit, shows that the $e\underline{A}\cdot\underline{A}$ interaction is approximately 10^{-6} of the $\underline{A}\cdot\underline{P}$ interaction.

Consequently it will be ignored in what follows.

Making the usual assumptions for a plane wave travelling through a linear isotopic medium with no free charges or currents gives the following Maxwell's equation:

$$\nabla \times \underline{E} = -\frac{\partial \underline{B}}{\partial t} \qquad (3.1,6a)$$

$$\nabla \times \underline{B} = \frac{\mu_r \varepsilon_r}{c^2} \frac{\partial \underline{E}}{\partial t} \qquad (3.1,6b)$$

$$\nabla \cdot \underline{E} = 0 \qquad (3.1,6c)$$

$$\nabla \cdot \underline{B} = 0 \qquad (3.1,6d)$$

where the symbols take their usual meaning. A plane wave travelling in the z direction will have no variation in the x and y direction. Eq.(3.1,6c) gives $\frac{\partial E_z}{\partial z} = 0$ and since we are not interested in steady longitudinal fields, E_z may be taken as zero, and the wave is transverse [4]. Given that Maxwell's equations may be satisfied for a transverse plane wave if $\phi = 0$ the vector potential enables both the $\underline{E}$ field and the $\underline{B}$ field to be calculated

$$\underline{E} = -\nabla\phi - \frac{\partial \underline{A}}{\partial t} = -\frac{\partial \underline{A}}{\partial t} \qquad (3.1,7a)$$

$$\underline{B} = \nabla \times \underline{A} \qquad (3.1,7b)$$

If $\underline{A}$ is a harmonic field, the time differential in (3.1,7a) may be replaced by $i\omega$ and using (3.1,6c) $\underline{A}$ obeys

$$\nabla \cdot \underline{A} = 0 \tag{3.1,8}$$

This result means that $\underline{A}$ and $\underline{p}$ commute so the perturbing Hamiltonian reduces to

$$H_1(\underline{r},t) = \frac{e}{m_e}\,\underline{A}\cdot\underline{p} \tag{3.1,9}$$

Taking the vector potential to be

$$\underline{A} = 2\,\underline{A}_0 \cos(\omega t - \underline{k}\cdot\underline{r})$$

the following fields are obtained from (3.1,7)

$$\underline{E} = 2\omega\,\underline{A}_0 \sin(\omega t - \underline{k}\cdot\underline{r}) \tag{3.1,10a}$$

$$\underline{B} = 2(\underline{k}\times\underline{A}_0)\sin(\omega t - \underline{k}\cdot\underline{r}) \tag{3.1,10b}$$

The latter is deduced using the vector identity

$$\nabla\times(f\underline{A}) = (\nabla f)\times\underline{A} + f(\nabla\times\underline{A})$$

with $f = \cos(\omega t - \underline{k}\cdot\underline{r})$ and $\nabla\times\underline{A} = \underline{B}$. The intensity of a plane wave is defined by [4]

$$\underline{I} = \underline{E}\times\underline{H} = \frac{\underline{E}\times\underline{B}}{\mu_r\mu_0} \tag{3.1,11}$$

In the laboratory it is the time average of $\underline{I}$ that is measured. Since $\underline{E}$, $\underline{B}$ and $\underline{k}$ are mutually perpendicular:

$$I = \langle|\underline{I}|\rangle = \frac{n\,|E_0|^2}{\mu_r\mu_0 c}\langle\sin^2(\omega t - \underline{k}\cdot\underline{r})\rangle = \frac{1}{2}\,n\varepsilon_0 c\,|E_0|^2 \tag{3.1,12}$$

where $\mu_r = 1$ and $|E_0|$ is the amplitude of the real electric field. In terms of the complex amplitude of the vector potential

$$I = \langle |\underline{I}| \rangle = 2n\varepsilon_0 c\omega^2 |A_0|^2 = 4n\varepsilon_0 c\omega^2 \langle |\underline{A}|^2 \rangle$$

(3.1,13)

The units of I are watts m^{-2}.

3.2. Time dependent perturbation theory

The time dependent Schrodinger equation describing the interaction between an atom and electromagnetic field is

$$i\hbar \frac{\partial \Psi}{\partial t} = (H_0 + H_1) \Psi$$

(3.2,1)

H_0 and H_1 are given by (3.1,2) and (3.1,9) respectively. The relative sizes of H_0 and H_1 may be deduced by a similar argument as that leading to (3.1,5). The result is

$$\frac{H_1}{H_0} \approx \frac{e a_0 E}{\frac{1}{2} V(a_0)} \sim 10^{-6}$$

(3.2,2)

Since this represents a small interaction it is possible to attempt an approximate solution of (3.2,1) using time dependent perturbation theory [5,6].

The method is to assume that a complete set of orthonormal solutions are available to the equation

$$i\hbar \frac{\partial \Phi_m}{\partial t} = H_0 \Phi_m \tag{3.2,3}$$

Since the set Φ_m is complete the solution to (3.2,1), Ψ, may be expressed as

$$\Psi = \sum_m C_m(t)\, \phi_m\, e^{-i\omega_m t} = \sum_m C_m(t)\, \Phi_m \tag{3.2,4}$$

The time dependence of the solution Ψ is represented in terms of the Φ_m by $C_m(t)$ where $|C_m(t)|^2$ is the probability that the atom is in the state Φ_m after a time t. The time dependence $\frac{dC_k(t)}{dt}$ is found from (3.2,1) and (3.2,4) to be

$$\frac{dC_k(t)}{dt} = \frac{1}{i\hbar} \sum_m C_m(t)\, (\phi_k, H_1 \phi_m)\, e^{i\omega_{km} t} \tag{3.2,5}$$

where $\hbar\omega_{km} = (E_k - E_m)$. The set of equations (3.2,5) are to be solved subject to the condition that at some time in the past, $t = -\infty$ say, the system was in a definite state, m=g. In order to apply the theory so far developed to a real atom, a modification must be made to (3.2,5). The electromagnetic field is being treated semi-classically so that spontaneous decay which is caused by the zero point fluctuations of the quantised electromagnetic field is not included naturally. Instead decay rates are included in (3.2,5) in an ad hoc manner.

$$\frac{d}{dt} C_K(t) + \left(\frac{\gamma_K}{2}\right) C_K(t) = \frac{1}{i\hbar} \sum_m C_m(t) \; (\phi_K, H_1 \phi_m) \, e^{i\omega_{Km} t}$$

(3.2,6)

where $\gamma_K = \frac{1}{\tau_K}$ and τ_K is the $\frac{1}{e}$ lifetime of the level K. This procedure ensures that an excited state decays with the experimentally correct lifetime τ_K. So far no approximations have been made.

The set of equations (3.2,6) cannot be solved exactly analytically since to evaluate $C_K(t)$ say, all the other $C_m(t)$, $K \neq m$, must be known. Clearly if this were the case it would no longer be necessary to solve (3.2,6) since the value of $|C_K(t)|^2$ could be obtained from the normalisation condition

$$\sum_m | C_m(t) |^2 = 1$$

which can be obtained from (3.2,4). The solution is found approximately by letting

$$C_m(t) = C_m^{(0)}(t) + C_m^{(1)}(t) + C_m^{(2)}(t) + \ldots$$

(3.2,7)

Substituting (3.2,7) into (3.2,6) the standard time dependent perturbation theory expansion

$$\frac{d}{dt} C_K^{(\ell+1)}(t) + \left(\frac{\gamma_K}{2}\right) C_K^{(\ell+1)}(t) = \frac{1}{i\hbar} \sum_m C_m^{(\ell)}(t) \; (\phi_K, H_1 \phi_m) \, e^{i\omega_{Km} t}$$

is found where ℓ represents the order of approximation.

3.3. Two photon transition rates.

The perturbation written out in full is

$$H_1(\underline{r},t) = \frac{e}{m_e} \underline{A}_o \cdot \underline{p} \left\{ e^{i(\omega t - \underline{k}\cdot\underline{r})} + e^{-i(\omega t - \underline{k}\cdot\underline{r})} \right\} \tag{3.3,1}$$

The spatial dependence of the perturbation due to the coordinate of the electron $\underline{r}$ enters through $e^{i\underline{k}\cdot\underline{r}}$, and since

$$\underline{k}\cdot\underline{r} \approx \frac{3}{8}(2\pi R_\infty).a_o = \frac{3}{8}\frac{2\pi R_\infty \alpha}{4\pi R_\infty} = \frac{3}{16}\alpha << 1$$

for hydrogen $e^{i\underline{k}\cdot\underline{r}} \sim 1$ is a good approximation. This is called the electric dipole approximation.

The model that will be analysed is the same as [7] so many manipulative steps in the argument will be omitted.

The atom is assumed to be in its ground state before the perturbation is applied.:

$$c_m(-\infty) = \delta_{og}$$

To prevent mathematical complexities from obscuring the physics, the slightly idealised problem of a laser pulse which is rectangular in time will be considered.

$$\underline{A}_o = \begin{cases} \underline{A}_o & 0 \leq t \leq \tau \\ 0 & t > \tau;\ t < 0. \end{cases}$$

where τ is the pulse length. Additionally the $e^{+i\omega t}$ term will be neglected from the perturbation (3.3,1) since this will be found to correspond to stimulated downward transitions. Since two photon transitions are generally weak this term can be neglected.

The solution for the first order equation

$$\frac{d}{dt}C_K^{(1)}(t) + \frac{\gamma_K}{2} C_K^{(1)}(t) = \frac{1}{i\hbar} H_{Kg}\, e^{i(\omega_{Kg}-\omega)t}$$

(3.3,2)

where $H_{Kg} = \left(\phi_K , \frac{e}{m_e} A_0 \cdot p \; \phi_g\right)$ is

$$C_K^{(1)}(t) = \frac{H_{Kg}}{\hbar}\left(\frac{e^{-\frac{\gamma_K t}{2}} - e^{i(\omega_{Kg}-\omega)t}}{(\omega_{Kg}-\omega) - i\left(\frac{\gamma_K}{2}\right)}\right) \qquad 0 \leq t \leq \tau$$

(3.3,3)

For $t > \tau$ there is no perturbation and $C_K(t)$ decays with the phenomological decay rate $\frac{\gamma_K}{2}$. The amplitude as a function of time is

$$|C_K(t)|^2 = \frac{|H_{Kg}|^2}{\hbar^2}\left\{\frac{e^{-\gamma_K t} + 1 - 2e^{-\frac{\gamma_K t}{2}}\cos(\omega_{Kg}-\omega)t}{(\omega_{Kg}-\omega)^2 + \left(\frac{\gamma_K}{2}\right)^2}\right\} = \frac{|H_{Kg}|^2}{\hbar^2} G . g(\omega,t)$$

(3.3,4)

The term in braces $\{\}$ may be written in terms of a normalised line shape $g(\omega,t)$ and a multiplying factor G.

$$g(\omega,t) = \frac{1}{G}\left\{\frac{e^{-\gamma_K t} + 1 - 2e^{-\frac{\gamma_K t}{2}}\cos(\omega_{Kg}-\omega)t}{(\omega_{Kg}-\omega)^2 + \left(\frac{\gamma_K}{2}\right)^2}\right\}$$

(3.3,5a)

$$G = \frac{\gamma_K}{2\pi(1 - e^{-\gamma_K t})}$$

(3.3,5b)

Notice that G is related to the characteristic time of the interaction. If the time of interaction is short $\gamma_K t << 1$ then $G \rightarrow 1/2\pi t$. If the pulse length is long compared with the natural lifetime $\gamma_K t >> 1$ $G \rightarrow \frac{\gamma_K}{2\pi}$. Thus it is reasonable to define the first order transition rate W_{Kg} to be

$$W_{Kg} = \frac{|c_K(\tau)|^2}{1/2\pi G} = \frac{H_{Kg}}{\hbar^2} 2\pi G^2 g(\omega,\tau)$$

In the long and short pulse limits

$$W_{Kg} = \begin{cases} \frac{|H_{Kg}|^2}{\hbar^2}\left(\frac{\gamma_K}{2\pi}\right) \frac{1}{(\omega_{Kg}-\omega)^2 + \left(\frac{\gamma_K}{2}\right)^2} & \gamma_K \tau >> 1 \\ \frac{|H_{Kg}|^2}{\hbar^2} \frac{1}{\tau} \frac{4\sin^2(\omega_{Kg}-\omega)\frac{\tau}{2}}{(\omega_{Kg}-\omega)^2} & \gamma_K \tau << 1 \end{cases}$$

In the long pulse the line shape is Lorentzian and has the natural width $\Delta\omega_{1/2} = \gamma_K$, in the short pulse case the lineshape is given by the artificial choice of a laser pulse amplitude which is rectangular in time. The linewidth is given by the laser linewidth $\frac{\pi}{\tau}$.

For the experiment being considered here the first order transition rate is zero since $H_{Kg}=0$ for an S→S transition. In this case the second order coefficient must be calculated:

$$\frac{d c_f^{(2)}(t)}{dt} + \left(\frac{\gamma_f}{2}\right) c_f^{(2)}(t) = \frac{1}{i\hbar}\sum_m H_{fK}\, e^{i(\omega_{Kg}-\omega)t}\, c_K^{(1)}(t).$$

(3.3,6)

Substituting (3.3,3) into (3.3,6) gives

$$c_f^{(2)}(t) = \frac{1}{\hbar}\left\{\sum_K \frac{H_{fK}\,H_{Kg}}{\omega_{Kg}-\omega-i\frac{\gamma_K}{2}}\right\}\left[\frac{e^{-\frac{\gamma_f t}{2}} - e^{i(\omega_{fg}-2\omega)t}}{\omega_{fg}-2\omega-i\frac{\gamma_f}{2}}\right]$$

(3.3,7)

By analogy with the first order transition rate, $W_{fg}^{(2)}$ is given by

$$W_{fg}^{(2)} = \frac{1}{\hbar^2}\left|\sum_K \frac{H_{fK}\,H_{Kg}}{\omega_{Kg}-\omega-i\frac{\gamma_K}{2}}\right|^2 \left\{\frac{\sin^2(\omega_{fg}-2\omega)\frac{T}{2}}{\left[(\omega_{fg}-2\omega)\frac{T}{2}\right]^2}\right\}$$

(3.3,8)

for the short pulse case $\gamma_f\tau \ll 1$. To evaluate $W_{fg}^{(2)}$ a value for the summation over matrix elements must be found. Let $\hat{\underline{\varepsilon}}$ be a unit vector representing the polarisation direction of the electromagnetic field $\underline{A}_0 = A_0\hat{\underline{\varepsilon}}$. The on resonance transition rate $W_{fg}^{(2)}$ for a unidirectional travelling wave may be written

$$W^{(2)}_{fg} = \frac{1}{4}\frac{e^4}{m_e^4}\frac{I^2}{\omega^4 n^2 \varepsilon_0^2 c^2 h^2}\left|\sum_K \frac{(\phi_f, \hat{\varepsilon}\cdot\underline{p}\,\phi_K)(\phi_K, \hat{\varepsilon}\cdot\underline{p}\,\phi_g)}{E_{Kg} - \hbar\omega}\right|^2 \tau$$

(3.3,9)

Equation (3.1,13) has been used to give A_0 in terms of the laser intensity I. The decay rates of the intermediate states γ_K is omitted from the denominator since $W^{(2)}_{fg}$ is only applicable if all other transitions are far from resonance. Using the definition of the fine structure constant (3.3,9) may be expressed compactly as

$$W^{(2)}_{fg} = \frac{(2\pi)^2 \alpha^2 |M|^2 I^2}{n^2}\begin{cases} \tau & \gamma_f \tau \ll 1 \\ \dfrac{4}{\gamma_f} & \gamma_f \tau \gg 1 \end{cases}$$

M is given for the hydrogen 1S-2S transition by [8]

$$M = \frac{1}{m_e \omega^2}\sum_K \frac{(\phi_f, \hat{\varepsilon}\cdot\underline{p}\,\phi_K)(\phi_K, \hat{\varepsilon}\cdot\underline{p}\,\phi_g)}{E_{Kg} - \hbar\omega}$$

$$= 5{\cdot}03 \times 10^{-3}\ \mathrm{m}^2\ \mathrm{J}^{-1}$$

Numerically, the rate on resonance is

$$W_{fg} = 5{\cdot}32 \times 10^{-8} I^2 \begin{cases} \tau & \gamma_f \tau \ll 1 \\ \dfrac{4}{\gamma_f} & \gamma_f \tau \gg 1 \end{cases}$$

(3.3,10)

This is the transition rate per atom per second. To obtain the transition probability per pulse eq. (3.3,10) has to be multiplied by the pulse length τ.

So far the atom has been assumed to be at rest in the laboratory frame. In a real gas the atom will be in motion and the perturbation frequency ω will in general be Doppler shifted to

$$\omega' = \frac{\omega\left(1 \pm \frac{V_x}{c}\right)}{\sqrt{1 - \frac{V_x^2}{c^2}}} \sim \omega\left(1 \pm \frac{V_x}{c}\right)$$

where terms of order $\frac{V_x^2}{c^2}$ which are typically $\sim 10^{-10}$ of the optical frequency for atomic hydrogen at room temperature have been neglected. V_x is the component of the atomic velocity along the laser beam direction and follows a Gaussian distribution characteristic of the temperature of the gas. For a two photon transition it is straightforward to observe that an atom can absorb energy from two counter-propagating beams, if $2\omega = \omega_{fg}$, independently of the value of V_x . One of the beams is Doppler shifted up in frequency while the other is shifted down in frequency as observed in the atomic frame of reference and the sum is independent of V_x :

$$\omega_{fg} = \omega\left(1 - \frac{V_x}{c}\right) + \omega\left(1 + \frac{V_x}{c}\right) = 2\omega + O\left(\frac{V_x^2}{c^2}\right)$$

The terms of order $\frac{V_x^2}{c^2}$ which were originally neglected cause the second order Doppler shift which redshifts the observed transition frequency by an amount which has been shown to be much smaller than the resolution of this experiment which is 10^{-10} of the optical frequency. Absorbtion of light from a single beam gives rise to a Doppler broadened background and it must be shown that the Doppler free signal can be observed against it. A full treatment is given elsewhere [2,7] so only a qualitative argument will be given here. Let $\Delta\nu_D$ be the Doppler width of the transition as observed on the exciting laser frequency scale and let $\Delta\nu_L$ be the laser linewidth. The contribution to the Doppler broadened background at a particular laser frequency ν_L will be proportional to the number of atoms excited, ie. roughly proportional to $\frac{\Delta\nu_L}{\Delta\nu_D}$. This is still true on the line centre of the transition. The Doppler free excitation only occurs within $\Delta\nu_L$ of the line centre and all the atoms independent of their axial velocity class can contribute. The resulting transition rate is four times the same constant that is involved in the Doppler broadened case. The reason for this is that the Doppler broadened transition rates are proportional to $2I^2$ (see (3.3,9)) while the Doppler free transition involves a modified M reflecting the fact that the one photon can be absorbed from each beam in either order.

$$M = \frac{1}{m_e^2\omega^2}\left\{\sum_k \frac{(\phi_f, \hat{\underline{\varepsilon}}_1\cdot\underline{p}\,\phi_k)(\phi_k, \hat{\underline{\varepsilon}}_2\cdot\underline{p}\,\phi_g)}{E_{kg}-\hbar\omega} + \frac{(\phi_f, \hat{\underline{\varepsilon}}_2\cdot\underline{p}\,\phi_k)(\phi_k, \hat{\underline{\varepsilon}}_1\cdot\underline{p}\,\phi_g)}{E_{kg}-\hbar\omega}\right\}$$

If the intensity and polarisation in each beam is the same, then the Doppler free transition rate is proportional to $4I^2$. The ratio of Doppler free excitation to Doppler broadened excitation is approximately $2\frac{\Delta\nu_D}{\Delta\nu_L}$ at line centre. The full result is [2]

$$\frac{4Ku}{\sqrt{\pi}\,\Gamma} = \frac{2\,\Delta\nu_D}{\sqrt{\pi}\sqrt{\ln 2}\,\Delta\nu_L}$$

For values used in this experiment the ratio is ~ 350 using $\Delta\nu_D \sim 7$ GHz, (this is a quarter of the real value since all frequencies and separations were observed at 486 nm. This is explained in Chapter 6), $\Delta\nu_L = 40$ MHz. Typical values observed for this ratio were in the region 50-100:1. Any effect which reduced the overlap of the beams in the cell could contribute to a reduction in signal strength. Despite the lack of agreement the enhancement of the Doppler free signal means that it is readily observable.

If the counter propagating beams are not exactly parallel and there is an angle θ between them, then it is straightforward to show that the Doppler width of the transition is [1]

$$\Delta\nu_D = \frac{4\nu}{c}\sin\left(\frac{\theta}{2}\right)\overline{V}$$

where $\overline{V} = \left[\frac{2kT\ln 2}{m}\right]^{1/2} \sim 1854$ ms for hydrogen at 300 K.

So

$$\Delta\nu_D = (28\ \mathrm{GHz})\sin\left(\frac{\theta}{2}\right)$$

For co-propagating beams this predicts $\Delta\nu_D = 28$ GHz, which is the Doppler width observed without Doppler free spectroscopy. Typical angles θ used in this experiment were $\sim 2\times10^{-4}$ rads so $\Delta\nu_D \sim 2.8$ MHz. This quantity is small compared with the laser linewidth (~ 40 MHz) used in this experiment and provides a negligible contribution to the observed linewidth.

3.4. Three photon ionisation.

The detection scheme used in this experiment was two photon resonantly enhanced, three photon ionisation [9,10,11,12]. Two photons at 243 nm are required to excite a hydrogen atom from its ground state to the $2S_{1/2}$ level. Subsequent absorbtion of a third photon with a wavelength shorter than 364.5 nm results in the ionisation of the hydrogen atom. Observation of the resonance involves collection of the resultant protons and electrons by applying a small electric field between two parallel metal plates. For the intensity range used in this experiment the non-resonant three photon ionisation is vanishingly small [13] and is not detectable.

The ionisation process can either be viewed as a single step process in which a transition from the ground state to the continuum occurs, or as a two step process in which the $2S_{1/2}$ level is physically populated and a proportion is subsequently ionised. In the approximation of the low excitation rates and no collisional damping both these processes should give the same rates. However if the excitation rates are high, giving significant probability of ionisation, the single step calculation [13] based on third order perturbation theory can overestimate the observed transition rate since saturation of the transition rate can occur if the probability of excitation approaches unity in any excitation step.

3.4.1. Three photon ionisation transition rates.

From Figure 11 of Reference [13] the transition rate for three photon ionisation can be written as

$$W_{1S-\epsilon P} = 3.75 \times 10^{-54} \frac{F^3}{\gamma^3} \text{ per second per atom} \tag{3.4,1}$$

where F is the photon flux in photons $cm^{-2}\ S^{-1}$ and γ is the linewidth of the intermediate resonance in S^{-1}. From the discussion in Section 3.3, γ has to be replaced by the laser linewidth at 243 nm.

The cross-section for ionisation from the 2S level to the εP continuum can be calculated using the results of Table I, Reference [14] to be $9.2 \times 10^{-18}\ cm^2$ in agreement with [15]. In a flux of F photons $cm^{-2}\ S^{-1}$ the ionisation rate per atom from the 2S level is

$$W_{2S-\epsilon P} = \sigma F \tag{3.4,2}$$

combining with the transition number per pulse given by eq.(3.3,10) for short pulse excitation, the total ionisation number per pulse from the ground state of hydrogen is

$$W_{1s-\epsilon p}\,\tau = 3{\cdot}2\times 10^{-53}\,F^3\tau^3$$

where the ionisation rate is

$$W_{1s-\epsilon p} = 3{\cdot}2\times 10^{-53}\,F^3\tau^2$$

(3.4,3)

since $\gamma = \frac{1}{\tau}$, eqs.(3.4,1) and (3.4,3) differ by an order of magnitude in the ionisation rate. The origin of this discrepancy is not known.

For the typical laser parameters used in this experiment (energy 1 μJ, pulse length 6 ns, spot radius 100 μm) the photon flux is 6.5×10^{23} cm^{-2}s^{-1}, and the transition rates per pulse are

$$(3{\cdot}4,1) \quad W_{1s-\epsilon p}\,\tau = 2{\cdot}2\times 10^{-7}$$

$$(3{\cdot}4,3) \quad W_{1s-\epsilon p}\,\tau = 1{\cdot}9\times 10^{-6}$$

At a pressure of 0.2 torr (2.6 Nm^{-2}) and assuming the atomic hydrogen forms 1/10 of the gas, the number density is $N = 6.3\times 10^{13}$ cm^{-3} and an interaction volume of $5\times 3\times 10^{-4}$ cm^3, the resulting number of ions is either 2×10^4 or 1.8×10^5 ions per pulse. These numbers are in excess of the noise level of the detector described in Section 5.6.

3.5. A.C. Stark shifts.

A time varying electric field can cause shifts of the energy levels as well as inducing transitions [16]. The shift can be shown to have a time independent component as well as components at twice the driving frequency. For optical excitation the latter may be ignored.

Consider a level m exposed to a monochromatic perturbation

$$H_1(t) = \frac{H_1}{2}\left\{ e^{i\omega t} + e^{-i\omega t} \right\}$$

The correction to the unperturbed wavefunction $\phi_m e^{-i\omega_m t}$ is

$$\Delta \Phi_m = \Delta\phi_m e^{-i\omega_m t} = -\sum_{k\neq m} \frac{H_{km}}{2\hbar}\left\{ \frac{e^{i\omega t}}{\omega_{km}-\omega} + \frac{e^{-i\omega t}}{\omega_{km}+\omega}\right\}\phi_k e^{-i\omega_m t}$$

where (3.2,4) and (3.3,3) have been used. The term representing stimulated emission neglected in (3.3,4) has been reintroduced. From time independent perturbation theory the change in energy due to H_1 is [17]

$$\Delta E_m = (\phi_m , H_1\Delta\phi_m) = \sum_{k\neq m}\frac{H_{km}H_{mk}}{4\hbar}\left\{\frac{e^{i\omega t}}{\omega_{km}-\omega} + \frac{e^{-\omega t}}{\omega_{km}+\omega}\right\}\left(e^{i\omega t}+e^{-i\omega t}\right)$$

$$= \frac{1}{4}\sum_{k\neq m}\frac{|H_{km}|^2}{\hbar}\left\{\frac{1+e^{2i\omega t}}{\omega_{km}-\omega} + \frac{1+e^{-2i\omega t}}{\omega_{km}+\omega}\right\}$$

Ignoring the time dependent terms $e^{\pm 2i\omega t}$, the D.C level shift is

$$\Delta E_m = \frac{e^2 E_0^2}{4} \sum_{K \neq m} \frac{|(\phi_K, \hat{\underline{\epsilon}} \cdot \underline{r}\, \phi_m)|^2}{\hbar} \left\{ \frac{1}{\omega_{Km} - \omega} + \frac{1}{\omega_{Km} + \omega} \right\}$$

(3.5,1)

The form of the perturbation used is

$$H_1(t) = -e\, \underline{E} \cdot \underline{r} = -e E_0\, \hat{\underline{\epsilon}} \cdot \underline{r} \cos\omega t$$

which is valid in the dipole approximation [18]. In the limit $\omega \to o$ the $e^{i2\omega t}$ terms omitted from (3.5,1) must be retained. In this case (3.5,1) reduces to the familiar form for the quadratic D.C. Stark effect.

The effect of the A.C. Stark effect has been explored experimentally and good agreement found with theory [16]. In previous experiments on hydrogen [7,20] the A.C. Stark effect has been included as a calculated systematic correction. The resolution in these experiments was too poor to confirm the expected magnitude of the shifts. This is also the case in the experiment described here.

The value for the A.C. Stark shift for the 1S-2S transition is calculated in [7]. A recalculation has been undertaken for this experiment. The method used is similar to [7] so that the calculation will only be discussed in outline. Values for the matrix elements $(\phi_K, \hat{\underline{\epsilon}} \cdot \underline{r}\, \phi_m)$ were obtained for the discrete states from [21] and the continuum from [22]. The numerical summation and integration were found to give good agreement with the results of [7]. The result is

$$\Delta\nu_{1s-2s} = \frac{e^2 a_0^2}{6\varepsilon_0 c (R_\infty h c) h} \{46 \cdot 35\} I \qquad (3.5,2)$$

for a single laser beam of intensity I. Evaluating the constants gives

$$\Delta\nu_{1s-2s} = +1 \cdot 4 \text{ Hz } W^{-1} cm^2 \qquad (3.5,3)$$

The effect is a combination of a lowering of the 1S energy due to repulsion of all the higher lying states and a raising of the $2S_{1/2}$ level which is influenced mainly by the nearby $2P_{1/2}$ level. The shift of the $2S_{1/2}$ level is 5 times the shift of the 1S level. The overall shift increases the 1S-2S frequency. For the experimental arrangement considered here the Stark shift is twice the value given by (3.5,3) since counter-propagating beams are present. This result is approximately 15% larger than that of [7], the difference being due to the values of the fundamental constants used in (3.5,2).

For the intensities used in this experiment the A.C. Stark shift is smaller than the statistical uncertainty which means that it is difficult to observe. For a U.V. pulse of length 6 ns, energy 1 μJ, and spot size 100 μm the laser intensity I is 0.5 MWcm^{-2} which increases the measured 1S-2S frequency by 1.5 MHz. However, since up to 20 μJ has been generated for use in this experiment, once the resolution is improved the A.C. Stark shift might be observable.

3.6. D.C. Stark shifts.

The energy level shifts caused by external electric fields are important in precision measurements on atoms. The shifts manifest themselves in two ways. Firstly, the experimental environment may not necessarily be free from stray electric fields. The atom may have to be prepared in a discharge where the electric fields may be difficult to measure. Alternatively, as in this experiment, a small known electric field is applied in order to detect the electrons produced in three photon ionisation detection. Secondly, the presence of other atoms and molecules in the experimental cell can perturb the transition frequency. Such effects may manifest themselves as Stark shifts due to the electric fields of atoms, molecules or ions passing close to the atom of interest. These shifts are normally called pressure shifts since they are related to the number density of the perturbers and will be discussed in a later section.

Obviously it is important to choose a transition which is insensitive to Stark shifts if precision measurements

Table 3.1.

$M_J = 1/2$

	$2S_{1/2}$	$2P_{1/2}$	$2P_{3/2}$
$2S_{1/2}$	$L_1 - \varepsilon$	$\pm\sqrt{3}\,S$	$\sqrt{6}\,S$
$2P_{1/2}$	$\pm\sqrt{3}\,S$	$L_2 - \varepsilon$	0
$2P_{3/2}$	$\sqrt{6}\,S$	0	$L_3 - \varepsilon$

Table 3.1.

Matrix elements for the Stark shift calculation for the $2S_{1/2}$ level. $S = 1.2795\,E$ where E is the electric field in volts/cm, and the shift is in MHz. If $L_2 = 0$ then $L_1 = 1057.9$ MHz and $L_3 = 10969$ MHz.

Figure 3.1.

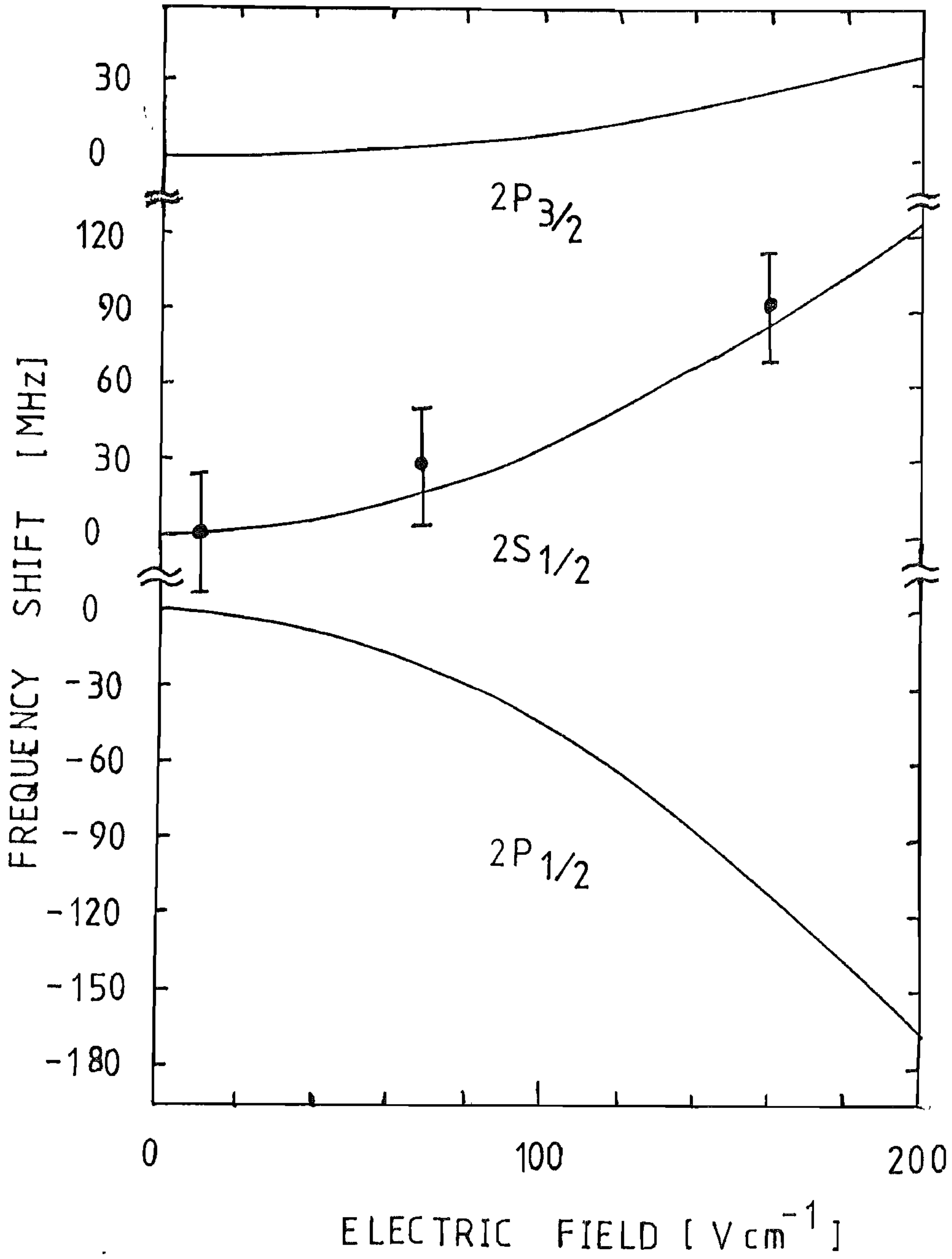

Figure 3.1.

D.C. Stark shifts of the n=2 levels in hydrogen. The experimental points are discussed in Section 3.6.1.

for metrological purposes are required. In this section it is hoped to demonstrate that the 1S-2S transition fulfils these requirements.

In the following discussion the hyperfine interaction will be neglected since a treatment by [23] indicates that for the fields used in this experiment the differences should not be noticeable. The energy level shifts which will be derived apply to the fine structure levels, which, as has already been discussed, are the centroids of the hyperfine levels. The range of field strengths of interest are those for which the Stark shift is small as compared with fine structure and Lamb shifts. In the dipole approximation the influence of an external electric field, $\underline{E}$, may be written as

$$H_2 = -e\,\underline{r}\cdot\underline{E} \tag{3.6,1}$$

The dominant contribution is due to the $2P_{1/2}$ level pushing the $2S_{1/2}$ level upwards. Contributions from all other levels and the continuum are small. For example, from the calculation used to derive the A.C. Stark shift with $\omega = 0$, the shift of the $1S_{1/2}$ level is found to be

$$\frac{\Delta E_{1S}}{h}\ (\text{quadratic}) \sim 10^{-4}\, E^2\ \mathrm{Hz}$$

where the units of E are Vcm^{-1}. This is negligible compared with the shift of the $2S_{1/2}$ level. Here a different approach is taken. Only the fine structure levels with n=2 are considered. The basis states for this calculation are the zero field Pauli-Dirac states with the energy levels corrected for the Lamb shift [24,25]. The matrix elements between the fine structure states $2S_{1/2}$, $2P_{1/2}, {}_{3/2}$ have been calculated and are displayed in Table 3.1. There is no matrix element connecting $2P_{3/2}(M_J=\pm\frac{3}{2})$ with the other levels so in this approximation this state is unshifted. The calculation proceeds as follows.

For an arbitrary field $\underset{\sim}{E}$ we may diagonalise the matrix represented in Table 3.1. This enables the field dependent eigenvalues and eigenvectors to be obtained. For this problem it is the eigenvalue which reduces to the 2S level in zero field that is of interest. It is simple to show that the determinant of the matrix is:

$$(L_3-\mathcal{E})\left\{(L_2-\mathcal{E})(L_1-\mathcal{E}) - 3S^2E^2\right\} - 6S^2E^2(L_2-\mathcal{E}) = 0 \tag{3.6,2}$$

where $\mathcal{E}$ is a solution of this cubic equation. Each of the solutions may be labelled by the level to which they reduce to in zero field. However, since states of different ℓ and j are mixed by the field $\underset{\sim}{E}$ the labels are not physically meaningful. The shifts of the three levels $2S_{1/2}$, $2P_{1/2}$, $P_{3/2}$ are shown in fig.3.1.

An additional effect of the electric field which may become important in measurements with higher resolution than obtained in this experiment is the reduction in the $2S_{1/2}$ lifetime [26,27]. The electric field mixes a small contribution of the $2P_{1/2}$ and $2P_{3/2}$ into the $2S_{1/2}$ wavefunction. After a time t where $\tau_{2P} < t < \tau_{2S}$ (τ_{2P} is the $2P_{1/2}$ lifetime and τ_{2S} is the $2S_{1/2}$ lifetime) the $2P_{\frac{1}{2},3/2}$ contributions have decayed leaving only the $2S_{1/2}$ contribution. It may be shown that the effective lifetime of the 2S level in a field E (in volts/cm) is

$$\tau_{2S}(\underline{E}) = \tau_{2P}\left(\frac{E}{475}\right)^{-2} \qquad (3.6,3)$$

This is only valid for intermediate fields where the lifetime is short compared with τ_{2S} but long compared with τ_{2P}. For sufficiently large fields the lifetimes of the $2S_{1/2}$ and $2P_{1/2}$ become $2\tau_P$ [27]. A field of 5 V/cm which was applied to detect the ions results in a 2S lifetime of 14 μS. This corresponds to a linewidth of 70 kHz which is unobservable in this experiment.

3.6.1. Experimental verification of D.C. Stark shifts.

Details of the experimental system used to examine the influence of electric fields on the $1S_{1/2}$-$2S_{1/2}$ frequency are given in Chapter 5. Only the experimental results will be discussed here. The object of this investigation was to verify (3.6,2) in order to confirm that the shift of the $2S_{1/2}$ level due to the small electric field required for the ionisation detection scheme was negligible.

The $1S_{1/2}-2S_{1/2}$ frequency was measured for three fields 10 Vcm^{-1}, 67 Vcm^{-1}, and 161 Vcm^{-1}. The results are shown in fig.3.1 together with the theoretical curve obtained from (3.6,2). Within the experimental accuracy the agreement is adequate. Improvements in the experimental accuracy would provide a better test of the theory.

The field used in the ionisation detection scheme was 5 V/cm. The corresponding shift in a quarter of the 1S-2S frequency was +23 kHz which is approximately 200 times smaller than the statistical error. For the present measurement the D.C. Stark shift may be ignored.

3.7. Pressure shifts of the $1S_{\frac{1}{2}}-2S_{\frac{1}{2}}$ frequency.

Pressure broadening and shifts occur when the presence of other atoms and molecules perturb the frequency and linewidth of the transition of interest. If the 1S-2S transition is ever to be probed at the 1 part in 10^{14} level, the shifts of the 1S-2S frequency will have to be well understood and controlled. There are no theoretical works which address the problem of the pressure effects on the 1S-2S frequency which is examined using two photon

Doppler free techniques. This section summarises the information that is available and describes an experimental measurement of the pressure shift in atomic hydrogen.

A simple view of the broadening process in three photon ionisation is as follows. Consider a laser tuned sufficiently far off the two photon resonance $\delta\nu = \nu_{12} - 2\nu_L$ that there is a negligible signal in the absence of collisions, ie. $\delta\nu > \Delta\nu_L$ where $\Delta\nu_L$ is the laser linewidth. The occurrence of collisions will tend to interrupt the interaction of the atom with the light field, so that instead of the interaction time being controlled by the inverse of the laser linewidth, it is limited by a time $\tau_c < \frac{1}{\Delta\nu_L}$. Thus the detuning $\delta\nu$ satisfies $\frac{1}{\tau_c} > \delta\nu > \Delta\nu_L$ the signal rate for this detuning will increase relative to the signal rate on resonance and the transition is broadened. Note that the signal rate decreases quadratically as the interaction time decreases so that the overall signal rate decreases. Estimates for the magnitude of this broadening are available [7,28]. In [28] a broadening 10 MHz/torr was obtained by analogy with inert gases. A slightly more quantitive estimate was made in [7], again giving a value of 10 MHz/torr. This analysis was based on the above simple picture that collisions cause an interruption of the interaction between the atom and the electic magnetic field.

In practise the collisional process is more complicated and for transitions probed by two photon

Doppler free techniques the broadening cannot be due to elastic collisions which merely change the atomic velocity, since the Doppler free component is independent of atomic velocity as noted in Section 3.3, [3]. The shifts and broadening arise through the perturbation of the energy levels of one atom by the electric field of an atom or molecule passing close by. Typically these might be attractive Van der Waals potentials which drop off as R^{-6}, or Coulombic fields which drop off as R^{-2} if the perturber is an ion where R is the atom - perturber separation. The effect of the electric field is firstly to Stark shift the energy levels of the atom and secondly to change the life time of the various levels either by mixing with a nearby level with a shorter lifetime, as discussed in Section 3.6, or by inducing transitions between nearby levels,[28].

The presure shift was measured by observing how the $^{130}Te_2$ to $1S_{1/2}-2S_{1/2}$ separation changed as a function of pressure. The separation was measured at 0.5 torr and 1.5 torr and the observed change found to be +3 ± 6 MHz/torr to higher frequencies. Since this shift was measured at 486 nm the total 1S-2S shift will be four times this value, or +12 ± 24 MHz/torr. At the normal operating pressure of 0.2 torr the shift is deduced to be +0.6 ± 1.2 MHz. The sign of the pressure shift is in agreement with the D.C. and A.C. Stark shift results and gives an increase in the 1S-2S frequency. The large error connected with this measurement can easily be reduced by improving the statistics by increasing the number of scans used in the analysis.

References.

[1] R. Loudon. "The Quantum Theory of Light". p334. Clarendon Press. 2nd.ed. (1983).

[2] V.S. Letokhov, V.P. Chebotayev. "Nonlinear Laser Spectroscopy". p155. Springer-Verlag. (1977).

[3] E.Giacobino, B. Cagnac. Progress in Optics. 17 85 (1980).

[4] P. Lorrain, D. Corson. "Electromagmetic fields and waves". p468. Freeman. 2nd.ed. (1970).

[5] E. Merzbacher. "Quantum Mechanics". p450. Wiley. 2nd.ed. (1970).

[6] L.I. Schiff. "Quantum Mechanics". p280. McGraw Hill. 3rd.ed. (1981).

[7] S.A. Lee. Ph.D. Thesis. M.L. Report No. 2460. Stanford University. (1975).

[8] Y. Gontier, M. Trahin. Phys. Lett. 36A 463. (1971).

[9] G.C. Bjorklund, C.P. Ausschnitt, R.R. Freeman, R.H. Storz. Appl. Phys. Lett. 33 54. (1978).

[10] C.P. Ausschnitt, G.C. Bjorklund, R.R. Freeman. Appl. Phys. Lett. 33 851. (1978).

[11] W.L. Glab, M.H. Nayfeh. Opt. Lett. 8 30. (1983).

[12] G. Grynberg, B. Cagnac, F. Biraben. "Coherent Nonlinear Optics: Recent Advances". p111. ed. M.S. Feld, V.S. Letokhov. Springer-Verlag. (1980).

[13] H.B. Bebb, A. Gold. Phys. Rev. 143 1. (1966).

[14] G. Peach. Mem. R. Ast. Soc. 71 13. (1967).

[15] G.C. Bjorklund, R.R. Freeman, R.H. Storz. Opt. Comm. 31 47. (1979).

[16] A.M. Bonch-Bruevich, V.A. Khodovoi. Sov. Phys. Usp. 10 637. (1968).

[17] E. Merzbacher. "Quantum Mechanics" p420. Wiley. 2nd.ed. (1970).

[18] V. Bunkin. J.E.T.P. 23 1121. (1966)

[19] W. Becher. Opt. Comm. 56 107. (1985).

[20] C. Wieman, T.W. Hansch. Phys. Rev.A. 22 192. (1980).

[21] H. Bethe, E. Saltpeter. "Quantum Mechanics of One- and Two- Electron Atoms". p262. Plenum. (1977).

[22] M. Stobbe. Ann.d.Phys. 7 661. (1930).

[23] J.E.M. Goldsmith. Ph.D. Thesis. M.L. Report No. 2955. Stanford University. (1975).

[24] J.A. Blackman, G.W. Series. J. Phys.B. 6 1090. (1973).

[25] G. Ludens. Ann. d. Phys. 6 308. (1951).

[26] H. Bethe, E. Saltpeter. "Quantum Mechanics of One- and Two- Electron Atoms".p286. Plenum. (1977).

[27] W.E. Lamb, R.C. Retherford. Phys. Rev. 79 547. (1950).

[28] E.V. Baklanov, V.P. Chebotaev. Opt. Spectrosc. 38 215. (1975).

[29] E.M. Purcell. Astrophysical J. 116 457. (1952).

Chapter 4. The $^{130}Te_2$ Saturation Spectrometer.

Diatomic molecules such as I_2, Na_2 and Te_2 have many transitions throughout the visible region. Cells containing I_2 at close to room temperature have been used as secondary frequency or wavelength standards for highly accurate measurements [1,2,3], and for stabilising lasers [4]. The advantage of using this type of standard over passive systems such as interferometers is that molecular transitions are relatively insensitive to the macroscopic perturbations present in a laboratory environment. A stabilised laser locked to a transmission maximum of an interferometer will inevitably follow the frequency drifts of that interferometer. If a laser is locked to a line in a molecular vapour, provided the cell pressure is regulated and no external perturbations such as magnetic fields are applied, there will be no long term drifts of the laser frequency. Additionally, it is possible for experimenters in different parts of the world to be sure that they have the same standard, because different samples of the same element have identical physical properties. Naturally there is a limit to this certainty, and for I_2 this corresponds to cases when accuracies better than 10^{-10} of the optical frequencies are required. Shifts of this order can be caused by foreign gas contaminants, wall temperature effects, stray magnetic fields and optical power shifts caused by the laser field.

For this experiment it was necessary to develop a frequency standard for use near 486 nm. This ruled out the use of I_2 since it starts to photodissociate at wavelengths below 500 nm [5]. $^{130}Te_2$ was an obvious choice since it had been used in previous experiments in the blue [6,7], and a comprehensive atlas of its absorbtion spectra was available [8]. One disadvantage of $^{130}Te_2$ is that it requires an elevated temperature in order to provide a sufficient number density. Fortunately the $^{130}Te_2$ can be used in a quartz cell which simplified the experimental apparatus [9].

The fluorescence spectrum of $^{130}Te_2$ when probed with a tuneable single frequency dye laser near 486 nm is rich, and bands fluorescing mainly in the green can easily be observed. Spacing of these bands is irregular but typically around 10 GHz. No attempt to identify these bands was made [10]. The widths of some of these bands is larger than might be expected from the Doppler broadening of a single line (0.8 GHz) and when observed using Doppler free techniques a multitude of lines separated by $\sim$300 MHz may be found.

This chapter outlines the methods used to observe the Doppler free transitions in $^{130}Te_2$ and specifies the experimental conditions under which the $^{130}Te_2$ standard was used.

Chapter 4.

4.1. Doppler free saturated absorbtion spectroscopy.

Doppler free saturated absorbtion techniques have been used for many years for high resolution spectroscopy. The details of this experimental method are outlined in many text books and review articles [11,12] so only a brief description is given here.

Doppler free saturated absorbtion spectroscopy is performed using two counter-propagating laser beams, normally of the same frequency in the laboratory frame of reference. One of the beams, called the pump, is of a higher intensity than the other beam, called the probe. The experimental cell is assumed to contain a gas of atoms with a resonant frequency close to the laser frequency. The transition being probed has a homogeneous linewidth much smaller than the Doppler width, so the resulting absorbtion is inhomogeneously broadened. Only those atoms which, due to their motion, see the laser frequency Doppler shifted into resonance can absorb a photon from one or other of the laser beams. If ν_L is the laser frequency and ν_T the transition frequency in the laboratory frame of reference, then

$$\nu_T = \nu_L \left(1 \pm \frac{V_x}{c}\right)$$

where V_x is the atomic velocity component along the axis

Figure 4.1.

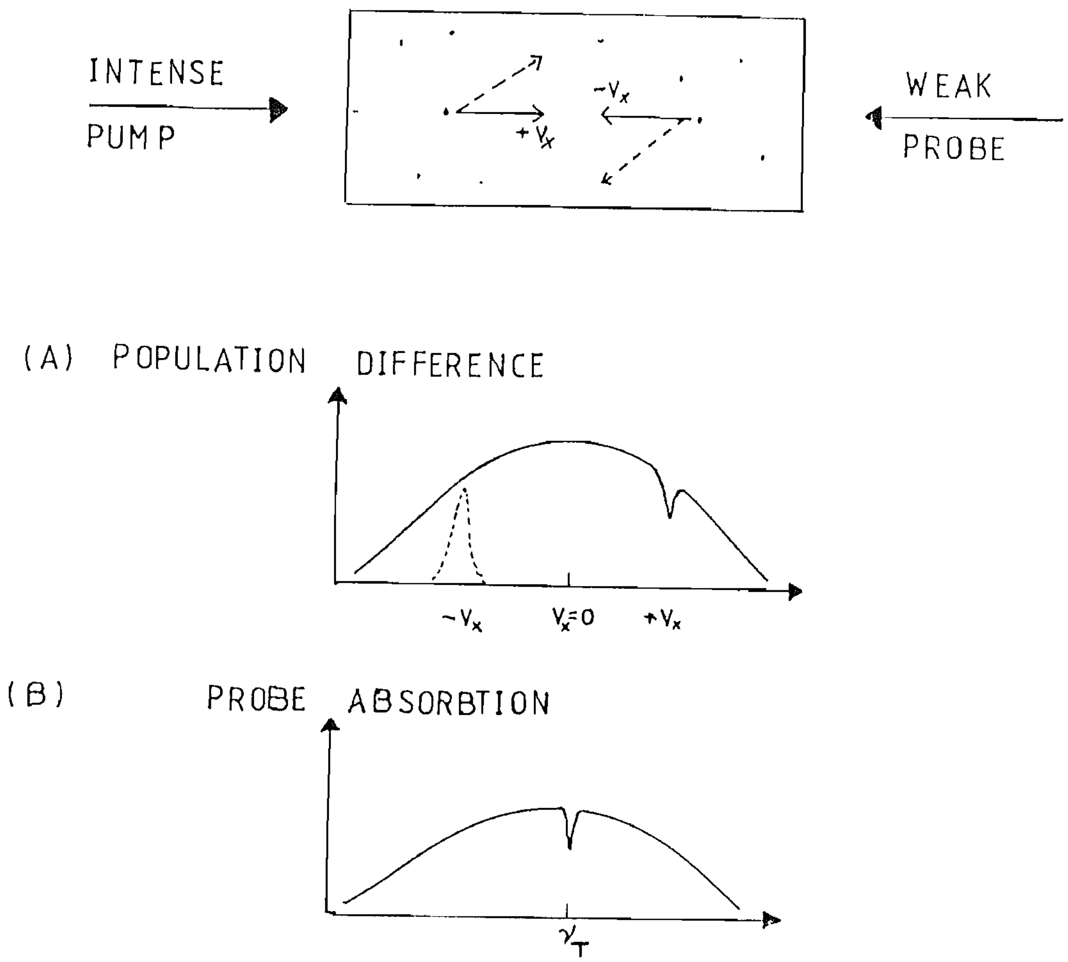

Figure 4.1.

Saturated absorbtion spectroscopy.

(A). Population difference hole burning by the laser beam.

(B). Resulting probe absorbtion showing the Doppler free decrease at ν_T.

defined by the counter-propagating laser beams. If the pump interacts with the $+V_x$ velocity class then the probe interacts with the $-V_x$ velocity class and the two counter propagating beams do not compete for the same atoms, providing $|\nu_L-\nu_T|>\Delta\nu_T$ where $\Delta\nu_T$ is the linewidth of the Doppler free transition that is observed. This is illustrated in fig.4.1. However, if $|\nu_L-\nu_T|<\Delta\nu_T$ then the two beams are competing for the same atoms. Assuming that the pump beam is sufficiently intense that it changes the ground state population of the velocity class with which it interacts significantly (it saturates the transition) then the probe beam will see a reduced absorbtion. The resulting line is narrower than the Doppler width of the transition and is composed of the homogeneous linewidth, the laser linewidth, and power and collision broadening effects. Since this method probes within the Doppler width of the transition it is often called Doppler free.

The experimental method is often more complex than outlined above. An additional laser beam may be sent through the cell in the same direction but spatially separated from the probe so it does not interact with the pump. This is subtracted from the probe intensity mainly to compensate for the laser intensity fluctuations, but also to remove the residual Doppler broadened changes in transmitted probe intensity. Also standard phase sensitive detection schemes may be used. The pump beam can be amplitude modulated at a selected frequency using an optical chopper and the difference between the probe and reference monitored for a component at this frequency. The modulation is transferred by the saturation of the transition described above. Another refinement is to observe changes in the polarisation of a linearly polarised probe when the pump is circularly polarised [13]. Polarisation spectroscopy, as it is called, can be much more sensitive than saturated absorbtion spectroscopy, but at a cost where the observed line shapes may be more dependent on the experimental conditions. In the experiment described here, the standard saturation absorbtion set up using pump, probe and reference beams and phase sensitive detection was used since it is simple and the signal to noise was adequate (20-80:1).

4.2. Doppler free $^{130}Te_2$ spectra.

The experimental arrangement used to obtain the $^{130}Te_2$ saturated absorbtion signals is shown in fig.4.2. Approximately 20-50 mw of single frequency light with a peak to peak linewidth of 1-2 MHz was provided near 468 nm. An acousto-optic modulator (Isomet) run at 80 MHz provided optical isolation between the saturation spectrometer and the dye laser. This enabled colinearity of the counter-propagating beams to be maintained over a long path length and reduced any residual Doppler broadening due to the crossing angle of the pump and probe. If the acousto-optic modulator was omitted, the pump beam could feed back into the dye laser causing amplitude and frequency instabilities. The acousto-optic modulator also had the effect of increasing the frequency of the light used in this part of the experiment by 80.00 MHz. A suitable correction for this had to be applied in the final stages of data analysis (Section 6.1).

Tellurium of 99.3% isotopic purity was contained in an evacuated fused silica cell (80 mm × 25 mm diameter) with normal incidence windows [14]. The cell had been baked to 1100 C and evacuated to 10^{-6} torr (10^{-5} Pa) prior to filling. No detailed information regarding the level of contaminants within the cell following the filling and sealing, or during any subsequent heating, was available. The cell wall was heated to 643°C via a 10Ω nichrome heater wire which was non-inductively wound. Insulation was provided by a layer of silica glass fibre between the heater and the cell body and two layers of the glass fibre over the heater. The complete assembly was wrapped with allumina coated paper. The temperature was monitored by a cold junction compensated chromel-alumel thermocouple fixed to the thermally insulated outer wall of the cell body. It was presumed that the tellurium equilibrium vapour pressure was determined by the temperature of the cell windows,

Figure 4.2.

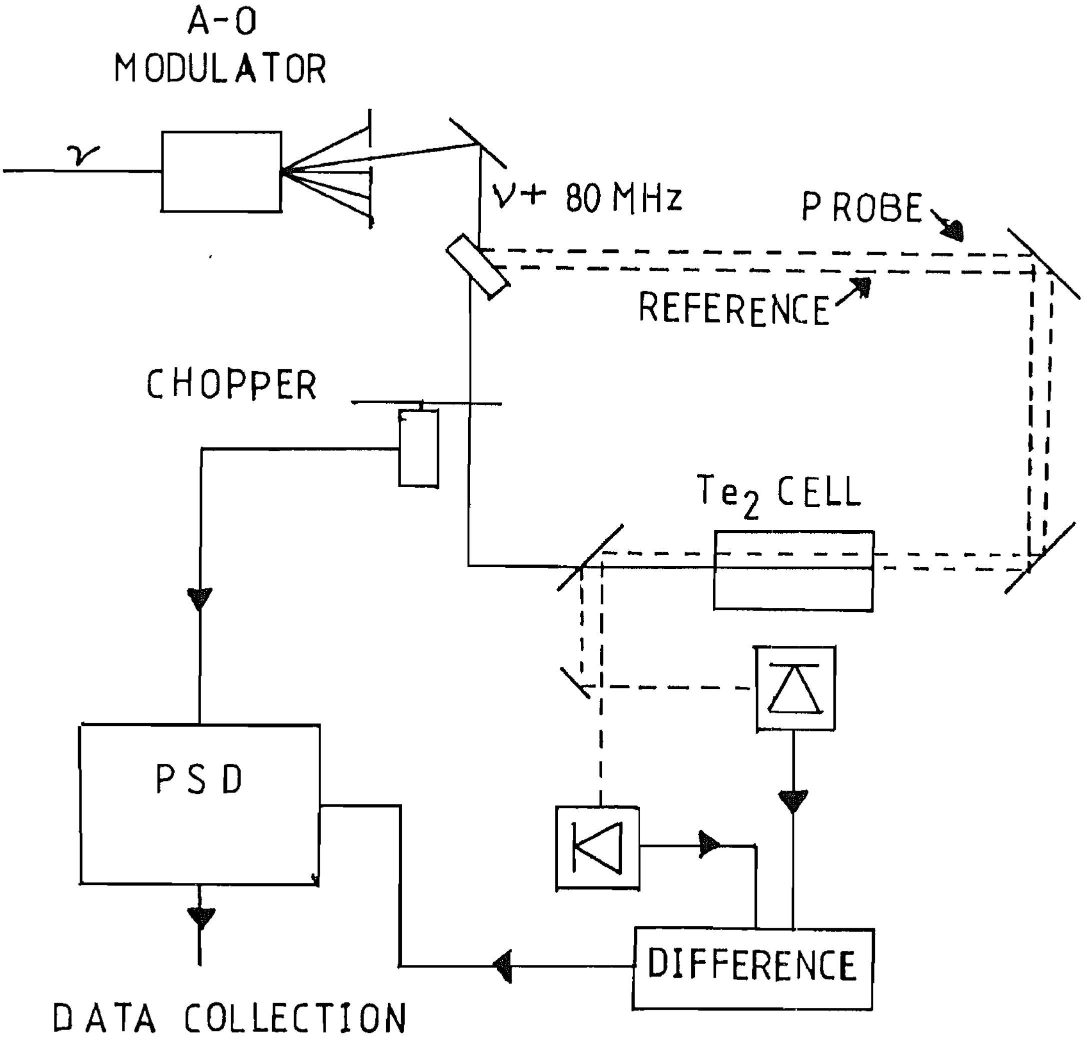

Figure 4.2.

Experimental arrangement used to obtain the $^{130}Te_2$ spectra and to provide the absolute frequency standard.

since these were not lagged and there was no "cold finger" side arm. This premise was in agreement with the observation of tellurium condensate there. Initially it was attempted to measure the temperature differential between the cell body and windows by observing the known tellurium melting point and assuming a proportional variation of this differential with respect to the measured temperature above ambient. This assumption was later found to be invalid with the differential being much larger than the measured -18°C. To ensure reproducibility of the frequency standard, the absorbtion of a low power beam (<1 mw) at a fluorescent band with only one major Doppler free component was measured using the standard operating conditions. The absorbtion and conditions are discussed later.

The saturated tellurium spectra in the vicinity of the deuterium and hydrogen transitions are shown in fig.4.3. These are produced by overlapping a 6 mw chopped pump beam with a 0.4 mw probe beam counter-propagating through the cell. The beams were focussed to waists outside the cell and the saturating and probe beam radii ($1/e$ amplitude point) in the cell ranged from 0.28 mm to 0.24 mm and 0.20 mm to 0.13 mm respectively. A reference beam identical to the probe but displaced was used to subtract off the laser intensity noise and linear absorbtion background from the detected probe. The Doppler free spectra were then recovered using standard phase sensitive detection methods.

The probe beams were slightly smaller than the pump beams in order to prevent convection induced probe beam wander relative to the saturating beam which otherwise resulted in a variation of the saturated signal amplitude.

Careful consideration was given to the choice of tellurium saturated components to be used for calibration. Use of saturated features with the narrowest linewidths should optimise the short term stability of a tellurium stabilised dye laser. The spectra of fig.4.3 exhibit linewidths (full width at half maxima) in the range of 20-100 MHz. By comparison, linewidths of 1-5 MHz were typical for saturated absorbtions in iodine [15]. Further, good long term reproducibility is required. As a result some of the features in fig.4.3 were deemed unsuitable due to unexpected temperature behaviour (eg. component h_2) or to magnetic field dependence. In this latter case an inductive heater winding used in a preliminary study resulted in an axial field induced 100 MHz modulation to the a_2 and d_2 features. These were discounted although the heater was rewound non-inductively. The components chosen for calibration were b_1 and b_2 which lie roughly 4.2 GHz and 1.4 GHz respectively below the frequencies equal to a quarter of the 1S-2S transitions in deuterium and hydrogen. The fwhm linewidths were measured to be 20 MHz and 34 MHz for b_1 and b_2 respectively.

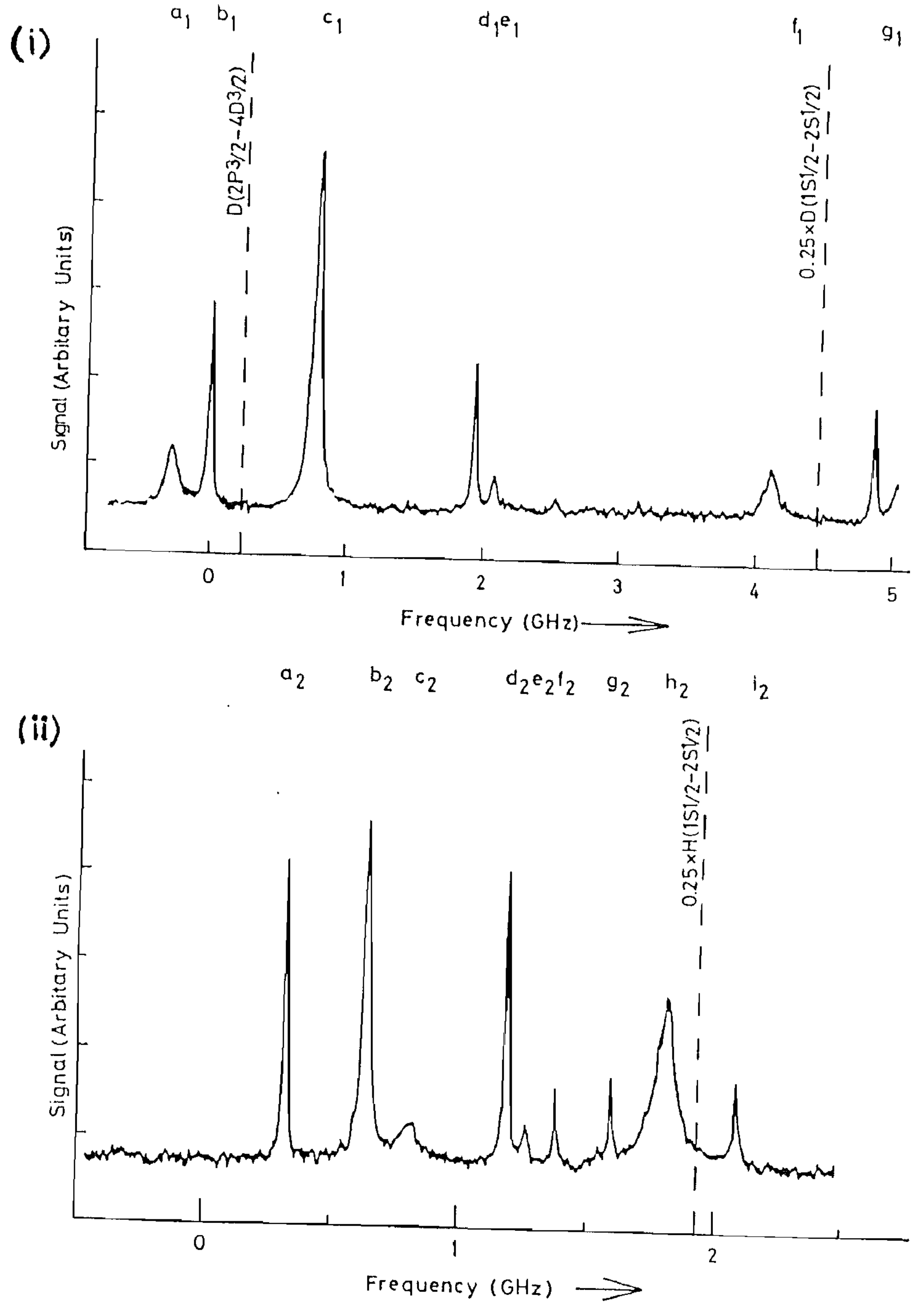

Figure 4.3.

Doppler free $^{130}Te_2$ spectra near 486 nm in (i) deuterium and (ii) hydrogen showing the calibrated components (b_1 and b_2). The approximate position of one quarter of the centroid of the 1S-2S transition frequency is also shown.

4.3. Interferometric frequency measurements.

The calibration of the tellurium Doppler free components b_1 and b_2 was carried out at the National Physical Laboratories in London. The frequency of a dye laser locked to a tellurium line was interferometrically compared with the 633 nm light from a HeNe laser stabilised to component "i" of the 11-5 R(127) transition in $^{127}I_2$. The iodine stabilised laser was an NPL reference laser and was operated under preferred reference conditions. It had a resettability of 1 part in 10^{11} and its frequency was within 4×10^{-11} of the mean of a number of lasers from other national laboratories with which it had been compared. The reference interferometer was a 1 m long plane-plane Fabry-Perot interferometer which was evacuated. The phase shifts on reflection of the mirror coatings (Appendix B) and other properties are well characterised [16,17,18].

The full experimental process is outlined in [19], only a brief description is given here. Preliminary frequency measurements of the dye laser stabilised at 486 nm to the chosen tellurium components were made using a moving arm Michelson Interferometer wave meter [20] to 5 parts in 10^8 (30 MHz). This was within the accuracy necessary to unambiguously determine the correct order number at 486 nm for the 150 MHz free spectral range reference interferometer. Two HeNe reference lasers were used. One is the iodine stabilised laser mentioned earlier, the other is locked to a transmission maxima of the reference interferometer. The beat frequency between these two lasers is observed. The etalon length is changed to bring it into resonance with the dye laser at 486 nm and the offset between the two HeNe lasers is noted. Given that the phase shifts on reflection are known at 633 nm and may be extrapolated to 486 nm then the ratio of the frequencies of the dye laser and the reference HeNe laser may be found. From this result the frequency of the dye laser locked to a tellurium component may be calculated using the known reference HeNe frequency. The measured frequencies of components b_1 and b_2 are

$$f(b_1) = 616\ 678\ 857.5 \pm 0.25 \text{ MHz}$$
$$f(b_2) = 616\ 513\ 896.3 \pm 0.25 \text{ MHz}$$

The uncertainties correspond to one standard deviation and are made up as follows:

reference laser	34×10^{-11}
observation statistics	8×10^{-11}
phase shift extrapolation	16×10^{-11}
other [19]	11×10^{-11}
Total (root sum of squares)	40×10^{-11}

The largest individual uncertainty was in the definition of the reference laser frequency. This could be reduced if an improved HeNe laser frequency is measured. The phase shift were extrapolated from nine measurements betwen 670 nm and 514 nm and the error arises from the difference between a cubic, quartic and exponential fit to these measurements. The observation statistics are larger than normally found with this interferometer. This is related to the larger linewidth of the tellurium components compared with iodine lines and the consequent uncertainty in the lock resettability. The remaining errors arise from residual effects in the interferometer optics and cell temperature drifts. The saturating beam power dependence of the measured frequency was measured between 3 mW and 9 mW and gave rise to shift which was not statistically significant.

It was not possible to carry out long term observations of the frequency of the measured components. A build up of foreign contaminants in the cell due to prolonged exposure to high temperatures is possible. Similarly, it was not feasible to intercompare different tellurium cells which would give information on the cell to cell reproducibility and on the variations in foreign contaminant levels. Such a method, utilising the Hanle effect, is used in iodine [21].

4.4. The operating conditions.

During the hydrogen $1S_{1/2}$-$2S_{1/2}$ experiments the tellurium spectrometer was used with the following conditions. The cell wall temperature at the point used in the calibration was maintained at 640-645 °C. However, as has been mentioned earlier, there was a problem in determining the "cold finger" temperature. To ensure that future experiments use the same conditions the absorbtion of a low powered probe was measured at this temperature. The experimental set up used is shown in fig.4.4, and fig.4.5 demonstrates the position of the fluorescent band for which the absorbtion was measued. It lies approximately 9 GHz lower in frequency than the calibrated hydrogen line and was chosen because it contains one strong Doppler free line which is 20 times stronger than any other components lying under this band. The absorbtion was 23.4 ± 1.4 %.

Figure 4.4.

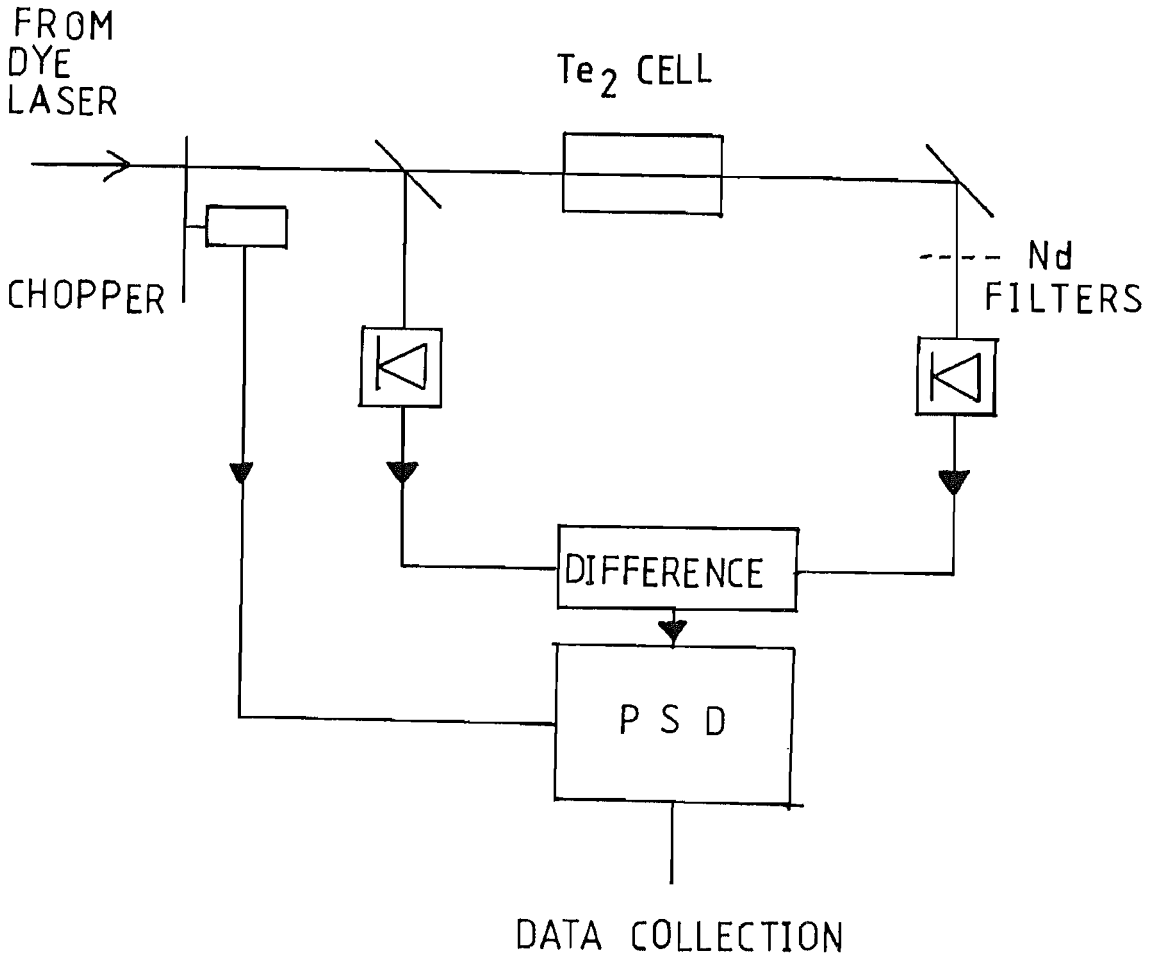

Figure 4.4.

Experimental arrangement used to obtain the linear absorbtion at the calibrated temperature.

Figure 4.5.

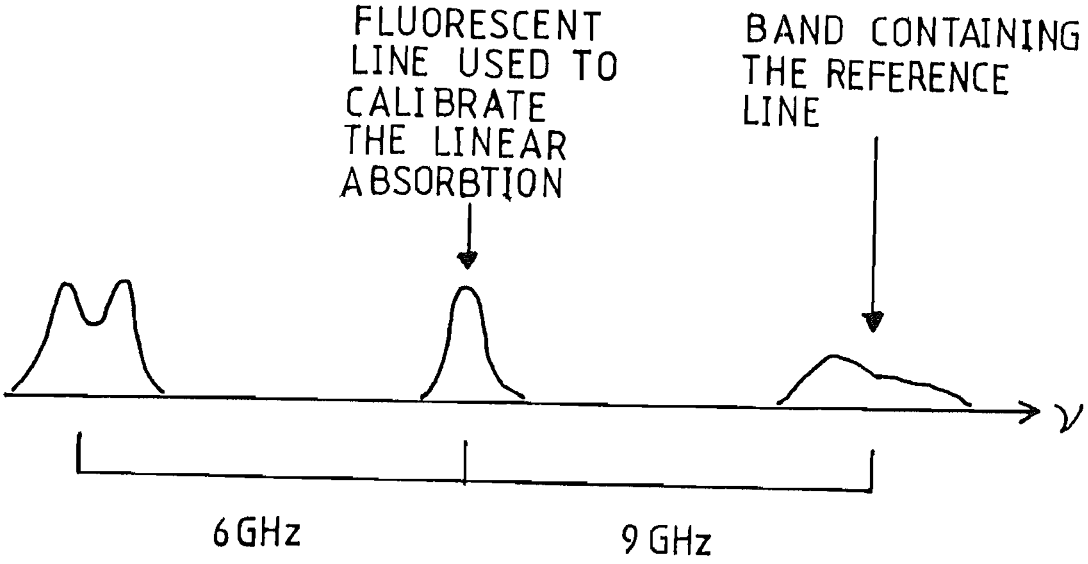

Figure 4.5.

Location of the fluorescent line used to measure the linear absorbtion.

References.

[1] J.E.M. Goldsmith, E.W. Weber, T.W. Hänsch. Phys. Rev. Lett. 41 1525. (1978).

[2] B.W. Petley, K. Morris, R.E. Schawyer. J. Phys. B. 13 3099. (1980).

[3] S.R. Amin, C.D. Caldwell, W. Lichten. Phys. Rev. Lett. 18 1234. (1981).

[4] A.J. Wallard. J. Phys. E. 6 793. (1973).

[5] S. Gestebkorn, P. Luc. "Atlas du Spectre d'Absorbtion de la molecule d'Iode". Lab. Aime-Cotton. C.N.R.S. Orsay. France.

[6] S. Chu, A.P. Mills. Jr. Phys. Rev. Lett. 52 1689 (1984).

[7] T.J. Stone, R.F. Barrow. Can. J. Phys. 53 1976. (1975).

[8] J. Cariou, P. Luc. "Atlas du Spectre d'absorbtion de le molecule de tellure". Lab. Aime-Cotton. C.N.R.S., Orsay, France. (1980).

[9] B. Wellegehausen, D. Friede, G. Steger. Opt. Comm. 26 391. (1978).

[10] R.F. Barrow, R.P. du Parq. Proc. R. Soc. Lond. A. 327 279. (1972).

[11] V.S. Letokhov, V.P. Chebotayev. "Nonlinear Laser Spectroscopy". Springer-Verlag. (1977).

[12] J.H. Shirly. Phys. Rev. A8 347. (1973).

[13] C. Wieman, T.W. Hänsch. Phys. Lett. 36 307. (1975).

[14] Opthos Instruments Inc. Maryland. MD 208JJ. USA.

[15] G.R. Hanes, C.E. Dahlstrom. Appl. Phys. Lett. 14 362. (1969).

[16] P.T. Woods, K.C. Shotton, W.R.C. Rowley. Appl. Optics. 17 1048. (1978).

[17] G.P. Barwood, W.R.C. Rowley. Metrologia. 20 19. (1984).

[18] G.P. Barwood, W.R.C. Rowley, P.T. Woods. Metrologia. 20 157. (1984).

[19] J.R.M. Barr, J.M. Girkin, A.I. Ferguson, G.P. Barwood, P. Gill, W.R.C. Rowley, R.C. Thompson. Opt. Comm. 54 217. (1985).

[20] S.J. Bennet, P. Gill. J. Phys. E: sci instrum. 13 174. (1980).

[21] W.R.C. Rowley, B.R. Marx. Metrologia. 17 65. (1981).

Chapter 5. The Experimental Equipment.

The experiment consisted of three sections: the hydrogen 1S-2S experiment, the tellurium saturation spectrometer and the reference interferometer. In this section the laser system and the equipment used in the experiment are described and the experimental procedure is outlined. The equipment is schematically shown in fig. 5.1 which has references to the section of this chapter where each component is described.

5.1. The laser system.

The c.w. 486 nm radiation was generated by a krypton ion laser (Coherent Cr 3000 K) pumping a coumarin 102 (C102) dye laser. The krypton laser typically ran all lines in the violet (406.7 nm, 413.1 nm, 415.4 nm) and produced 2-3 Watts. The C102 dye laser was a commercial ring dye laser (Coherent 699-21). In the later parts of the experiment it was converted to standing wave operation. The reason for this was that the threshold was lower so the krypton laser could be operated at reduced powers (1.5-2 W as opposed to 3 W), which proved a more reliable system. Also the day to day operation of a standing wave laser is easier and less time consuming than the ring laser. This proved important in the data collection process in the latter part of the experiment. The reduction in single frequency power in the standing wave laser as opposed to

Chapter 5.

Figure 5.1.

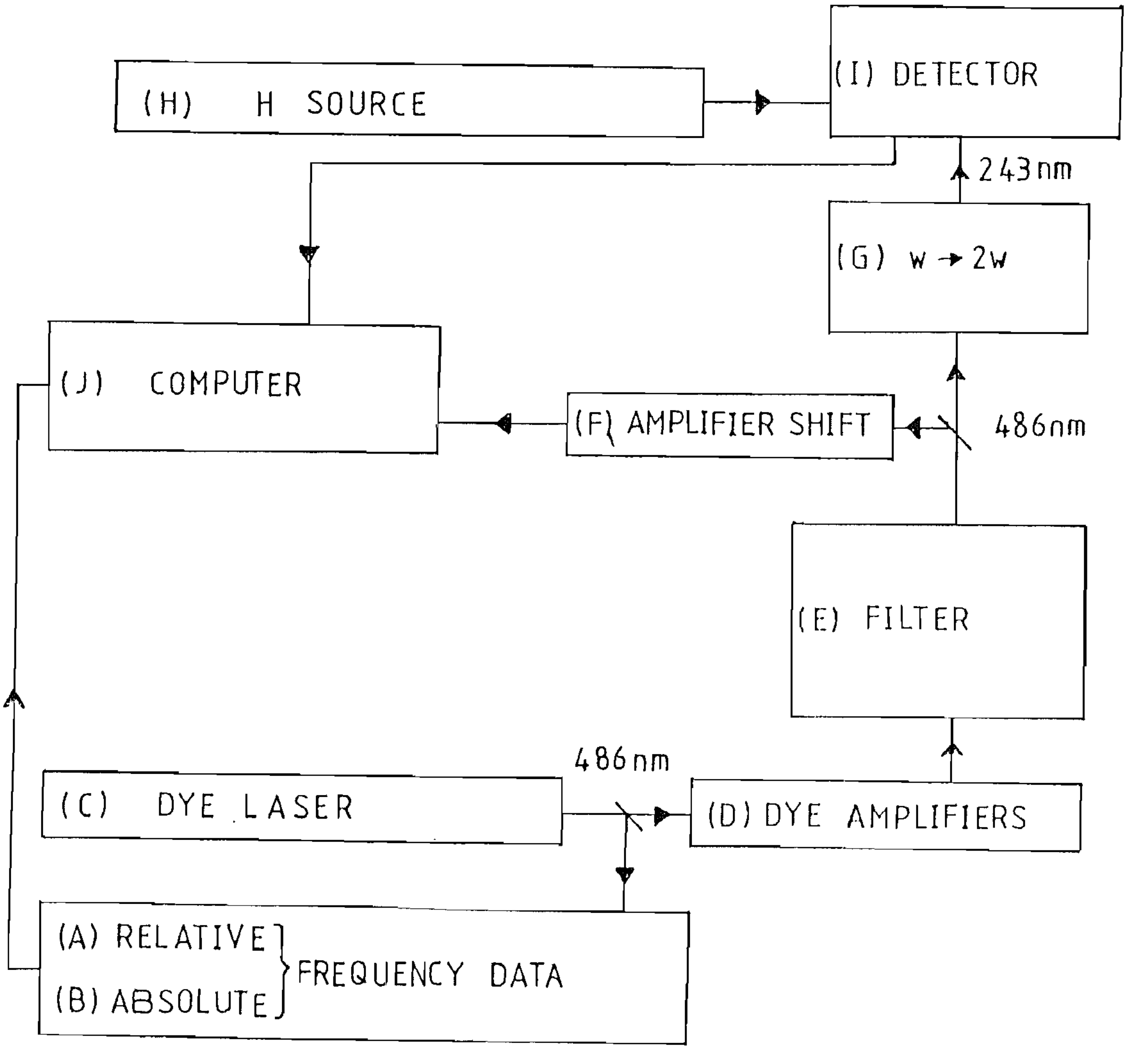

Figure 5.1. Schematic diagram of the experiment.

(A) Section 5.7
(B) Chapter 4
(C) Section 5.1
(D) Section 5.2
(E) Section 5.3

(F) Section 5.3.3
(G) Section 5.4
(H) Section 5.5
(I) Section 5.6
(J) Section 5.8

the ring laser (150 mw to 75 mw) was not a constraint in this particular experiment. However, if a grand experiment was envisaged in which the 1S-2S spectra, the Balmer spectra and the tellurium spectra were recorded simultaneously, then the power limitations of a single frequency standing wave laser might be a problem.

The standard dye laser system ensured single frequency operation by using three line narrowing filters: a birefringent filter and two etalons. Stabilisation of the laser was achieved by locking the laser to an external confocal etalon. The laser frequency was scanned by changing the length of the confocal interferometer by rotating an internal Brewster plate. Since the laser was locked to this cavity its frequency followed the cavity resonant frequency. The control electronics allowed the laser to be scanned over a frequency region of up to 30 GHz ($1 cm^{-1}$) in times ranging from 0.25 s to 600 s. Scanning the laser tended to broaden the laser linewidth to about 7 MHz. This was attributed to irregular rotations of the Brewster plate and nonlinearities and instabilities in the ramp voltage driving the Brewster plate galvanometer. Pressure scanning of the reference cavity was tried to see if any reduction in linewidth occurred [1]. The refractive index n in the cavity is related to pressure by the Clausius-Mossotti relation [2]:

$$\frac{n^2-1}{n^2+2} = \frac{4\pi N\alpha}{3}$$

where N is the number of molecules per unit volume and α is the mean polarisability of each molecule. N is related to the Pressure P, so assuming for air $n \sim 1$

$$n-1 = KP \qquad K = \text{constant}$$

and the refractive index is approximately linear with pressure. The resonance condition for a confocal interferometer is (Appendix B)

$$\frac{m\lambda}{2} = 2L$$

and λ is independent of n. However, on passage into another medium of fixed refractive index n_0, the output wavelength λ_0 is related to λ by

$$n_0\lambda_0 = n\lambda$$

Since λ and n_0 are fixed, a change in n means λ_0 also changes. The wavelength change $\Delta\lambda_0$ is

$$\Delta\lambda_0 = \frac{\Delta n}{n_0}\lambda = K'\Delta P\lambda \qquad K' = \text{constant}$$

If the gas in the reference cavity is nitrogen then the frequency change is 226 MHz/torr [3]. Thus if the required scan range is 2 GHz the pressure change will be ~ 10 torr which is rather small. Notice that the free spectral range of the interferometer does not enter into the final result.

The modifications required to pressure scan the dye laser were modest. The reference cavity was already hermetically sealed otherwise the laser frequency would be sensitive to small atmospheric pressure changes. The major modification was to replace the original lid with a homemade lid which had a pressure fitting built in. Additionally the galvanometer body was raised slightly from the base of one of the two internal chambers to allow free gas flow between them. The advantage of being able to combine both pressure and electrical scanning mechanisms in one container is that the electrical scanning is more convenient for initial tuning in to a given frequency. Pressure scanning is then available for the actual experimental runs. The pressure in the reference cavity was monitored using a water filled manometer. For simplicity the reference cavity was pressurised using a syringe and allowed to leak out of a needle valve. The scan linearity was measured by monitoring the transmission fringes of a 75 MHz confocal interferometer. If the frequency of the laser varies smoothly with time it should have been possible to fit a curve to the separations between the interferometer peaks. In practice it was found that the error in the fit was comparable to electrical scanning indicating that the random frequency fluctuations were similar. Part of the reason for this result is that the locking electronics have to work harder when the frequency is pressure scanned than when it is electronically scanned.

It is possible to derive a feed forward signal when electrically scanning which smoothly adjusts the tuning and stabilisation filters so that the locking circuits only have to deal with small detunings of the laser frequency from the reference cavity resonant frequency. When pressure scanning using the simple set up described above no feed forward was generated and the locking electronics had to compensate for the total change in resonance frequency of the reference cavity. This led to periodic relocking events when the voltage on the various stabilisation elements reached a maximum value and were automatically zeroed. A feed forward could be generated by monitoring the pressure in the reference cavity using a capacitive manometer and applying this to the stabilisation electronics.

The laser dye, coumarin 102, had a relatively short useful lifetime and required to be changed after 50-100 Whrs. Photodissociation products tended to increase the losses and reduce the output power. The concentration was 0.75 g/l and the circulator contained approximately 1 litre of solution. The dye was initially dissolved in 100 ml of benzyl alcohol then added to ethylene glycol (ethandiol) in the dye circulator while monitoring the laser power. Maximum power normally corresponded to a pump light absorbtion of 60-70% in the dye jet. The krypton laser was one of the most troublesome components in this experiment. The most frequently occuring failure mode was non user serviceable and required a new laser tube. The

Brewster windows on the tube gradually coated on the inside. This coating absorbed in the violet and U.V. causing thermal lensing which reduced the output and beam quality. Laser tubes lasted, on average, 4.5 months with eight tubes being used over the three years of the experiment.

5.2. Pulsed amplification.

The low power c.w. beam from the dye laser was amplified to high peak powers using a pulsed, single pass, four stage, transversely pumped dye amplifier chain. The dye cells were pumped by a frequency tripled Q-switched Nd:YAG oscillator-amplifier system (Quanta Ray DCR 2 (10)). This laser generated up to 0.7 J in a 7 ns pulse length at 1064 nm. Subsequent frequency doubling and mixing gave 150 mJ in a 5-6 ns pulse length at 355 nm.

5.2.1. The dye amplifier chain.

The amplification process has been well treated in the literature [1,5,6,7,8] and only a brief outline will be given here. Pumping of a dye cell, using a several nanosecond pump pulse can create a population inversion which can be used to amplify an input signal. In common with all amplifying processes the output consists of an amplified version of the input signal, (the amplifying process may introduce temporal, spectral and spatial distortion) and a noise signal. The experimental considerations leading to the amplifier system illustrated in fig.5.2 are designed to optimise the amplification by reducing the associated distortions and the background noise. The background noise is due to amplified spontaneous emission (ASE) which, as its name suggests, is caused by excited dye molecules relaxing to their ground state and emitting a photon by spontaneous emission. Since this photon emission was not stimulated it is completely unrelated to the input signal. It may however experience the same gain as the input signal and be amplified to an inconveniently large level. If its growth is not limited it may saturate the gain, thus reducing the gain experienced by the signal. It is shown in [5] that the maximum single pass gain G, before gain is limited by ASE, is independent of the dye parameters and dependent only on the geometric properties of the excited region:

$$\frac{G}{\sqrt{\ln G}} \approx \frac{L^2}{R^2} \qquad (5.2,1)$$

where R and L are the radius and length of the active medium respectively. This result only holds for weak pumping and for exponential gain, which means that the gain is not saturated by by the amplifying process.

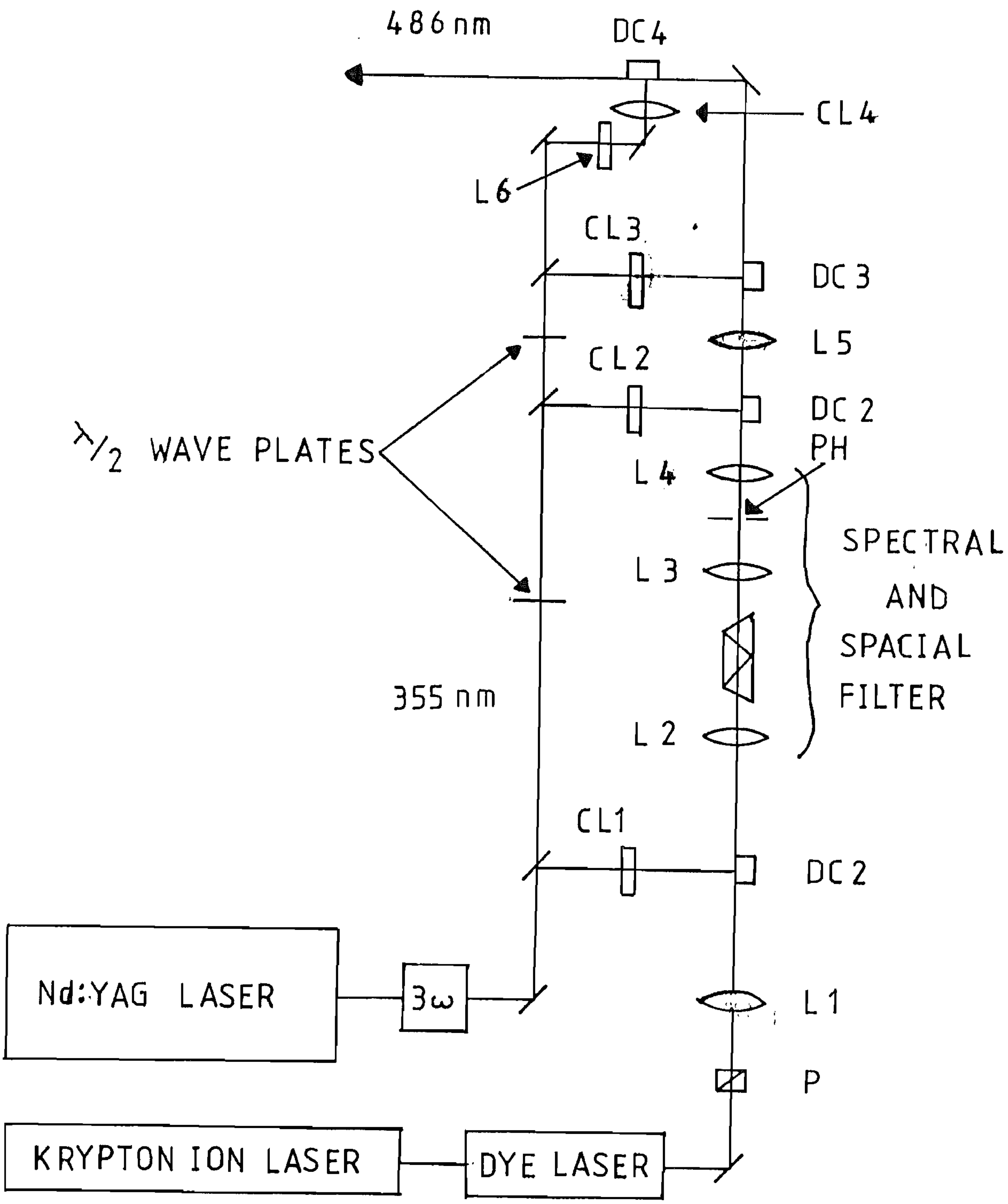

Figure 5.2. Dye amplifier system.

L1	10 cm	L6	-15 cm
L2	8 cm	CL1	15 cm
L3	3.3 cm	CL2	15 cm
L4	6 cm	CL3	5 cm
L5	4 cm	CL4	5 cm

For the dye cells used in the early stages of amplification L=1 cm and $R \sim 0.1$ mm, $\Rightarrow G \sim 3\times10^4$. Typically the measured gain ranged from 5×10^3 to 10^4. In the second and subsequent stages of amplification (5.2,1) does not apply since the gain is saturated by the amplification process and the weak pumping condition does not apply. Secondly, in these stages the ASE does not grow from the background noise but is injected together with the signal from the previous stage. However the same geometric considerations do apply. The active medium should be long and thin to reduce the probability of a spontaneously emitted photon being amplified.

Transversely pumped dye cells introduce inhomogeneity in the spatial distribution of energy in the amplified beam. This is due to the non uniform gain distribution within the active region. The gain is highest closest to the front surface of the dye cell, consequently the signal in this region experiences a higher gain. The front surface of the dye cell can act as a diffraction edge which introduces intensity fluctuations across the beam profile. Careful alignment and spatial filtering can compensate a little for these defects.

Amplification can also chirp the frequency of the pulse. This process has not been generally discussed in the literature since it is only a problem when amplifying narrowband c.w. dye lasers and using the light in experiments where the c.w. frequency is being compared with the pulsed frequency [9,10,11].

Approximately one third of the vertically polarised light from the dye laser, 10-20 mw, was passed through a polariser and focussed (f=10 cm) to a 55 μm ± 10 μm radius spot in the first dye cell. The polariser was optional and was used to reduce the backward travelling ASE to a level where it did not perturb the dye laser stabilisation. The 355 nm light from the Nd:YAG laser was horizontally polarised and the front surface reflection from a quartz plate was used to pump the dye cell ($\sim$1%, 1-2 mJ). It was focussed to a 1 cm long line using a quartz cylindrical lens (f=15 cm). The position and rotation of the lens optimised the amplification (5×10^3 - 10^4). The output of the first cell was collimated and passed through a direct view dispersing prism, which spatially separated the ASE from the amplified light. A 3.3 cm lens focussed the light onto a screen with a 100 μm pinhole. This provided spatial and spectral filtering and reduced the ASE background to 1/200 - 1/500 of the amplified signal level. The transmitted light was collected and focussed (f=6 cm) to a 180 ± 10 μm spot size in the second stage. The 355 nm $\lambda/2$ plate was used to rotate the polarisation incident on the quartz plate and thus vary the reflectance to enable optimisation of the signal amplification and ASE to be made. Typically 1-7 mJ reached the dye cell and gave a saturated gain in the region of 100. The output of this stage was collected and focussed into the third stage (180±20 μm) and allowed to expand into the final stage (650±50 μm). A second λ/2 plate rotated the pump polarisation until it was vertical and pumped the third stage with ~7 mJ. The rest of the pump energy (~30 mJ) was used to pump the final stage where it was expanded and focussed to a 2 cm long line to match the final cell length. The final stages gave comparable gains of 20-50 giving an overall gain in the region of 2×10^7. Losses and absorbtion in the dye cells account for the discrepancy between the gain each stage gave and the overall gain. The total amplification process was not particularly efficient and could be improved. The output of the Nd:YAG was 70 mJ per pulse of which about half reached the dye cells. This gives an energy conversion of 3.5% which was adequate for this experiment.

Flowing dye cells were essential to prevent thermal lensing in a system operating at 10 Hz. The first two cells share the same circulator and dye concentration: 0.7 g/l of C102 in methanol. The third stage dye concentration was 0.5 g/l and the final stage concentration was 0.2 g/l. Variations in the dye concentration of ~25% did not change the overall performance.

The amplifier typically produced 1.0-1.3 mJ per pulse with a background of ASE between 10%-30%. The pulse length is about 5 ns which is shorter than the pump pulse length of 7 ns. The spectral properties of the pulse were measured using confocal interferometers of 1.5 GHz and 300 MHz free spectral ranges and resolutions of 15 MHz and 2 MHz respectively. The linewidth was measured to be 150-200 MHz which is approximately 2 to 2.5 times the Fourier transform limit. Pulse broadening effects could be due to intensity modulations of the pump [4] and to the frequency chirp experienced in the amplification process. The frequency chirp varied on a day to day basis but was normally in the region of 30-55 MHz.

A simple model of the contributions to the amplifier chirp will be analysed. Consider a dye cell transversely pumped by a short pulse. The gain experienced by light passing through the cell increases to ~10^3 in times ~1 ns. The light propagates in the cell according to [12]

$$E = E_0 \, e^{+\frac{\gamma}{2} z} \, e^{i(\omega t - (k + \Delta k) z)} \qquad z = 0, L \qquad (5.2,2)$$

where L is the length of the dye cell (L=0.01 m), γ is the intensity gain coefficient related to the imaginary part of the complex susceptibility $\chi''(\omega)$:

$$\gamma(\omega) = - \frac{k \chi''(\omega)}{2 n^2}$$

n is the refractive index far from resonance. k is the wavevector of the wave assuming a refractive index n. Δk is the change in wavevector caused by the pumping and assuming that the dye cell is sufficiently short that changes in the population inversion during the passage of light is small.

$$\Delta k = \frac{k\chi'(\omega)}{2n^2}$$

where $\chi'(\omega)$ is the real part of the complex susceptibility

$$\chi(\omega) = \chi'(\omega) - i\,\chi''(\omega)$$

The real and imaginary parts of the complex susceptibilty are related through the Kramers-Kronig relations [12] by

$$\chi'(\omega) = 2\,\frac{\omega_0-\omega}{\Delta\omega}\,\chi''(\omega)$$

where ω_0 is the resonance frequency and $\Delta\omega$ is the full width ay half maximum of the absorbtion curve.

The frequency chirp $\delta\omega$ is given by

$$\delta\omega = -\frac{1}{2}\,\frac{\omega}{c}\,\frac{L}{n}\,\frac{d\chi'}{dt} = \frac{\omega_0-\omega}{\Delta\omega}\,L\,\frac{d\gamma}{dt}$$

An expression for γL is

$$\gamma L = \ln\left[1 + G\,e^{-t^2/\tau^2}\right]$$

where G is the gain of the cell [$G \sim 10^3$] and τ is the time of the pumping pulse ($\tau \sim 3$ ns). For $\left|\frac{t}{\tau}\right| < 2$ the time differential $\frac{d\gamma}{dt}$ is

$$\frac{d\gamma}{dt} = \frac{G\,e^{-t^2/\tau^2}}{1 + G\,e^{-t^2/\tau^2}}\left[-\frac{2t}{\tau^2}\right] \sim -\frac{2t}{\tau^2} \sim \pm\,0.6\times10^{9}\,s^{-1}m^{-1}$$

The magnitude of the resulting frequency chirp for $t=\tau$ is 1 MHz if $\omega_0-\omega\sim\Delta\omega$. The sign of the chirp is positive on the leading edge of the pulse ($t<0$) and negative on the falling edge. As the model stands it leads to a symmetrical broadening of the spectrum and does not predict a shift as observed in the experiment. Additionally the predicted chirp is an order of magnitude smaller than the measured shift (~ 30 MHz).

A number of comments on this calculation are appropriate. The model only considers a single dye cell whereas the dye amplifier chain consists of four cells each pumped by different energies. The relative timings of the pump and the amplifier pulse passing through each cell may play a role in reducing the effect of the trailing edge chirp thus giving the pulse frequency a net positive shift. The model assumes that the Kramers-Kronig relations are valid, which is not true in the presence of saturation [12] which is an important consideration in the second and subsequent dye cells. Additionally it is not clear that the Kramers-Kronig relations in the form used here are valid for a dye emission band. The important result is that the refractive index changes occuring during a pump pulse causes a frequency shift and the calculated chirp has roughly the right order of magnitude.

A further mechanism that can cause a frequency shift is the frequency dependence of the gain coefficient $\gamma(\omega)$. The gain is higher for frequency components closer to ω_0 , [13]. An estimate of the shift due to this process gives a value $\sim 10^3$ too small.

5.3. The line narrowing interferometer.

The linewidth of the pulsed light from the amplifier system was measured to be in the region of 150-200 MHz using a 1.5 GHz confocal interferometer with a 15 MHz passband. This limited the experimental resolution to 20 MHz in the blue (3 parts in 10^8), With the availability of more efficient doubling crystals (see Section 5.4) the possibilty of line narrowing the pulsed light by passing it through a confocal interferometer was considered. The transmitted light would acquire the linewidth characteristic of the interferometer passband and the energy would be reduced by approximately the ratio of the interferometer linewidth to the pulse bandwidth. This section discusses the design and operation of the filter.

The design criteria were:

(1). The linewidth of the filter was chosen to be about 20 MHz because the filtering process would reduce the energy per pulse to 0.1 of its original value, while conversion to U.V. light could be maintained by focussing in the doubling crystal. How much further this process could be carried out was not known without experimental results.

(2). The intensity on the mirrors should not be above the coating damage threshold and the amplifier beam quality should not limit the filter resolution. Both these requirements meant that a confocal interferometer (see Appendix B) should be used. Since the transverse modes resonant frequencies are degenerate and the acceptance aperture is large ($r_{max} \sim$ 3 mm) for a confocal interferometer, no modematching optics should be required and large beam diameters could be maintained on the mirrors. The only alignment required is to ensure that the optic axis of the interferometer is parallel and coincident with the laser beam.

(3). The transmission frequency should be related to the c.w. dye laser frequency. This was achieved by mounting one mirror of the interferometer onto a piezo-electric crystal and locking the interferometer resonant frequency to the dye laser frequency.

Each of these criteria will be discussed in more detail as the filter design is described.

5.3.1. Mechanical construction of the filter.

The mirror separation of the filter was chosen to be 25 cm which gives a non modematched free spectral range of

300 MHz and a modematched free spectral range of 600 MHz. When the interferometer is modematched the free spectral range is much greater than the linewidth of the incoming pulses (200 MHz) so only one order of the filter will be excited. Apart from this, a design for interferometers of this type already existed. Also a reliable source of mirrors with the required curvature and coatings was available (Technical Optics). The filter body was made out of a stainless steel tube which has a smaller coefficient of thermal expansion than dural. The mirror holders were constructed of brass. The piezo-electric crystal (PZT-5H, 1" diameter, I.D.=0.75") was glued onto a brass holder which was threaded to give a coarse length adjustment. Two wires were soldered to the inside and outside of the PZT tube and were taken to a BNC connector to be used to apply the high voltage required to modulate the cavity length and apply the correction voltage. The other mirror was mounted on a mirror mount which gave the slight angle adjustments which aligned the mirrors on a common optical axis.

The filter tube was held by two mounts which were independently adjustable both vertically and horizontally. The mounts held the filter tube as close as possible to the mirror positions so that each adjustment was independent. Modematching was achieved by aligning the interferometer parallel to an optic axis defined by the incoming laser beam. The initial stage was to pass the light through the interferometer until two distinct spots were observed. The spots were overlapped close to the output of the interferometer by adjusting the horizontal and vertical controls at the output end. Next the spots were observed on a wall a few meters away and overlapped using the horizontal and vertical controls at the input end. This process was repeated until a two beam interference pattern was seen. The dye laser was then scanned over a few free spectral ranges and the interferometer transmission was observed on an oscilloscope. Fine adjustments to the horizontal and vertical controls enabled modematching to be realised which was shown on the oscilloscope by a decrease in amplitude of alternate transmission fringes, indicating that the free spectral range had doubled.

5.3.2. Optical parameters of the filter.

The bandwidth of a modematched confocal interferometer with mirror reflectivity R is (Appendix B)

$$\Delta\nu = \frac{\nu_{FSR}}{F} = \frac{c}{2L}\,\frac{1-R}{\pi\sqrt{R}}$$

If R=0.9 and L=25 cm, the bandwidth is 20 MHz corresponding to a theoretical finesse of 29. The finesse was measured and found to be approximately 25. The discrepency is probably due to the figure of the mirrors. The first mirrors tried were specially coated standard 300 MHz interferometer mirrors (SA 300 Technical Optics). These mirrors performed well if only a limited region of the mirror surface was used, which corresponds to the acceptance aperture being limited by the mirror quality rather than by spherical aberration. The mirrors were replaced with another set which were of higher optical quality ($\lambda/25$) allowing a larger input spot size and giving results closer to the theoretical values. The output beam quality also improved and became substantially more like the input beam. The original mirror set gave a very distorted fringe pattern. It is interesting to note that the analysis of Appendix B indicates that if the interferometer length is tuned away from the confocal condition then the acceptance aperture is controlled by the detuning rather than the spherical aberrations and other defects of the mirrors. This is indeed what was observed. The detuned non confocal interferometer gave a good circular fringe pattern even with the low quality mirrors. As the length was adjusted towards the confocal condition the fringes distorted progressively. The distortion was only noticeable in the lower quality mirror set.

Another prediction of the analysis of Appendix B that was verified was the resolution of higher order transverse modes as the interferometer length was tuned away from the confocal condition. When a large diameter beam was passed through the detuned interferometer so many transverse modes were excited that the resulting transmission fringes when viewed on an oscilloscope were asymmetric in a sufficiently detuned interferometer. If the interferometer was too long (short) then the tail was on the high (low) frequency side as shown in fig.B.2. This was one of the techniques used to identify the confocal condition. The other method was to observe whether the fringes pattern got smaller or larger when the laser frequency was increased [14]. This method did not work with the low quality mirrors in the immediate vicinity of the confocal position because the distorted fringe pattern made it difficult to tell if the fringe radii were increasing or decreasing.

5.3.3. Filter stabilisation.

The filter was stabilised using standard first derivative locking techniques [15]. Refer to fig. 5.3 to follow the description of this method. The cavity length and hence resonant frequency is scanned over a small frequency range which modulates the transmission of a fixed frequency laser beam. Depending on whether the fixed laser frequency is higher or lower than the resonant frequency, the intensity modulation will be in phase or 180° out of phase with the modulation. Also when the fixed laser frequency is equal to the average resonant frequency the intensity modulation is at twice the modulation frequency. The intensity modulation is amplified and phase sensitively detected. The phase sensitive detector is driven by the modulation frequency and its output is a D.C. level whose polarity depends on the relative phase and and whose magnitude depends on both the relative phase and the gradient of the transmission versus frequency curve shown in fig. 5.3. Essentially the output is the first derivative of the transmission profile. The sign of the P.S.D. output contains the required information about the position of the fixed frequency laser relative to the transmission maxima of the cavity.

Figure 5.3.

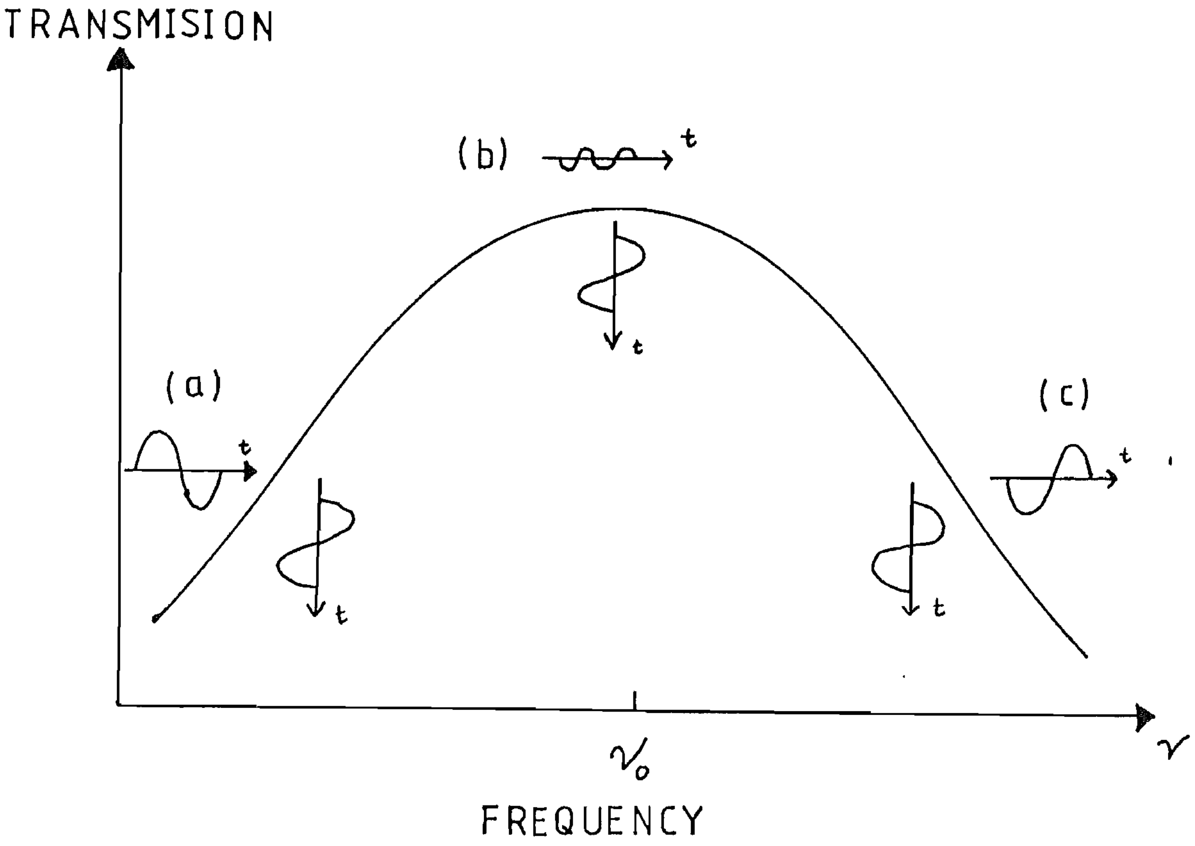

Figure 5.3. First derivative locking.

The graph shows on an expanded frequency scale one of the transmission maxima of an interferometer. The transmission as a function of time is shown at three points on the curve as the resonant frequency is varied.

(a) on the low frequency side of ν_0 the transmission change is in phase with the frequency change.

(b) at the peak the change in transmission occurs at twice the rate of the change in frequency.

(c) on the high frequency side the change in transmission is 180° out of phase with (a).

If the P.S.D. output is amplified to a sufficient level and applied with the correct sign to the PZT crystal then the cavity resonant frequency may be tuned into resonance with the fixed laser frequency. This simple scheme has the defect that the P.S.D. output, the error signal, vanishes when the cavity and laser frequencies are equal. As the signal applied to the PZT is proportional to the error signal final cavity frequency will come to equilibrium somewhere between the original cavity frequency and the laser frequency. To avoid this problem the P.S.D. output is integrated before being amplified and applied to the PZT. Thus when the laser and cavity frequencies are equal, the error signal becomes zero and the integrator output remains constant. A schematic diagram of the locking system is shown in fig. 5.4.

The circuits used in this experiment were taken from [16]. The modulation frequency was 600 Hz and the cavity resonant frequency was modulated over 7 MHz. Due to the lack of sensitivity of the P.S.D. circuit a commercial P.S.D. unit (Bentham) was substituted. This has continually variable gain and a wide range of time constants. The intensity modulation was detected on a photocell. The amplified pulses were also incident on the detector since they were coincident with the residual c.w. beam. To prevent the very large signal saturating the amplifier and affecting the locking, the detector was shorted out during the pulses. The circuit used for this is shown in fig.5.5.

Figure 5.4.

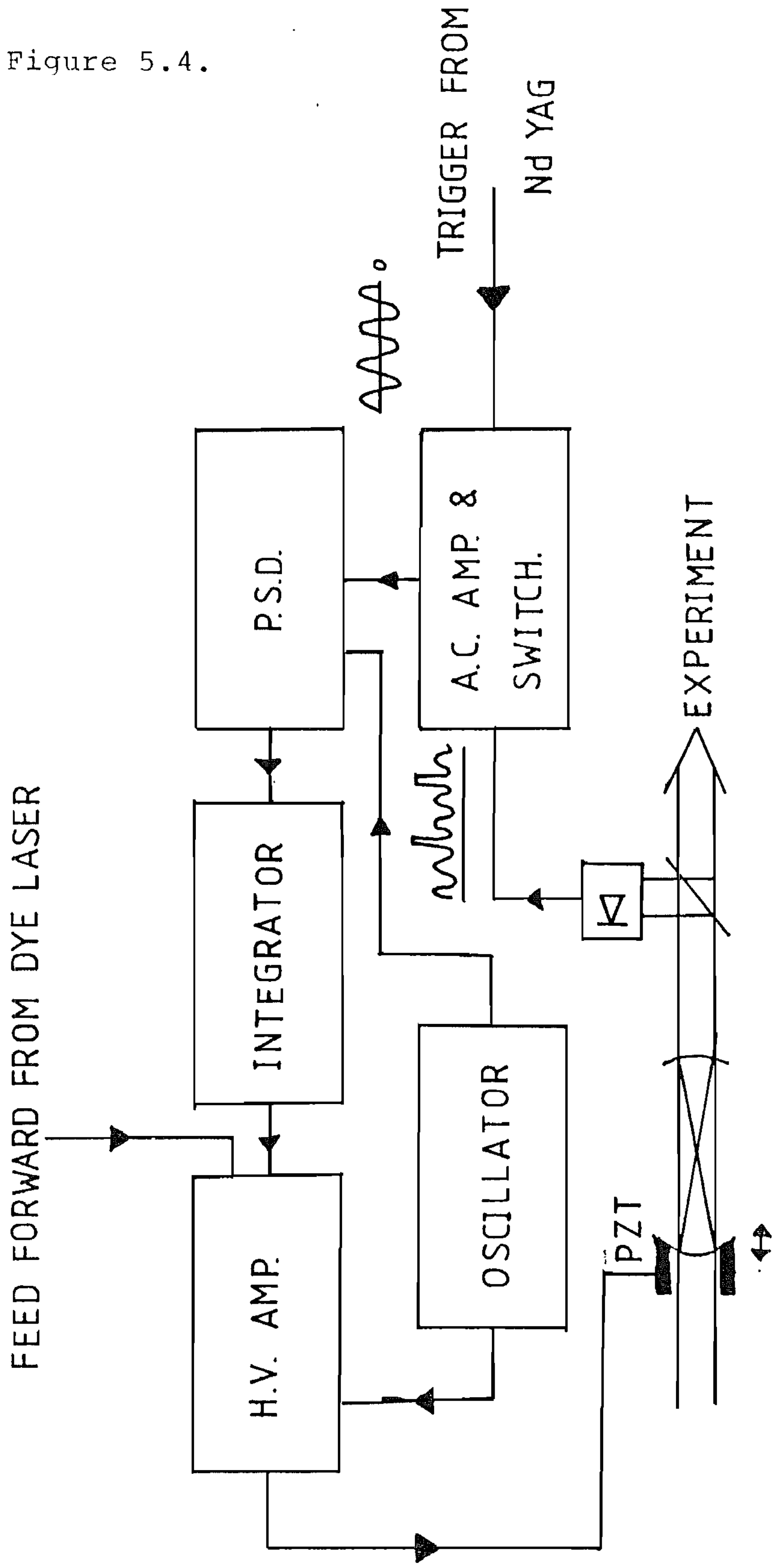

Figure 5.4.

Schematic of the locking electronics.

The signal from the photocell was passed through a current to voltage converter.An analogue switch shorted the output to earth wherever a trigger pulse was present from the Nd:YAG laser. The analogue switch was triggered by two 74LS123 which controlled the delay with respect to a trigger pulse from the Nd:YAG laser and the duration that the analogue switch conducted. The next stage was an active low pass filter which rolled off at 18 dB per octave and had a corner frequency at 1000 Hz. This surpressed any transients due to the switching while passing the modulation frequency. Two stages of adjustable gain follow the filter. The output of the amplifier was passed to the phase sensitive detector where it was rectified and sent to the integrator [16]. After integration the signal was passed to the high voltage amplifier where it was summed with the modulation voltage and the feed forward from the dye laser. As explained in Section 5.1 the feed forward was used to adjust the filter resonance frequency when the dye laser was scanned. The locking electronics deal with any non linearities in the scan and any perturbations the filter might receive. The maximum frequency scan of this system was 2 GHz. This was limited by the high voltage (900 V) that could be applied to the PZT. Since this was sufficient to carry out the experiment no steps were taken to expand the scan range.

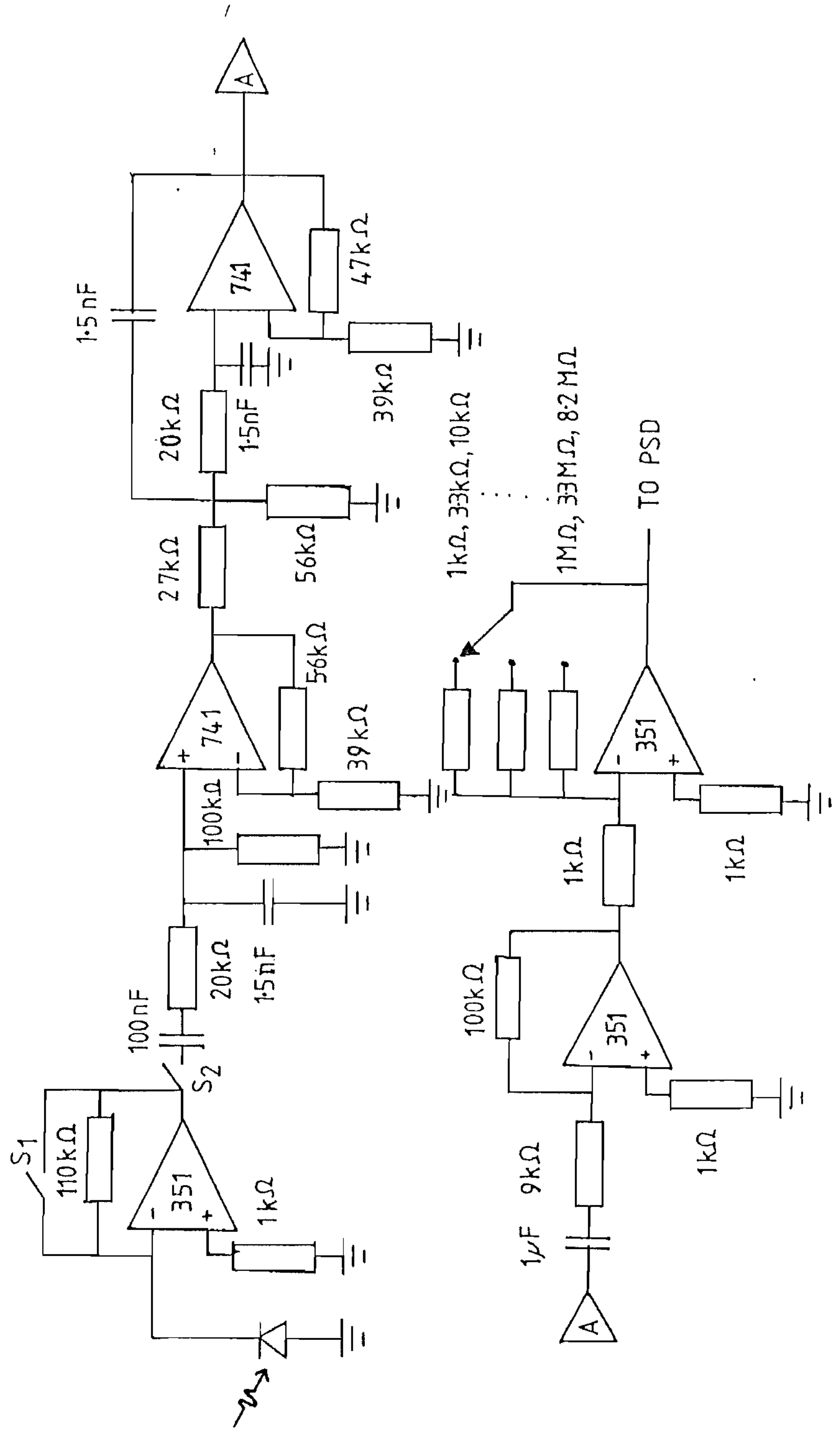

Figure 5.5(a).

Filter stabilisation detector's filtering and amplification circuit.

Figure 5.5(b).

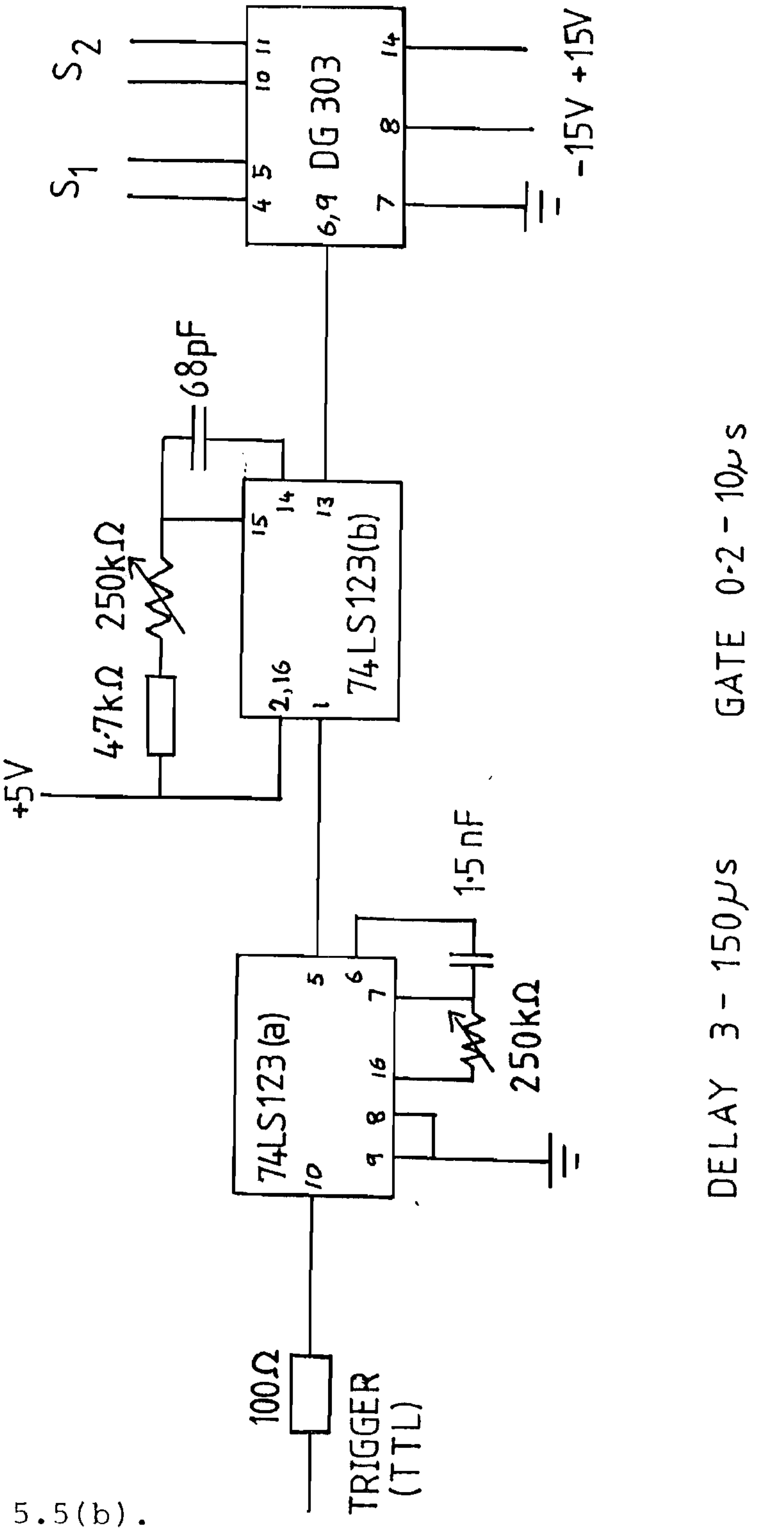

Figure 5.5(b).

Analogue switch driving circuit.

The quality of lock was monitored by measuring the ratio of the error signal when locked to the maximum error signal when unlocked. Typically this value lay between 1/200 and 1/1000 of the filter linewidth. The lock was optimised by increasing the gain and time constant on the P.S.D.. The laser could be scanned over 2 GHz in 0.25 s without losing lock. Normally the filter lost lock only when the dye laser suffered an abrupt frequency perturbation.

When in use both the c.w. light and the pulsed light were modematched into the cavity. Since modematching was insensitive to deviations less than $\pm 5\times10^{-4}$ radians from coincidence of the filter axis with the laser beam optic axis this means that the pulsed and c.w. light were colinear to this level. One mechanism which could make the pulsed light non parallel with the c.w. light was the thermal lenses set up by the pump laser. Since the dye was flowing in the dye cells the thermal lenses would be washed out by the time the next pulse arrived. However the c.w. beam was present all the time and sampled the production and decay of the lens. This could cause beam deviations not seen by the pulsed light. It is conceivable that such non parallelism could cause a frequency offset between the c.w. light and the pulsed light. The magnitude of such an offset may be estimated from [14] and is negligible in comparison with a frequency shift caused by the amplifier chirp described in Section 5.2.

The linewidth of the filter was 25 MHz measured with a single frequency laser. The linewidth of the pulsed light was measured to be 30-40 MHz with some of the broadening attributed to the 7 MHz length modulation applied to the filter.

When the filtered pulsed light frequency was compared with the c.w. frequency it was found to be slightly blue shifted. One contribution to this residual amplifier shift was due to the non zero gradient of the pulsed spectrum at the c.w. frequency. This may be estimated as follows. Let the filter lineshape be represented by a Gaussian $f(\nu)$

$$f(\nu) = F e^{-\nu^2/\sigma_1^2}$$

while the pulsed lineshape is represented by

$$g(\nu) = G e^{-(\nu-\nu_s)^2/\sigma_2^2}$$

Then the transmitted lineshape is given by $f(\nu)g(\nu)$ with a maximum found by equating the first differential with respect to ν to zero:

$$\nu_{max} = \nu_s \frac{\sigma_1^2}{\sigma_2^2 + \sigma_1^2}$$

ν_s is the amplifier shift (40 MHz), σ_1 is the 1/e half width of the filter ($\sigma_1 \sim 15$ MHz) and σ_2 is the 1/e half width of the pulsed spectrum ($\sigma_2 \sim 75$ MHz).

The resultant contribution to the residual amplifier shift is +1.5 MHz towards the peak of the pulsed spectrum (see fig. 5.6.). This value is smaller than that observed using a high resolution confocal interferometer with a 300 MHz free spectral range and a 2 MHz linewidth. For the sequence of spectra used in the final data analysis the residual amplifier shift was 12.3 ± 5.2 MHz. Other contributions to the residual amplifier shift could include a locking error in the filter stabilisation electronics or the effect of spherical aberrations of the mirrors. As pointed out in Appendix B, the round trip phase change is smaller off axis than on axis, so the resonance frequency is higher. The maximum useable radius r_{max} is calculated assuming that it is the radius when the off axis resonance frequency can be resolved from the on axis frequency. This corresponds to a change of +25 MHz and could explain the magnitude of the residual amplifier shift.

Figure 5.6.

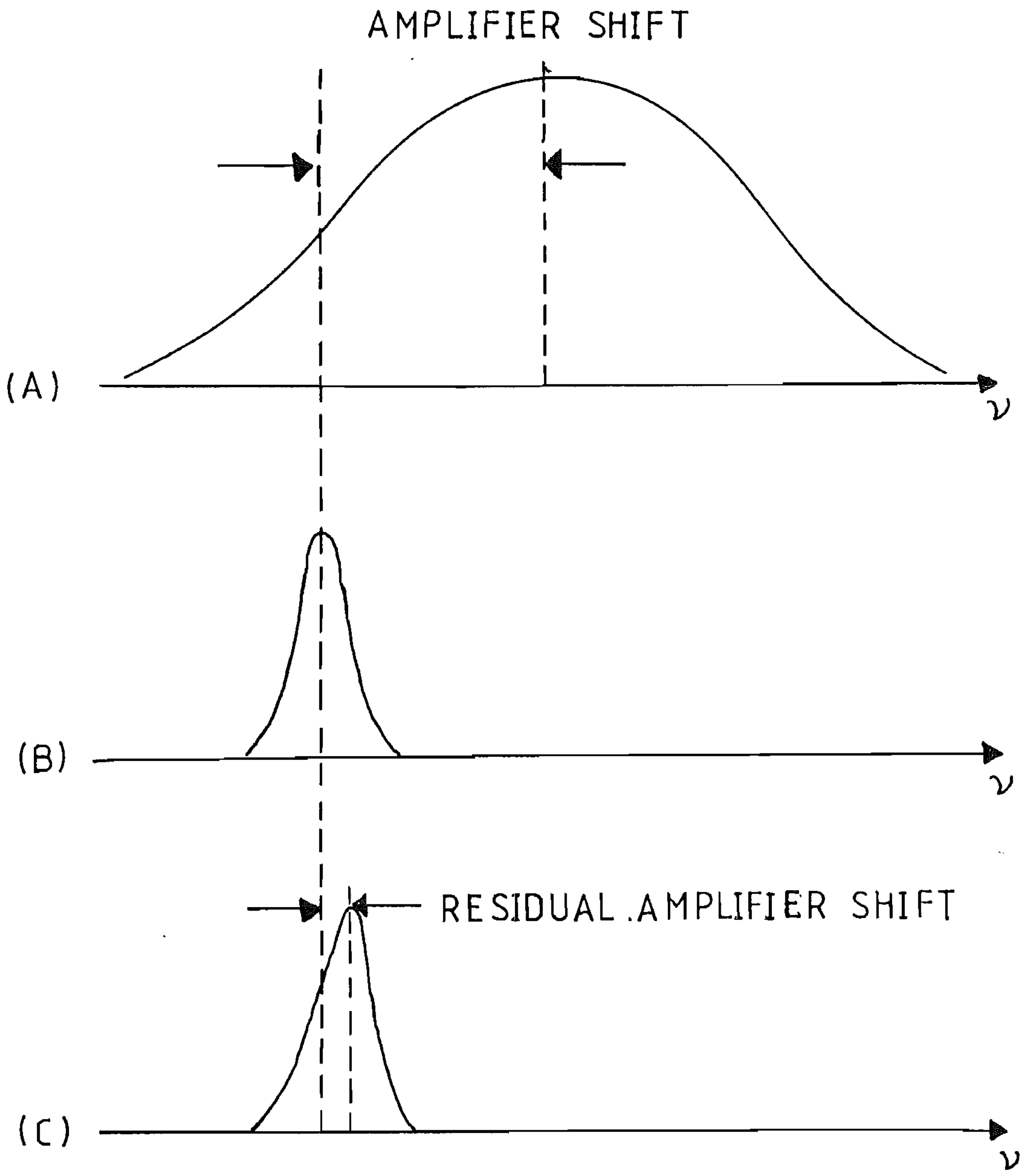

Figure 5.6.

Spectral properties of the filtered pulsed light showing the formation of the residual amplifier shift.

(a) spectrum of the c.w. and pulsed light.

(b) transmission of the filter locked to the c.w. light.

(c) the residual amplifier shift.

Consideration of the Fourier transform relation between time and frequency shows that for the filter limited linewidth of 25 MHz the length of a single sided exponential pulse must be

$$\Delta t = \frac{1}{2\pi \Delta \nu} \sim 7\,\text{ns}$$

and for a Gaussian pulse

$$\Delta t = \frac{0{\cdot}441}{\Delta \nu} \sim 17\,\text{ns} \; (\text{FWHM})$$

The $1/e$ time is related to Δt by $\Delta t(\frac{1}{e}) = \frac{\Delta t}{\ln 2} = 25\,\text{ns}$. Since the output pulse was a combination of a Gaussian rising edge and an exponential tail the expected duration was between 7 ns and 25 ns as indeed it was. Fig. 5.7 shows tracings of a series of photographs of the temporal shape of the filtered pulse. The first photograph shows the modematched case with a duration of 12 ns ($\frac{1}{e}$ time). The second photograph shows the output pulse of the filter when it has been deliberately detuned from the mode matched case. The ripple in the intensity is a real effect, the exposure was 20 s which corresponds to an average of 200 pulses. The period of the ripple is ~ 3 ns and relates to a beat frequency of ~300 MHz. The explanation is that when non modematched, the free spectral range reduces to

Figure 5.7.

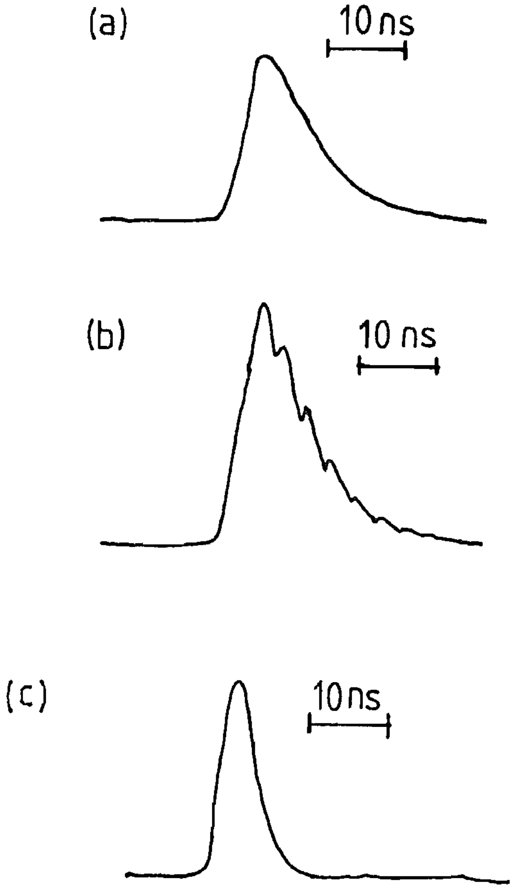

Figure 5.7.

Temporal profile of the amplified and filtered pulses.

(a) interferometer mode matched.

(b) interferometer deliberately detuned from the modematched condition.

(c) the amplified pulse before filtering.

300 MHz and since the pulse bandwidth is 150-200 MHz a significant amount of power may be present in the adjacent orders of the interferometer. These cause the 300 MHz beats. The final photograph shows the input pulse to the interferometer with the full width at half maximum of 4 ns.

The transmission of the interferometer was 1/13. An incident peak power of 260 kW was reduced to 10 kW after taking into account the different pulse lengths.

5.4. Frequency doubling.

Frequency doubling was carried out in either lithium formate monohydrate (LFM) or urea. Both crystals had similar dimensions ($8\times8\times8$ mm^3) and were cut for type I phase matching at 486 nm at normal incidence. The crystals were obtained from Quantum Technology. The crystal cells had normal incidence windows and contained a solution of FC104 which acted as a nominal index matching liquid and prevented the crystals from coming into contact with water vapour. Details of the phase matching requirements and calculations of the nonlinear coefficients are given in Appendix C where it is also shown that urea is expected to be about four times more efficient than LFM under optimum focussing conditions. The relative conversion from 486 nm to 243 nm was measured and urea was found to be six times more efficient than LFM which is in reasonable agreement with theory. Any differences may be accounted for by the optical quality of the LFM crystal which had deteriorated due to colour centre formation by U.V. absorbtion. The high efficiency of the urea crystal meant that it was used exclusively in the final stages of the experiment. As an example of this, energy conversion efficiencies of up to 20% were observed when doubling a 1 mJ unfiltered pulse from the output of the amplifier giving up to 200 μJ of U.V.. The best observed from LFM was 50 μJ. Under optimum focussing conditions (spot size = 18.6 μm) the generated second harmonic power is (see Appendix C, Table C.1)

$$P_{2\omega} = 8.9 \times 10^{-5} \; P_{\omega}^{2}$$

for a crystal of length 0.01 m. After filtering of the pulsed light there is approximately 10 kW of peak power in the pulse indicating that up to $P_{2\omega} \sim 8.5$ kw may be generated. Clearly at this level of conversion the assumption that the fundamental is not being depleted is invalid. Experimentally the $1/e$ radius in the crystal was 70 μm ± 20 μm indicating that the arrangement was far from optimum. The generated U.V. energies ranged from 10-20 μJ (1.7 kw-3.3 kw using a 6 ns pulse length) after correction for losses in optics, which is a conversion of 33%. Using the experimental value of $\xi = 0.1$, $h_{mm}(B) = 0.03$ and for $P_{\omega} = 10$ kW, $P_{2\omega} = 3.2$ kW in close agreement with the measured value.

Typical energy levels in the experimental cell were

0.7-3 μJ. Using a U.V.pulse length of 6 ns these correspond to peak powers of 117-500 W.

5.5. Production of atomic hydrogen.

The atomic hydrogen source was initially designed by J.M. Girkin. This section briefly describes the design and operation of the system. The molecular hydrogen (or deuterium) was obtained by electrolysis of H_2O (or D_2O). The electrolysis cell consisted of a stainless steel cathode and a tungsten anode. The electrolyte was a mild NaOH solution. A reservoir of capacity 500 ml was included to provide a reliable supply. Flow from the electrolysis cell was controlled by a needle valve.

The molecular gas was dissociated using a microwave discharge (Microtron 200). Total power available was 25 W but normally 6-10 W was sufficient to provide a good discharge. Increasing the microwave power did not normally increase the atomic hydrogen yield as observed in the sample cell. The discharge cell was quartz with dimensions 9 cm × 1 cm diameter. It was connected via an orifice of I.D. 1 mm and a graded seal to a pyrex U. tube which lead to the sample cell. The dimensions are given in fig.5.8. Atomic hydrogen tends to recombine on almost any material.

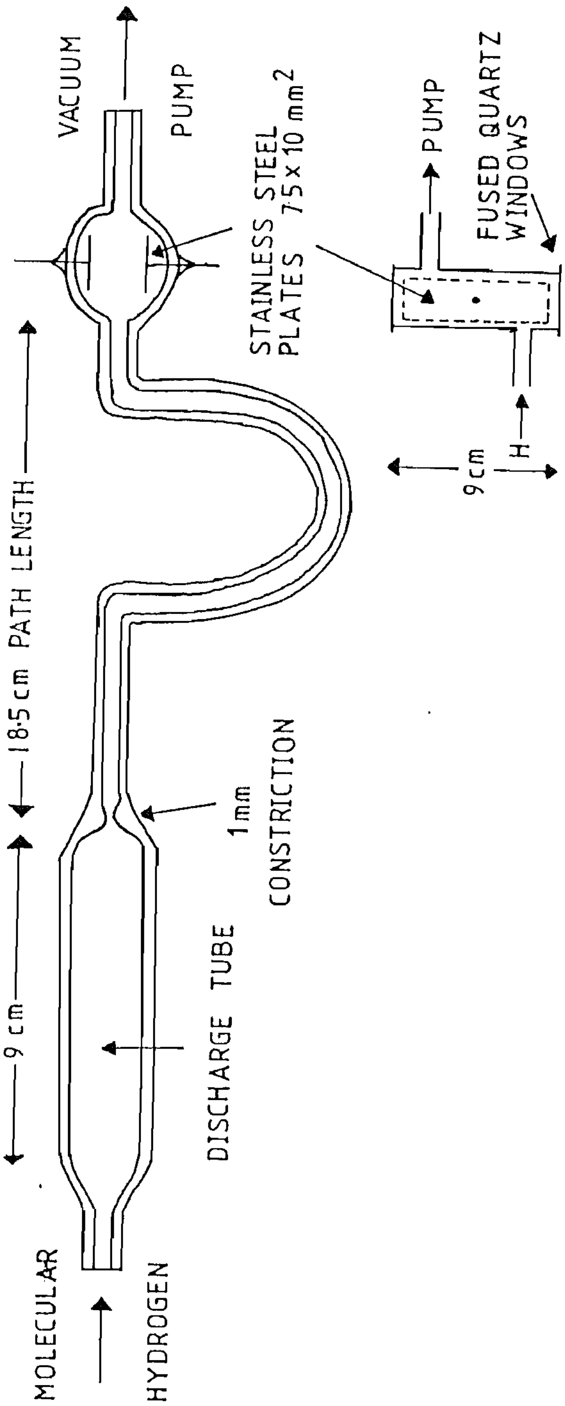

Figure 5.8.

The hydrogen discharge tube and ionisation cell.

Teflon and quartz are good low recombination materials. By coating the inside of the tube with a thin layer of dilute ortho-phosphoric acid (10-20%) the recombination rate is enormously reduced. With practise, observation of the discharge colour and spectrum enabled the presence of atomic hydrogen to be predicted. A deep pink colour and the absence of molecular bands was a good sign. Drying out of the phosphoric acid coating by evaporation caused by the discharge or the low pressure (0.2 torr) was noted by a reduction in signal or a change in colour of the discharge to a whiter shade of pink. Adding a little water to the discharge tube generally cured this problem. When deuterium was under examination it was found beneficial to use deuterated water as the dilutant of the phosphoric acid. If this was not done the hydrogen 1S-2S signal was found to be larger than the deuterium 1S-2S signal even though D_2 was being flowed into the discharge. Replacing the water coating with D_2O increased the deuterium 1S-2S signal until it was comparable with the hydrogen signal. The reason for this is twofold. Firstly the deuterium source produces a significant quantity of H_2 since NaOH was added to the electrolyte. Secondly, there may be a mechanism for the exchange of D_2 vapour with the H_2 combined on the walls of the discharge tube as water. This process may reduce the amount of D_2 and increase the amount of H_2 in the cell when the walls were coated with H_2O.

Pressure in the discharge cell was monitored using a capacitative manometer (Baratron 222B). Normally the experiment was carried out using a pressure of 0.18 torr, but when pressure shifts were examined a range of 0.5 to 1.5 torr was used.

5.6. The detection scheme.

The ions produced by three photon ionisation of atomic hydrogen were detected by applying a small voltage between two stainless steel plates in the sample cell. The plate dimensions were 10×75 mm^2 and they were separated by 15 mm. The collected charge changed the potential of the capacitor plates which was detected using the circiuts of fig. 5.9. The sample cell and the first amplifier were placed in a Faraday cage to prevent pickup in the electrically noisy environment of the laboratory. The biggest problem was R.F. pickup associated with the Nd:YAG laser and 50 Hz noise related to the microwave discharge. The circuit of fig. 5.9 includes a high pass filter which reduces the amplitude of 50 Hz pickup. The combined system has a response of 13Vpc which was measured by applying a voltage step V_{in} to one end of a known capacitor C_o connected in place of the sample cell. If V_{out} is the output pulse height the sensitivity S is given by

Figure 5.9.

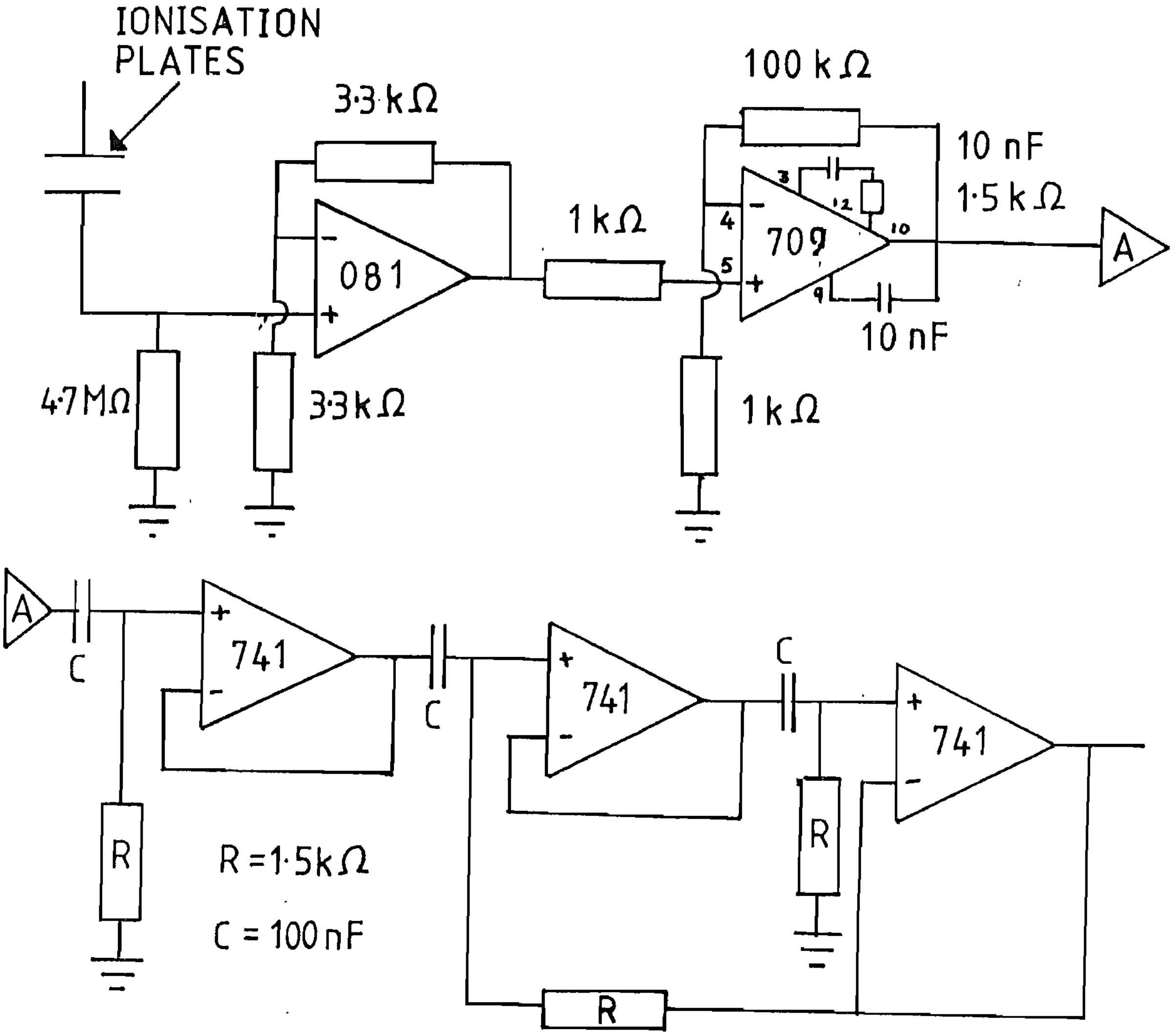

Figure 5.9.

The ionisation detector circuit.

$$S = \frac{V_{out}}{C_o V_{in}}$$

The noise level corresponds to 10^4 electrons peak to peak or 3×10^3 rms.

5.7. The reference interferometer.

The reference interferometer was a confocal interferometer with a nominal free spectral range of 500 MHz. The spacer was a quartz tube the ends of which were made parallel by polishing on a lathe. The tube length was measured independently by Dr. A.I. Ferguson and myself; the measurements agreed within experimental error. The result was 149.57 ± 0.02 mm. The mirrors were coated with aluminium and epoxied to the end of the quartz tube with torr seal applied to the outside of the joints only. Taking into account the diameter of the tube 23.76 ± 0.1 mm, and the radius of curvature of the mirrors, 15 cm, the optical length of the interferometer was 150.51 ± 0.013 mm corresponding to a free spectral range of 497.96 (10) MHz. The refractive index correction to this was made negligible by evacuating the tube to 10^{-6} torr and testing for pressure integrity. After this the tube was sealed.

Ambient temperature variations can cause the resonant frequency to shift. Quartz has a small temperature coefficient (0.5×10^{-6} °C^{-1}), however, in order to keep the resonant frequency constant to better the 1 MHz the ambient temperature should be stabilised to better than 4×10^{-3} °C. While this level of accuracy was not achieved in this experiment a temperature drift of less than 20 MHz per hour was normally found. The correction to the free spectral range ν_{FSR} due to this shift is easily found to be:

$$\Delta\nu_{FSR} = \frac{\dot{\nu}_L \; \nu_{FSR}}{\dot{\nu}_L - \dot{\nu}_I}$$

where $\dot{\nu}_L$ and $\dot{\nu}_I$ are the laser and interferometer frequency changes per unit time respectively. In this experiment the laser scan was normally 2 GHz in 200 s, ie. $\dot{\nu}_L = 10$ MHz/sec and $\dot{\nu}_I \sim 6\times10^{-3}$ MHz/sec, and the correction was less than 0.3 MHz per free spectral range. This number is roughly the order of magnitude of the uncertainty in the free spectral range and since no systematic shift of this size could possibly be resolved in this experiment this correction was neglected. It could, however, be included as an additional uncertainty.

The temperature of the interferometer was stabilised using a proportional controller designed to control a peltier cooler. A nicrome heating wire of resistance 10 Ω was wrapped around the tube, fig. 5.10. Thermal insulation was given by foam rubber inside an airtight tube. This system was somewhat sensitive to the ambient temperature changes and draughts in the laboratory so it was placed within a temperature controlled box which was stabilised to ±0.5 °C using a commercial control unit. A 100 W bulb provided the heat source.

5.8. Data acquisition.

Up to six channels of information were recorded using a homemade data acquisition system. A small microcomputer (BBC model B Acorn computer) controlled the system and analysed the data. Data was digitised using an analogue to digit converter (ADC) which sequentially accessed up to eight channels. Normally six channels were used:

Number (1). Pulsed 1S-2S data.
(2). Not used in this experiment
(3). Not used in this experiment
(4). 500 MHz interferometer fringes
(5). Smoothed 1S-2S data (0.1 s time constant).
(6). Tellurium saturation spectrometer (0.1 s time constant).
(7). Amplifier shift c.w. data
(8). Amplifier shift pulsed data.

Figure 5.10.

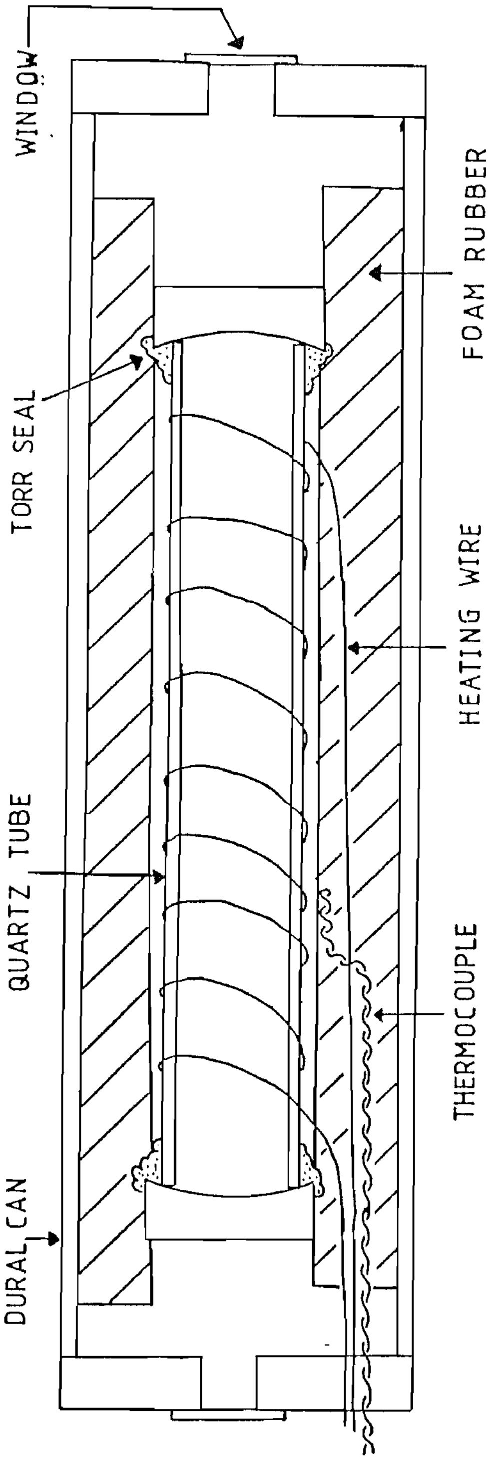

Figure 5.10.

The reference interferometer.

As will be explained in the next chapter, the amplifier shift data was taken separately from the experimental data. A schematic of this experiment is shown in fig.5.11. Prior to being digitised the data was collected using sample and hold techniques. The output of the sample and holds was scaled and shifted to utilise the resolution of the ADC.

Timing of the data acquisition process was achieved by using trigger pulses from the Nd:YAG laser to start each device. The sample and hold was triggered from a pulse approximately 210 μsec before the optical pulse. Adjustable delays and gate widths enabled the correct data to be collected. The ADC was triggered by the computer which continually interrogated a memory mapped logic input connected to the Nd:YAG Q switch. This ensured the ADC cycled after the data had been collected. Since the internal memory of the BBC computer was limited, the data was stored in a sideways RAM (Solidisk 128 k bytes). This was configured to appear as an additional disc drive with 100 k bytes of extra memory. After each run the data was displayed and stored on floppy disc.

Figure 5.11.

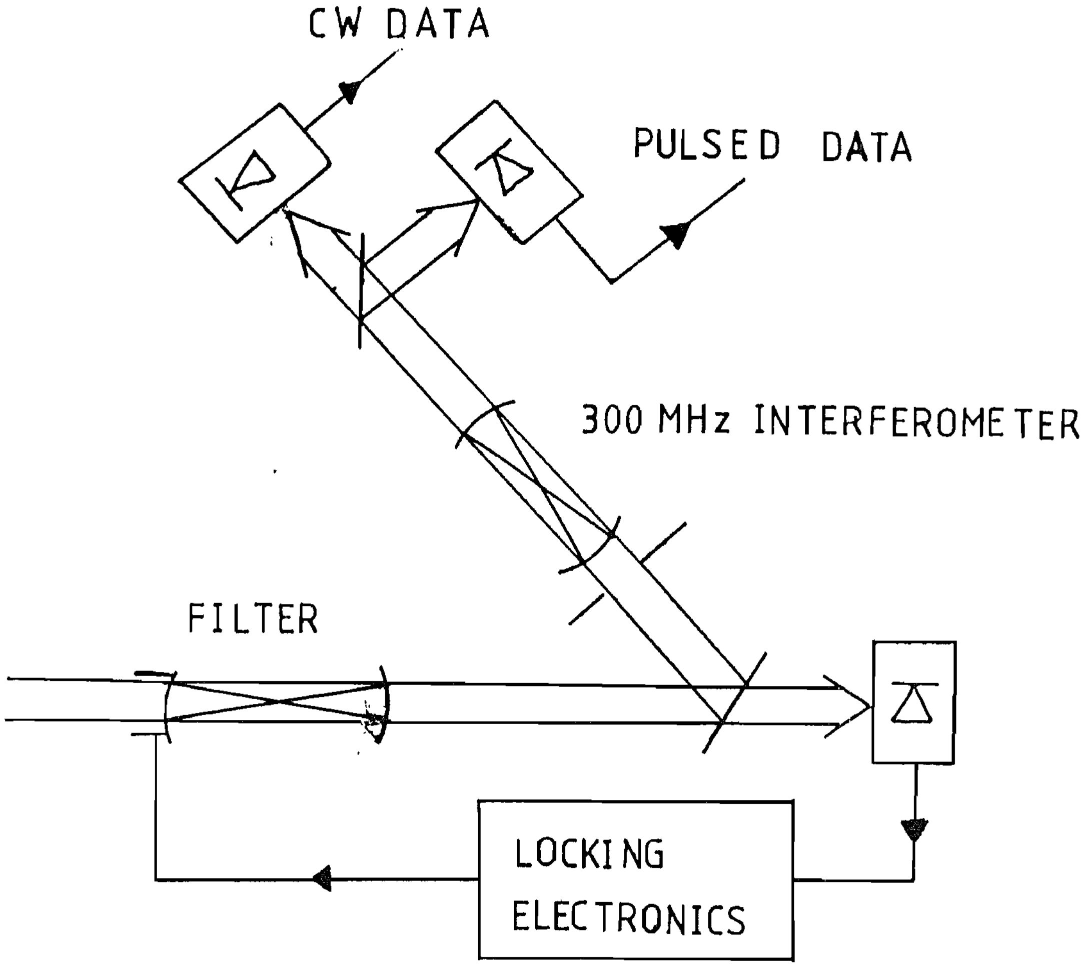

Figure 5.11.

Experimental arrangement used to obtain the residual amplifier shift.

5.9. Experimental procedure.

This section discusses and summarises the experimental set up which has been described area by area in the preceding sections. The analysis of the results is given in Chapter 6.

The 243 nm light from the frequency doubling crystal was focussed into the sample cell using a quartz lens of 10 cm focal length and a cylindrical quartz lens of 15 cm focal length. The cylindrical lens was used to compensate for the astigmatic beam caused by walkoff in the doubling crystal. The beam was focussed onto a plain high reflecting mirror placed 1-2 cm beyond the sample cell. The U.V. spot size was 100 μm ± 30 μm. Typical energies were in the region .7 μJ-3 μJ per pulse in 6 ns.

The residual amplifier shift described in Section 5.3.3 was measured before or after each sequence of 1S-2S spectra and used to correct those spectra before the other corrections were included. It would have been preferable to record the shift for each individual spectrum but this proved difficult since the extra losses introduced by the doubling crystal and other optics made it impossible to do both at once. Improvements in the sensitivity of the filter locking detector would overcome this.

The tellurium spectra were recorded using essentially the experimental arrangement described in Chapter 4 and in [17]. The phase sensitive detector had a time constant of

0.1 s. Since the filter locking electronics had a limited scan range of 2 GHz, the c.w. laser was scanned over a range which did not contain the calibrated component. To overcome this problem the separation between the hydrogen 1S-2S spectra and the intermediate $^{130}Te_2$ line was measured. This line is indicated in fig. 6.1 by an arrow. The separation between the calibrated line and this intermediate line was measured in a separate experiment.

The frequency marker fringes were detected on a photocell and amplified using a standard current to voltage converter. The signal was sent to the ADC with no signal averaging.

References.

[1] R. Wallenstein, T.W. Hänsch. Appl. Optics. 13 1625. (1973).

[2] C. Kittel. "Introduction to Solid State Physics". 5th. ed. Wiley. (1976).

[3] S.A. Lee. PhD. Thesis. M.L. Report No. 2460. Stanford Univ. (1975).

[4] P. Kumar, R. Bondurant. Appl. Optics. 22 1284. (1984).

[5] M.H. Gassman, H. Weber. Opto-electronics. 3 1877. (1971).

[6] U. Ganiel, A. Hardy, G. Neuman, D. Treeves. IEEE. J. Quant. Elect. QE-11. 881. (1975).

[7] R. Wallenstein, T.W. Hänsch. Opt. Comm. 14 353. (1975)

[8] R. Wallenstein, H. Zacharias. Opt. Comm. 32 429. (1980).

[9] C. Wieman, T.W. Hänsch. Phys. Rev. A. 22 192. (1980).

[10] G.L. Eesley, M.D. Leverson, D.E. Nitz, A.V. Smith. IEEE. J. Quant. Elect. QE-16 113. (1980).

[11] S. Chu, A.P. Mills, J.L. Hall. Phys. Rev. Lett. 52 1689. (1984).

[12] A. Yariv. "Introduction to Quantum Electronics". 2nd. ed. Wiley. (1976).

[13] C.G.B. Garrett, D.E. McCumber. Phys. Rev. A. 1 305. (1970).

[14] M. Hercher. Appl. Optics. 7 951. (1968).

Chapter 5.

[15] A.J. Wallard. J. Phys. E. 6 793. (1973).

[16] K.C. Shotton, W.R.C, Rowley. "An Electronic Servocontrol System for Stabilised Lasers and Similar Applications". N.P.L. Report QU 28. (1978).

[17] J.R.M. Barr, J.M. Girkin, A.I. Ferguson, G.P. Barwood, P. Gill, W.R.C. Rowley, R.C. Thomson. Opt. Comm. 54 217. (1985).

Chapter 6. Results and Conclusions

The first part of this chapter discusses the methods used to analyse the experimental data. The conditions under which the data was recorded are described in Chapters 4 and 5. A general description of the techniques used to analyse the data is given in Section 6.1. Each stage of the data reduction is discussed in turn: calibration of the relative frequency scale in Section 6.2, measurement of the intermediate frequency standard in Section 6.3, and the measurement of the 1S-2S frequency in Section 6.4. The results of the experiment and comparison with theory and previous experiments are given in Section 6.5. Finally an overall view of this experiment, together with suggestions for improvements and new experiments, is given in Section 6.6.

6.1. Data analysis.

The data was collected on a pulse to pulse basis as described in Section 5.8. The data was treated in two ways. Firstly, in order to provide print outs of the spectra, as in fig. 6.1, the data was smoothed using a moving average defined by:

$$\overline{X}_m = \frac{1}{2N+1} \sum_{m=-N}^{+N} X_{n+m}$$

where X_j is the data corresponding to the j^{th} pulse in a particular spectrum. $\overline{X}_n$ is the smoothed value of X_n carried out using the adjacent 2N points. The smoothed value is only defined over the points m=N to m=M-N-1 where M is the total number of points, typically $M \sim 2000$. Other types of smoothing were investigated [1,2] and gave similar results but at a cost of increased computer time. Figure 6.1 was produced using this method of smoothing. N was taken as 15 for the interferometer fringes and 5 for the $^{130}Te_2$ spectrum and 1S-2S spectrum.

It is tempting to numerically differentiate the smoothed data in order to find the peaks of each spectrum. This is equivalent to evaluating $\delta_n = \overline{X}_{n+1} - \overline{X}_n$ and finding $\delta_n = 0$. However in full this is

$$\delta_n = \frac{1}{2N+1} \sum_{m=-N}^{+N} \left(X_{n+m+1} - X_{n+m} \right) = \frac{1}{2N+1} \left(X_{n+N+1} - X_{n-N} \right)$$

and only two points contribute to each δ_n . In practise the following definition was used [3] :

$$\delta_n^* = \sum_{m=1}^{N} \left(x_{n+m} - x_{n-m} \right)$$

and the zero crossings which correspond to a maximum were found. A linear interpolation was carried out to find the position of the zero if it occurred between two δ_n^*. Geometrically this method is equivalent to finding the centre of gravity of the peak providing there are less than 2N+1 points in the width of the peak.

Figure 6.1.

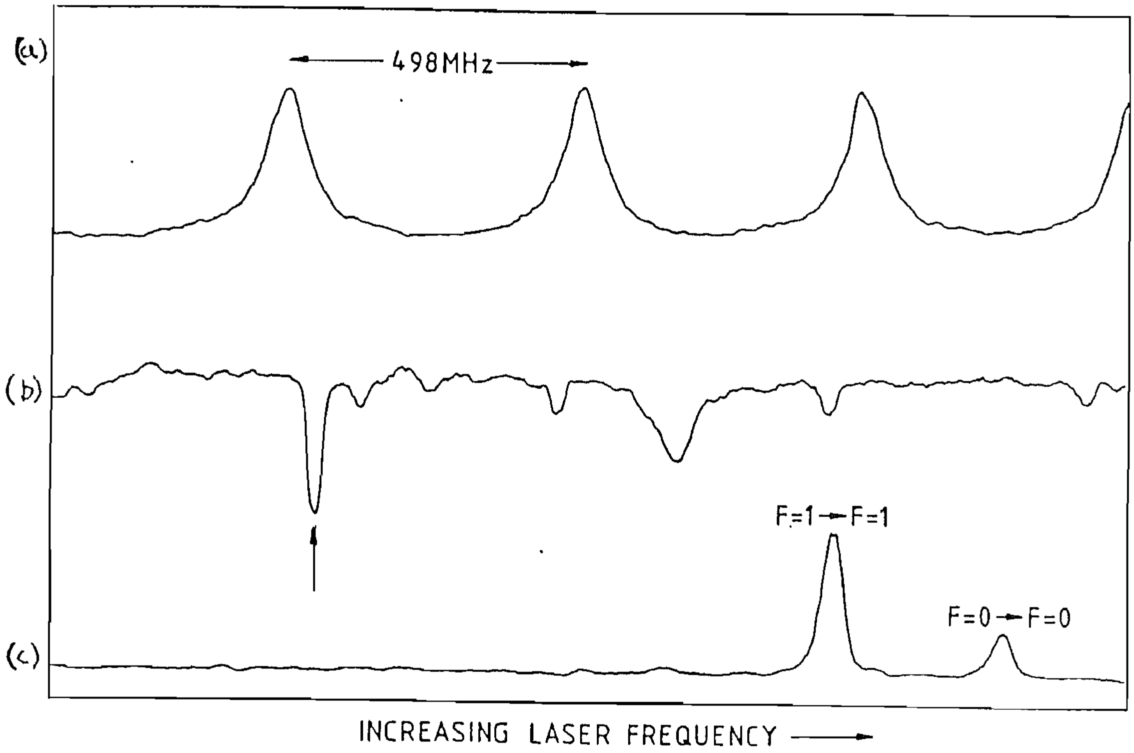

Figure 6.1.

Typical experimental spectra of :

(a) reference interferometer

(b) $^{130}Te_2$ Doppler free spectrum

(C) two photon resonantly enhanced three photon ionisation spectra.

The function δ_n^* is composed of two parts. For a given point j the area under the points $j+1$ to $j+N$ is

$$A_j = a \sum_{i=1}^{N} x_{j+i}$$

where a is the frequency change between the points and is assumed constant. The area under the points $j-N-1$ to $j-1$ is also calculated:

$$A_{-j} = a \sum_{i=1}^{N} x_{j-i}$$

and the difference taken, $\delta_j^* \propto A_j - A_{-j}$. When $\delta_j^*=0$ the point corrosponds to the centre of gravity of the curve provided N is sufficiently large compared with the number of points in the curve. In mathematical terms if $\Delta\nu_p$ is the full width at half maximum of the peak then

$$N \geqslant \frac{\Delta\nu_p}{2a}$$

The algorithm is useful since it can give both the first derivative of the peak ($N< \frac{\Delta\nu_p}{2a}$) and the centre of gravity ($N>\frac{\Delta\nu_p}{2a}$). Any differences correspond either to an asymmetric profile or poor signal to noise.

This method is probably the best that can be used without making any assumptions about the shape of the peaks. Alternatively if the shape of the $^{130}Te_2$ curves are assumed to be Lorentzian, then this curve could be fitted to the data using a nonlinear least squares method. This is attractive for the next stage of experiments but was not done here since the resolution is not severely limited by the techniques used in data analysis. This point will be returned to in the discussion of the experiment in Section 6.5.

A different technique for analysing the data which looks promising is the maximum entropy method [4]. This technique is designed to give a consistent analysis of data while making the minimum possible assumptions about the structure within the data. It is also possible to incorporate any additional information about the structure. Examples of the use of this method given in [4] include the analysis of blurred and noisy photographs, X-ray tomography, NMR spectroscopy and an interesting "blind" deconvolution of an unknown image blurred with an unknown point spread function. Maximum entropy could prove useful in analysis of the type of spectral data accumulated in laser spectroscopic measurements. It was not used in this experiment mainly due to time constraints and limited computing power.

6.2. Relative frequency calibration.

The information contained in the reference interferometer channel was analysed to provide a frequency scale in terms of pulse number. The centre of gravity of each fringe was located using the method of Section 6.1.

For this case the value of N=15 was chosen. Changing N had little effect on the centre of gravity because the fringes were very symmetrical. In any case since each fringe in a given spectrum had the same shape, the separation between two calculated centres of gravity would be the free spectral range of the interferometer for any value of N.

The pulse number of three or four maxima in the vicinity of the $^{130}Te_2$ line and the H 1S-2S transition were recorded and plotted on a graph as a function of relative interferometer order number. It was found that a linear fit to the graph of order number versus pulse number was not always a particularly good fit and often a quadratic fit or occasionally a cubic fit was better. The origin of this effect was the non linear scan of the dye laser referred to in Section 5.1. In the absence of any further information it was difficult to decide which fit is the appropriate one to use. It should be emphasised that the differences between each fit were very small, typically in the region of 0.6% of the free spectral range of the interferometer (497.96 (10) MHz), which was less than the standard error in the final result. However, it was possible to use the measured separation of the two hyperfine components in the H 1S-2S transition as a guide in selecting the best fit.

This number may be deduced from the ground state hyperfine splitting (see Section 2.3, [5]) and is 310.713 7583 MHz in the frequency frame of the blue laser. The real energy splitting is four times this value. The measured hyperfine splitting using the linear, quadratic and cubic fits was compared with this value and the fit giving the closest agreement was used to measure the H 1S-2S to $^{130}Te_2$ line separation. For the 30 runs used to obtain the final result, 18 gave the best hyperfine splitting using a quadratic fit. The measured value of the hyperfine splitting was 310.0 (6.2) MHz which is in excellent agreement with the previous quoted experimental value. The error is one standard deviation.

Once the frequency calibration was known for each run the separation of any lines in the $^{130}Te_2$ and H 1S-2S spectra can be found. Assume for the sake of simplicity that the maxima of the reference fringes occur at the 100, 500, 900 and 1300 pulse. Assign relative order numbers 0, 1, 2, 3 respectively. In this case the graph of relative order number versus pulse number is clearly linear. Let a $^{130}Te_2$ peak occur at pulse 300 and a H 1S-2S maxima occur at pulse 1000. The fractional order number corresponding to each peak is 0.5 and 2.25 respectively, and the difference is 1.75 free spectral ranges. This simple example gives the essence of the method used in determining the hydrogen-tellurium line separation. If the fit is non linear the procedure is more complex requiring the use of interpolating polynomials [6].

6.3. Intermediate frequency standard.

The separation between the calibrated $^{130}Te_2$ component and the H (F=0 → F=0) component was approximately 1.8 GHz while the scan range of the laser was 1.9-2.0 GHz (Section 5.3.3), due to limitations of the confocal filter locking electronics. It was found extremely difficult to reliably scan the laser over the range containing both peaks. The solution was to measure the separation between component d_2 and the H (F=1 → F=1) component. In this case it was simple to ensure that both H components appeared on each spectra.

Component d_2 was used as an intermediate frequency standard and the separation between the calibrated component b_2 and component d_2 was measured in a separate experiment. Conditions were as described in Chapter 4. A total of eleven spectra were taken to obtain the b_2-d_2 separation which was found to be 549.1 (1.7) MHz with d_2 being higher in frequency than b_2. The transfer standard is indicated in fig. 6.1 by an arrow.

To carry out the above analysis the centre of gravity of each curve was found using the procedure outlined in Section 6.1. The number of points used was 2N=10. Varying the number of points did not change the observed positions significantly; the shift was always less than the scatter in the points.

6.4. Measurement of H (F=1→F=1), $^{130}Te_2$ separation.

A total of thirty spectra were analysed to measure the $^{130}Te_2$ intermediate frequency standard (component d_2) to H (F=1→F=1) hyperfine component separation. The data collection was carried out in four groups and the residual amplifier shift was measured for each group as discussed in Section 5.3.3. The experimental layout used in measuring the residual amplifier shift is shown in fig. 5.11. The net amplifier shift weighted for the number of runs in each group was 12.3(5.2) MHz while the weighted separation between the intermediate frequency standard and the H (F=1→F=1) component was 895.1(2.8) MHz. The latter result together with the previous measured separation between the two $^{130}Te_2$ lines (b_2, d_2) indicates that the accuracy of the interpolation routine is better than ± 3 MHz (1 standard deviation). Thus the main contribution to the overall error as discussed in Section 6.5 arises from the amplifier shift measurements. In analysing the H 1S-2S spectra the number of points used in finding the centre of gravity of the lines was 2N=10. Varying the number of points did make a small difference in the apparant position of the centre of gravity indicating an asymmetry in the shape of the spectrum. The magnitude of the shift was less than the statistical uncertainty (2.8 MHz) and was neglected.

There is a further problem in relating the peak frequency of the pulsed laser spectrum to the centre of the 1S-2S two photon transition. This is discussed in detail by Wieman and Hänsch [7] and arises because in measuring the pulsed spectrum using an interferometer phase information is lost. This makes it difficult to relate the pulsed laser spectrum to the two photon signal. If no phase information is available then the relationship is clearly arbitrary. The approach taken in [7] was to attempt to calculate the expected two photon signal spectrum using the measured pulsed laser spectrum and making a number of assumptions about the phase. The relative peak positions of the two spectra was then found to depend upon the choice of phase variation and physical arguements used to select the most likely variations. The differences between the possible choices was the dominant error in that experiment.

In this experiment it was assumed that filtering the amplified pulses using the confocal interferometer produced transform limited pulses with electric field amplitudes represented by single sided exponentials. The result is that the phase is a constant across the spectrum and the peak of the pulsed spectrum coincides with the peak of the H 1S-2S signal. In this case the only amplifier shift correction that had to be included was the residual amplifier shift described in Section 5.3.3. While this assumption is probably not completely valid the following points support it. The linewidth of the confocal filter was measured to be ~ 25 MHz and was broadened to ~30 MHz when the length modulation was applied. The linewidth of the filtered pulsed spectrum was 35-45 MHz which is less than one and a half times the Fourier transform limit. The linewidth of the H 1S-2S signal was also in the region of 35 MHz to 45 MHz which is the result expected for a transform limited pulse. Also it was qualitatively noted that if the filtered pulsed spectrum was asymmetric due to the confocal filter length being detuned, the H 1S-2S signals similarly showed a corresponding asymmetry. If this assumption is not correct, an estimate of the magnitude of the shift may be obtained from [7] where the correction was taken to be 7% of the pulsed linewidth giving, in the case of this experiment, a 2.8 MHz shift which acts in a direction to make the 1S-2S frequency larger. This is considerably smaller than the total error in this experiment and is the same size as the statistical error.

6.5. The 1S-2S transition frequency.

The $1S_{1/2}$-$2S_{1/2}$ transition frequency of atomic hydrogen can be calculated using the results of Section 6.4 together with various corrections. All corrections are applied in the frequency frame of the blue laser. The origin of the main corrections due to the acousto-optic shift of the light used in the $^{130}Te_2$ spectrometer (Section 4.2) and the residual amplifier shift (Section 5.3.3) are shown in fig.

6.2. The measured separation was reduced by 80 MHz and increased by 12.3(5.2) MHz. One experimental systematic correction was applied: in Section 3.7 measurement of a pressure shift was discussed. The $1S_{1/2}-2S_{1/2}$ frequency increases by +3(6)MHz/torr so at operating pressure of 0.2 torr the correction was -0.6(1.2) MHz. The A.C. Stark shift was calculated in Section 3.5 to be 0.7 Hz $W^{-1}cm^{2}$ and using the laser intensity of 117-500 W and a 100 μm spot size, the shift was 0.3-1.1 MHz. This shift was not experimentally confirmed since the magnitude was very small in comparison with the resolution. Additionally, such an experiment would require careful experimental control and measurement of the spot size and laser pulse energy. Since the A.C. Stark shift is expected to increase the measured 1S-2S frequency the correction was -0.6(0.6). An additional uncertainty of (0.3) MHz was included to account for the error in the interferometer free spectral range.

The result of the above calculation is shown in Table 6.1 where the value of one quarter of the H (F=1 → F=1) hyperfine component frequency is found by adding the corrected $^{130}Te_2$-H (F=1 → F=1) separation to the known value of the $^{130}Te_2$ frequency giving

616 515 271.6 (6.3) MHz

The value of the centroid of the H 1S-2S transition frequency is found by adding 77.678 MHz to the one quarter of the H (F=1 → F=1) frequency and multiplying by 4. The factor 77.678 MHz is given by 1/4 × the hyperfine splitting of the 1S-2S transition. The value of the 1S-2S frequency is

2 466 061 397 (25) MHz.

Figure 6.3 shows a histogram of the experimental results indicating that the distribution is approximately Gaussian. The small deviations are probably not significant due to the small number of samples (30).

6.6. Experimental results and deductions.

The aim of this experiment was to measure the frequency of the $1S_{\frac{1}{2}}$-$2S_{\frac{1}{2}}$ transition in atomic hydrogen. This has been successfully done. The main reason for carrying out this measurement, as discussed in the introduction, is to make a comparison of experiment with theory. To do this the difference between the Lamb shift of the $1S_{1/2}$ and $2S_{1/2}$ levels is extracted from the measured frequency of the $1S_{1/2}$-$2S_{1/2}$ level by subtracting it from the Dirac value (including the recoil correction) given in Section 2.2. The result is

7137 (25) MHz

which compares well with the theoretical value of 7128.171(81) MHz which may be calculated from Table 2.2. By accepting the theoretical value for the 2S Lamb shift, a value for the ground state Lamb shift is obtained:

8182 (25) MHz

Figure 6.2.

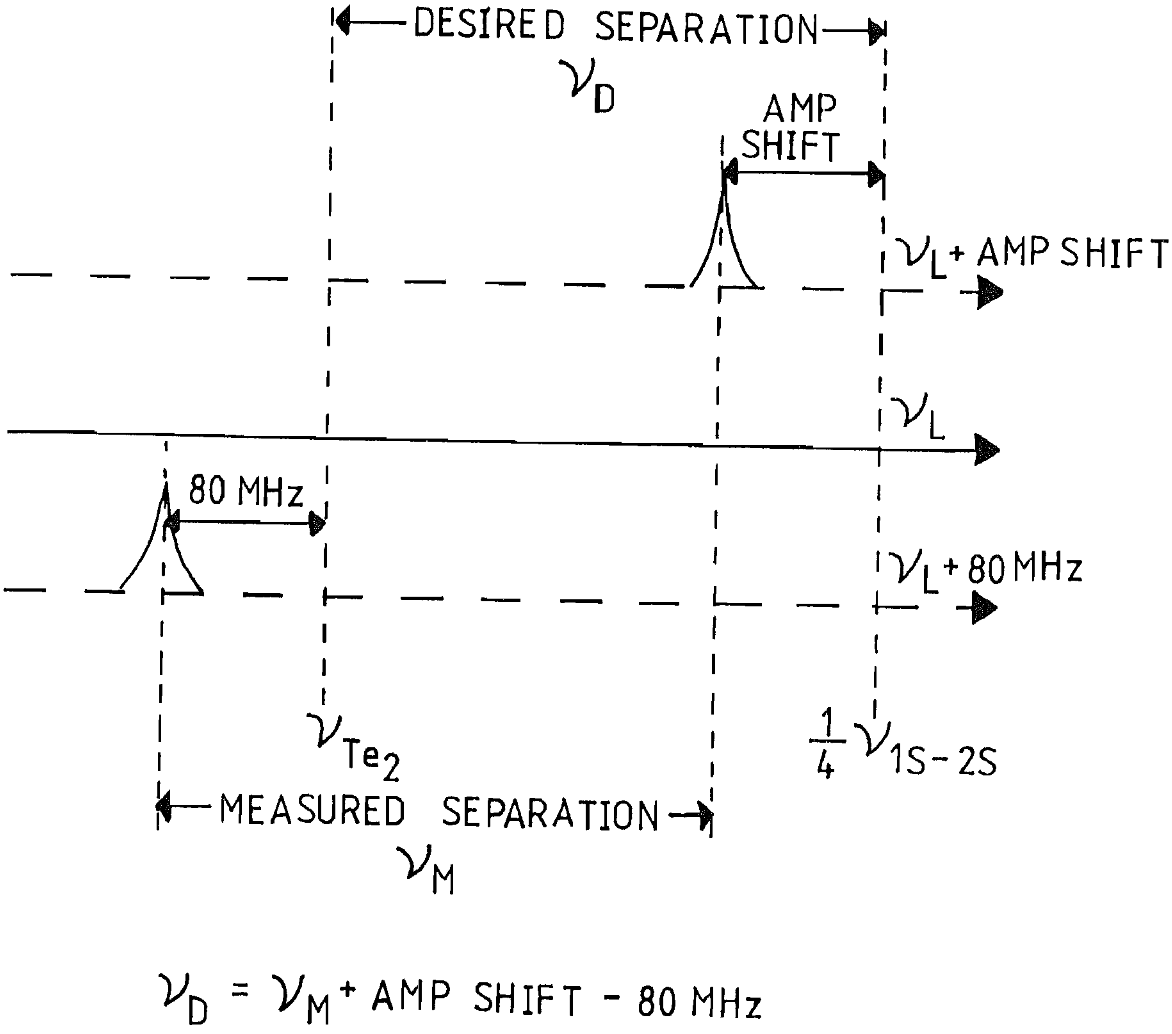

Figure 6.2.

The major corrections to the separation between the $^{130}Te_2$ line and the H 1S-2S signal are the acousto-optic shift of +80 MHz which made the $^{130}Te_2$ frequency appear lower than it really was and the residual amplifier shift which had the same effect on the H 1S-2S frequency.

Table 6.1.

Calibrated $^{130}Te_2$ frequency [15]	616 513 896.30 (25) MHz
Intermediate $^{130}Te_2$ offset	+549.1 (1.7) MHz
$^{130}Te_2$ - H(F=1→F=1)	+907.4(5.9) MHz
H(F=1→F=1), centroid	+77.678 MHz
Acoousto-optic shift	-80.00 MHz
Pressure shift	-0.6(1.2) MHz
A.C. Stark shift	-0.6(0.6) MHz
Interferometer free spectral range	(0.3) MHz
Total	616 515 349.3 (6.3) MHz

Measured $1S_{1/2}$-$2S_{1/2}$ frequency	2 466 061 397 (25) MHz
Deduced Lamb shift difference	7137 (25) MHz
Deduced $1S_{1/2}$ Lamb shift	8182 (25) MHz
Deduced Rydberg constant	10 973 731.50 (11) m^{-1}
$1S_{1/2}$-$2S_{1/2}$ hyperfine splitting	1240 (25) MHZ.

Figure 6.3.

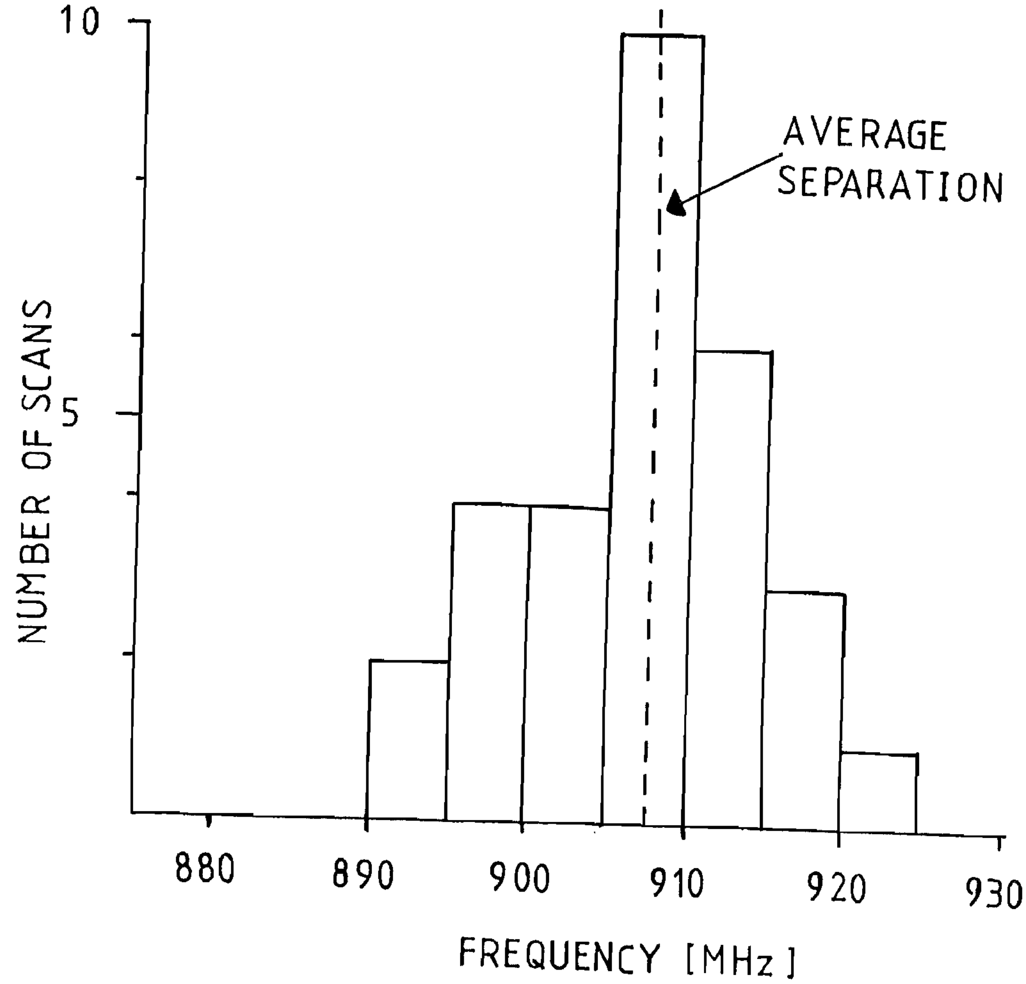

Figure 6.3.

Distribution of the experimental results. The frequency scale is the measured separation between the d_2 tellurium line and the H (F=1→F=1) resonance including the amplifier shift. No other systematic corrections have been included.

The theoretical result (Table 2.2) is 8173.24(8) MHz. The difference between theory and experiment is 9(25) MHz. Given that the quoted error is 1 standard deviation, the agreement is excellent.

There are three previous measurements of the ground state Lamb shift of hydrogen with which this work may be compared, [7,8,9]. The measured values are given in Table A.1 (note the results quoted there include the recoil correction as part of the Lamb shift). Only the value of [7], which gives the ground state Lamb shift to be 8175(30) MHz (excluding the recoil correction) [10] is comparable in accuracy with the results of this experiment. While this value is in better numerical agreement with theory, the error bounds ensure that disagreement is insignificant. All previous experiments [7,8,9] use the comparison method briefly outlined in the introduction to deduce a value for the ground state Lamb shift. This involves measuring the separation between a Balmer β line which was, in the case of reference [7], the cross-over between the $2S_{1/2}-4P_{1/2}$ and $2S_{1/2}-4S_{1/2}$ (Stark allowed) transitions as observed using polarisation spectroscopy, and one quarter of the $1S_{1/2}-2S_{1/2}$ transition frequency. In order to obtain the ground state Lamb shift the measured separation was compared with the theoretical separation calculated assuming that the ground state Lamb shift was zero. The difference between these two numbers is one quarter of the ground state Lamb shift. These experiments give essentially an indirect measurement of the ground state Lamb shift and do not allow direct comparison with independent experiments which measure other properties of the H atom. Additionally there were large corrections to the measured separation which arose from observing the Balmer β spectra in a Woods discharge using polarisation spectroscopy. In order of importance [7] these corrections were pressure, D.C. Stark shifts, unresolved hyperfine structure and A.C. Stark shifts.

In comparison, the experiment described here was somewhat simpler. The $^{130}Te_2$ frequency standard, with the exception of temperature induced pressure shifts, was stable and insensitive to perturbations [15]. Using this cell far from the recommended conditions resulted in shifts of less than 1 MHz. However, as with reference [7], similar problems were found with the 1S-2S systematic shifts (amplifier chirp, A.C. Stark shift). In this experiment pressure shifts were included as a correction whereas [7] excludes them as being too small. The main experimental conclusion of this work was a value of the $1S_{1/2}$-$2S_{1/2}$ transition frequency [14]. From this a value for the ground state Lamb shift has been deduced. In addition this result may be compared directly with experiments which have made measurements of the Rydberg constant, [10,11,12,13]. This comparison is interesting because most of these measurements have been made on one of the Hα($n=2 \rightarrow n=3$) transitions. The ideas used were basically the same as those of this experiment, the wavelength of the transition was measured [11,12,13] and the value of the Rydberg constant varied until the theoretical value for the transition wavelength was in agreement with the experimental value. For this experiment the new value for the Rydberg constant was given by

$$R_{new} = R_{old} - \frac{\Delta}{\nu_T} R_{old} = \frac{\nu_E}{\nu_T} R_{old}$$

where R_{old} is the weighted mean of the recent values of the Rydberg constant [11,12,13,16] shown in Table 6.2. ν_T is the value of the 1S-2S frequency calculated using R_{old}, ν_E is the experimental value of the 1S-2S frequency and $\Delta = \nu_T - \nu_E$. The value of the Rydberg constant deduced here is

$$109\ 737\ 31.50\ (11)\ \mathrm{m}^{-1}$$

A comparison of this value [14] with all previous measurements of the Rydberg constant made on Hα [11,12,13] and on the 1S-2S transition [10] is shown graphically in fig.6.4. This information is also given in tabular form by Table 6.2.

The comparison shows that there is a disagreement between Amin's value [13] and those of Hildum et al. [10] and Goldsmith et al. [11]. The Rydberg constant derived from this work is in agreement with the other values but with a slightly larger uncertainty [14].

Table 6.2.

		ΔR	ΔE
Hildum et al.	[10]	0.492(22)	395.6(4.8)
Goldsmith et al.	[11]	0.500(32)	397.8(7.2)
Petley et al.	[12]	0.521(64)	402.6(14.4)
Amin et al.	[13]	0.539(12)	406.6(2.7)
Weighted mean	[11-13]	0.534(13)	405.5(2.9)
This work	[14]	0.50(11)	397(25)

A comparison of recently measured values of the Rydberg constant adjusted by Taylor [16]. Also included is a value for the Rydberg constant deduced from a recent measurement of the $1S_{1/2}$-$2S_{1/2}$ transition frequency in atomic hydrogen [10]. The tabulated quantities are: $R=R_{\infty}-10973731\ m^{-1}$ and $E=E_{1S-2S}-2466061000$ MHz.

Figure 6.4.

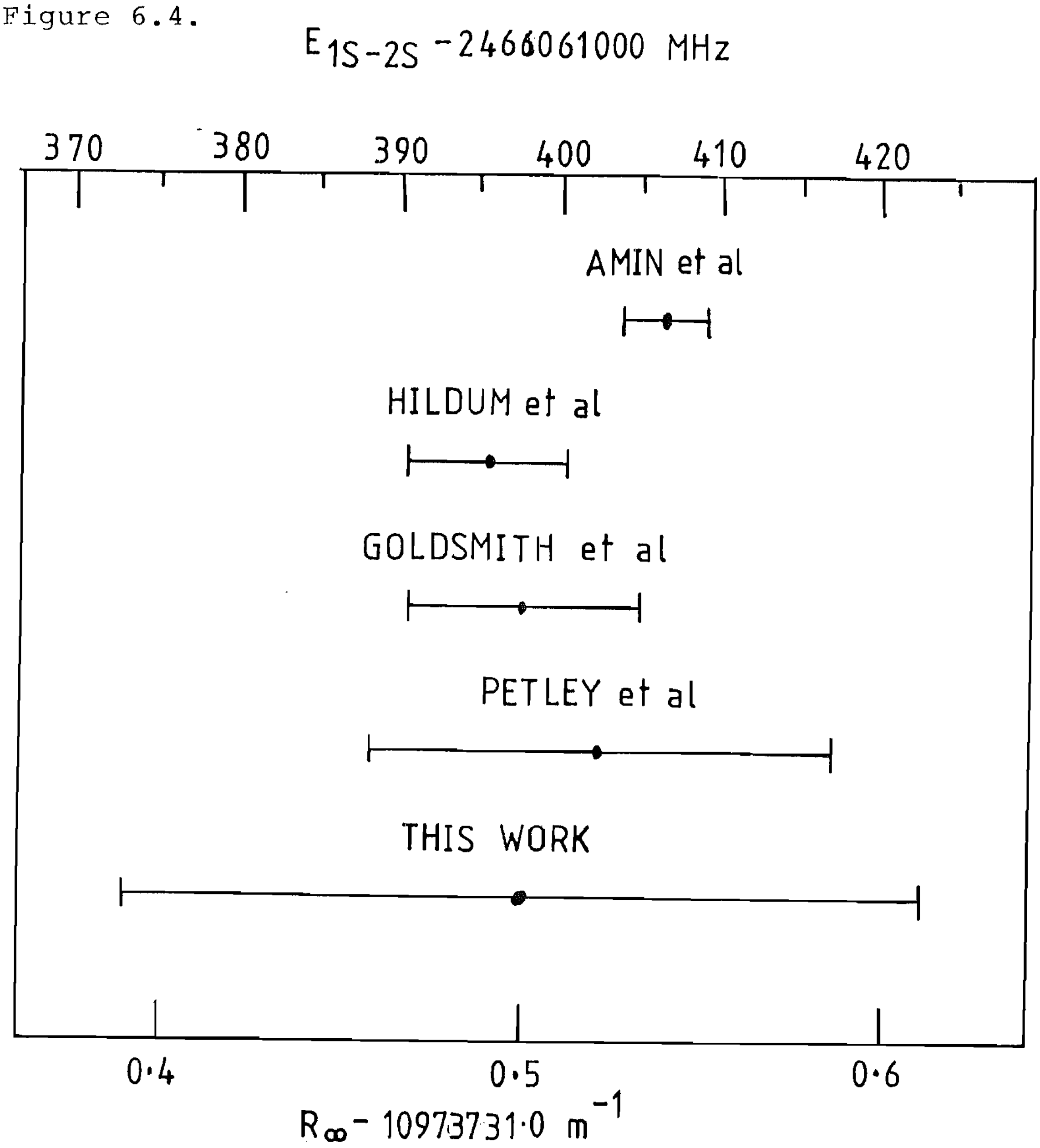

Figure 6.4.

A comparison of the recent Rydberg constant values measured on atomic hydrogen using methods of high resolution laser spectroscopy. The frequency scale corresponds to the values for the 1S-2S transition calculated using each value of the Rydberg constant.

The conclusion that may be made from these results is that to within the experimental accuracy the $1S_{1/2}-2S_{1/2}$ frequency measured here is consistent with other independent measurements made on the Hα lines in atomic hydrogen. However it does not give a great deal of confidence in the value of the ground state Lamb shift that was deduced. This occurs because the magnitude of the difference between the experimental value of the 1S-2S frequency and the predicted value for each Rydberg constant is the same as the magnitude of the difference between the theoretical value of the ground state Lamb shift and the value deduced from the experiment. Thus using the Rydberg constant of Goldsmith et al. [11] would give a value, for the ground state Lamb shift from this experiment, of

8174(26) MHz

which is in better numerical agreement with the theoretical value. Note the increase in uncertainty. However the range of values for the Lamb shift is well within the error bounds of the original result calculated using the weighted mean value of the Rydberg constant.

6.7. Conclusion.

The results discussed in Section 6.4 represent one of the first experimental measurements of the 1S-2S transition frequency in atomic hydrogen [10,15]. While the agreement, both with other experiments and with theory, was fair, improvements could be made to the experiment equipment and procedure.

The experiment procedure could be improved by using an interferometer with a smaller free spectral range as a frequency marker. Alternatively a number of interferometers with different free spectral ranges could be used. The advantage of this would be a better method of correcting non linearities in the laser frequency scan. Additionally interpolation to such a small fraction of the free spectral range (~1%) would not be required. More linear frequency scans could be realised by pressure scanning the laser stabilisation interferometer as discussed in Section 5.1 [10]. The precision of determining the centre of the various spectral lines could be better. Either a non linear least squares programs could be used to fit Lorentzian or Gaussian shapes to the lines, or perhaps methods of maximum entropy [4] could be utilised.

It is expected that the main improvement will result from a reduction in filter linewidth. This would give the advantage that the observed lines would be narrower, also the magnitude of the residual amplifier shift would be reduced. Some consideration will have to be given to the cause of the residual amplifier shift. The three possible contributions are (a) spherical aberrations of the interferometer, (b) the non zero frequency background of the pulsed spectrum and (c) frequency offsets introduced by the locking circuitry. The constraints on reducing the linewidth arise partially from the reduction in energy throughput. To some extent this can be mitigated by tighter focussing into the urea crystal and by improving the sensitivity of the ionisation detector. A further problem will arise once the filter linewidth approaches the laser linewidth (1-2 MHz). In this case locking the filter could become a problem. The lower limit on the filter linewidth is expected to be about 3 MHz. In this case the accuracy could well be about 300 kHz. At this level an improved measurement of the Rydberg constant would be possible. The ultimate aim of such a series of measurements would be to investigate the differences between the Erickson [17], Mohr [18] and Saperstein [19] theories, which amount to about 300 kHz in the ground state Lamb shift. At this level of accuracy the use of a ground state hydrogen beam to reduce pressure shifts [10,13] will be important. An alternative to an atomic hydrogen beam is to use atoms emitted from a cold source (<1 mk) and slowed down using the earth's gravitational field, [20]. Using a c.w. 243 nm source [21,22] and two photon optical Ramsey spectroscopy resolution of the natural linewidth of the 1S-2S transition may prove possible.

To carry out the measurement reported here a frequency standard near 486 nm has been developed which is known to 4 parts in 10^{+10} of its optical frequency [15]. Two lines in the tellurium spectrum close to one quarter of the 1S-2S transition frequency in atomic hydrogen and deuterium were calibrated. These are available for accurate frequency measurements both in the Balmer β spectrum and in the 1S-2S spectrum. It is anticipated that with measurements made in a metastable atomic beam a new improved value of the Rydberg constant can be measured since the linewidths of the Balmer β transitions are narrower than the corresponding Balmer α transitions [23]. Such an experiment is in progress in Southampton.

A narrow linewidth high power dye amplifier chain has been constructed which provides up to 260 kW peak power with a 180 MHz linewidth. The linewidth can be reduced to 35 MHz by filtering in a confocal interferometer. Typically 10 kW power is available. Frequency doubling with efficiencies of up to 20% have been observed for both schemes with up to 0.2 mJ available in the broadband case and 20 μJ in the narrowband case. As demonstrated in this experiment this constitutes a useful source for high resolution spectroscopy.

The system described here provides the basis for a narrow linewidth high peak power laser system which spans the near ultra violet to near infra red. By combining sum frequency generation and frequency doubling all possible frequencies between 208 nm and 900 nm could be reached. An argon ion pumped oscillator which is capable of generating 560 nm to 900 nm light also covers 280-450 nm by frequency doubling. The region 360-488 nm is covered by mixing with the residual fundamental of the Nd:YAG laser which for the Quanta-Ray DCR-2A is of the order of 200 mj per pulse. Frequency doubling of the amplified dye laser output followed by mixing reaches the region of 208-280 nm. The difficult wavelength region around 500 nm can be obtained by pumping the oscillator with the U.V. from an argon ion laser and pumping the amplifier chain with the frequency tripled Nd:YAG output. To retain the good spectral properties of the narrow linewidth output of the dye amplifier chain when frequency mixing, the Nd:YAG should be run on a single longitudinal mode. Recent developments in single mode c.w. Nd:YAG lasers pumped perhaps by a diode array have made it possible to seed a single cavity mode of a high power pulsed Nd:YAG laser with low level coherent radiation so the only one mode is preferentially present in the laser output. Providing proper frequency matching is maintained between the master and slave oscillators, single mode operation of the slave occurs [24]. It would be interesting to observe whether a dye amplifier chain pumped by a single mode pump laser exhibits improved spectral performance since mode beating would not occur [25]. Such a laser system might prove useful for a spectroscopist whose spectral range of interest is not fixed.

Chapter 6.

Reference.

[1] A. Savitzky, M. Golay. Analytical Chemistry. 36 1627. (1964).

[2] J.P. Porchet, Hs.H. Gunthard. J. Phys. E. 3 261. (1969).

[3] J.J. Snyder. Appl. Optics. 19 1223. (1980).

[4] S.F. Gull, J. Skilling. IEE Proc. 131 646. (1984).

[5] H. Hellwig, R.F.C. Vessot, M.W. Levine, P.W. Zitzewitz, D.W. Allen, D.J. Glaze. IEEE Trans. Intsrum. Meas. 19 200. (1970).

[6] G.M. Phillips, P.J. Taylor. "Theory and Application of Numerical Analysis". Academic Press. (1973).

[7] C. Wieman, T.W. Hänsch. Phys. Rev. A. 22 192. (1980).

[8] T.W. Hänsch, S.A. Lee, R. Wallenstein, C. Wieman. Phys. Rev. Lett. 34 307. (1975).

[9] S.A. Lee, R. Wallenstein, T.W. Hänsch. Phys. Rev. Lett. 35 1262. (1975).

[10] E.A. Hildum, U. Boesl, D.H. McIntyre, R.G. Beausoleil, T.W. Hänsch. Phys. Rev. Lett. 56 576. (1986).

[11] J.E.M. Goldsmith, E.W. Weber, T.W. Hänsch. Phys. Rev. Lett. 41 1525. (1978).

[12] B.W. Petley, K. Morris, R.E. Schawyer. J. Phys. B. 13 3099. (1980).

[13] S.R. Amin, C.D. Caldwell, W. Lichen. Phys. Rev. Lett. 18 1239. (1981).

[14] J.R.M. Barr, J.M. Girkin, J.M. Tolchard, A.I.

Ferguson. Phys. Rev. Lett. 56 580. (1986).

[15] J.R.M. Barr, J.M. Girkin, A.I. Ferguson, G.P. Barwood, P. Gill, W.R.C. Rowley, R.C. Thompson. Opt. Comm. 54 217. (1985).

[16] B.N. Taylor. Private communication of work carried out in connection with the 1985 least squares readjustment of the fundamental constants.

[17] G. Erickson. J. Phys. Chem. Ref. Data. 6 831. (1971).

[18] P. Mohr. Phys. Rev. Lett. 34 1050. (1975).

[19] J. Saperstein. Phys. Rev. Lett. 47 1723. (1981).

[20] R.G. Beausoleil, T.W. Hänsch. Optics. Lett. 10 547. (1985).

[21] C.J. Foot, B. Couillard, R. Beausoleil, T.W. Hänsch. Phys. Rev. Lett. 54 1913. (1985).

[22] C.J. Foot, P.E.G. Baird, M.G. Boshier, D.N. Stacey, G.K. Woodgate. Opt. Comm. 50 199. (1984).

[23] H.A. Bethe, E. Saltpeter. "Quantum Mechanics of One- and Two-Electron Atoms". Plenum. (1977).

[24] L.A. Rahn. Appl.Optics. 24 940. (1985).

[25] P. Kumar, R.S. Bondurant. Appl. Optics. 22 1284. (1983).

A.1. Previous measurements of the $1S_{1/2}$ and $2S_{1/2}$-$2P_{1/2}$ Lamb shifts.

A list of Lamb shift measurements is given in [1] which is complete until September 1976. From this table measurements relating to the $1S_{1/2}$ Lamb shift in hydrogen and deuterium have been extracted and displayed in Table A.1. Recent accurate measurements on the $2S_{1/2}$-$2P_{1/2}$ have been included in order to highlight the experimental discrepancies still remaining. Table A.2 lists the three theoretical values for the $2S_{1/2}$-$2P_{1/2}$ Lamb shifts showing that there is fundamental disagreement between the various approaches and between theory and experiment. There is fair agreement between Saperstein's value for the Lamb shift and experiment, but insufficient details are given in his paper on the proton size assumed in his calculation [8] to be sure that the same constants where used in each calculation. The major difference between these calculations is in the value of C_{60} used in the electron structure corrections. Table A.3 demonstrates the difference in {ZA2 ETC} using the various values of C_{60}.

Appendix A.

Table A.1.

Atom	Interval	Measured	Reference
H	$1S_{1/2}-1S_{1/2}$	8600±800 MHz	[2]
		8.20±0.10 GHz	[3]
		8151±30 MHz	[4]
	2S -2P	1057.845±0.009 MHz	[5]
		1057.8594±0.0019 MHz	[6]
D	1S -1S	0.262±0.038 cm	[7]
		8300±300 MHz	[2]
		8.25±0.110 GHz	[3]
		8177±30 MHz	[4]

Summary of the Lamb shifts of the n=1 and n=2 levels in hydrogen and deuterium. The values given here are those quoted in the relevant papers. The values from references [2,3,4] include the recoil correction.

Appendix A.

Table A.2.

Erickson [1,8]	1057.934±0.010 MHz
Mohr [8,9]	1057.888±0.014 MHz
Saperstein [10]	1057.860±0.009 MHz

Comparison of the various theoretical predictions for the $2S_{1/2}$-$2P_{1/2}$ Lamb shift. Both Mohr's and Erickson's results have been corrected for the new value of the proton radius.

Table A.3

	{ZAZ ETC}	C_{60}
Erickson	-1.105 MHz	-19.343(500)
Mohr	-1.331 MHz	-23.25(1.25)
Saperstein	-1.426 MHz	-24.9(9)

Values of {ZA2 ETC} for the ground state Lamb shift predicted using the values of C_{60} calculated by Erickson [1], Mohr [9] and Saperstein [10]. The predictions differ by about 300 kHz.

Appendix A.

A.2. Contributions to the Lamb shift.

A full list of the contributions to the Lamb shift as detailed in Erickson [1] are presented here. This is to enable the origin of the terms given in Table 2.2 to be traced. A listing is also given of a program written to calculate the Lamb shift of levels in H and D. This is fully annotated so that improvements in theory and the experimental values of fumdamental constants can be incorporated.

{IR LOG} $$\frac{4\alpha(Z\alpha)^4 m_e c^2}{3\pi n^3}\left(\frac{\mu}{m_e}\right)^3\left[\left\{\ln\left(\frac{1}{Z\alpha}\right)^2+\ln\left(\frac{m_e}{\mu}\right)+\frac{11}{24}\right\}\delta_{\ell 0}+L_n\right] \quad \text{(A2.1)}$$

where L_n is defined after (2.12) in reference [1]

{MAG MOM} $$\frac{4\alpha(Z\alpha)^4 m_e c^2}{3\pi n^3}\left(\frac{\mu}{m_e}\right)^3\left[\frac{3}{8}\delta_{\ell 0}+\frac{3}{8}\left(\frac{m_e}{\mu}\right)\frac{C_{\ell j}}{2\ell+1}\right] \quad \text{(A2.2)}$$

where $C_{\ell j}$ is defined after (2.2)

{VAC POL} $$\frac{4\alpha(Z\alpha)^4 m_e c^2}{3\pi n^3}\left(\frac{\mu}{m_e}\right)^3\left[-\frac{1}{5}\delta_{\ell 0}\right] \quad \text{(A2.3)}$$

{(HTOT)} $$\frac{4\alpha(Z\alpha)^4 m_e c^2}{3\pi n^3}\,H(Z\alpha) \quad \text{(A2.4)}$$

where (HTOT) = ZA +ZA2 LL + ZA2 ETC.

{ZA} $$\frac{4\alpha(Z\alpha)^4 m_e c^2}{3\pi n^3}\left(Z\alpha\, C_5\right)$$

(A2.5)

{ZA2 LL} $$\frac{4\alpha(Z\alpha)^4 m_e c^2}{3\pi n^3}\left((Z\alpha)^2\, \ln^2 (Z\alpha)^2\, C_{62}\right)$$

(A2.6)

{ZA2 L} $$\frac{4\alpha(Z\alpha)^4 m_e c^2}{3\pi n^3}\left((Z\alpha)^2\, \ln^2\!\left(\frac{1}{Z\alpha}\right)^2 C_{61}\right)$$

(A2.7)

{ZA2 ETC} $$\frac{4\alpha(Z\alpha)^4 m_e c^2}{3\pi n^3}\left((Z\alpha)^2\left\{C_{60} + C_{70}(Z\alpha)\right\}\right)$$

(A2.8)

{AL} $$\frac{4\alpha(Z\alpha)^4 m_e c^2}{3\pi n^3}\left\{\frac{\alpha^2}{\pi^2}(0\cdot 470)\right\}\delta_{\ell 0}$$

(A2.9)

{A MM} $$\frac{(Z\alpha)^4 m_e c^2}{n^3}\left(\frac{C_{\ell j}}{2\ell+1}\right)\left[-\left(\frac{\alpha}{\pi}\right)^2(0\cdot 328) + \left(\frac{\alpha}{\pi}\right)^3(1\cdot 285)\right]$$

(A2.10)

{A VP} $$-\frac{82}{81}\left(\frac{\alpha}{\pi}\right)^2\frac{(Z\alpha)^4 m_e c^2}{n^3}\,\delta_{\ell 0}$$

(A2.11)

{RM/N4} $$-\frac{(Z\alpha)^4 \mu^2 c^2}{8n^4(m_e+M)} - \frac{\mu^2 (Z\alpha)^4 \mu c^2 C_{\ell j}}{M^2\, 2n^3\,(2\ell+1)}\left(1-\delta_{\ell 0}\right)$$

(A2.12)

{RM(BS)} $$\frac{\mu^3}{m_e M}\,\frac{4(Z\alpha)^5 c^2}{3\pi n^3}\left(2\left[\left(\ln\left(\frac{1}{Z\alpha}\right)^2 + \frac{11}{24}\right) + L_n\right]\right.$$

$$-\frac{7}{2}\left[\left(\ln\left(\frac{n}{2Z\alpha}\right) - \sum_1^n i + \frac{1}{2n} - 1\right)\delta_{\ell 0} + \frac{1-\delta_{\ell 0}}{2\ell(\ell+1)(2\ell+1)}\right]$$

$$\left. - \delta_{\ell 0} + \frac{2-\frac{7}{2}}{M^2 - m_e^2}\left[M^2 \ln\left(\frac{m_e}{\mu}\right) - m_e^2 \ln\left(\frac{M}{\mu}\right)\right]\delta_{\ell 0}\right)$$

(A2.13)

{NUCSTR} $$\frac{\langle r^2\rangle}{\left(\frac{\hbar}{m_e c}\right)^2}\;\frac{2(Z\alpha)^4 m_e c^2}{3n^3}\left[\left(1 + C_{str}\right)\delta_{\ell 0} + (1-\delta_{\ell 0})\left(\frac{5}{5+2\ell}\right)\left(\frac{\langle r^2\rangle}{a^2}\right)^{\ell}\right]$$

(A2.14)

where C_{str} is -0.004±0.002 for H and -0.0147±0.0055 for other nuclei. The RMS radius of the nucleus $\langle r^2 \rangle$ is given in [1] Table A.

$$a = \frac{n\hbar}{Z\alpha m_e c}$$

is the Bohr radius.

$$\{\mathrm{HO\ VP}\} \quad \frac{4\alpha(Z\alpha)^4 m_e c^2}{\pi n^3}\left[\frac{5\pi}{192}(Z\alpha) - \frac{3}{35}(Z\alpha)^2 + \frac{7\pi}{256}(Z\alpha)^3 + \dots\right]$$

$$+ \frac{4\alpha(Z\alpha)^4 m_e c^2}{\pi n^3}\left(\frac{m_e}{m_\mu}\right)^2\left[-\frac{1}{5} + \frac{5\pi}{192}\left(\frac{m_e}{m_\mu}Z\alpha\right) - \frac{3}{35}\left(\frac{m_e}{m_\mu}Z\alpha\right)^2 + \frac{7\pi}{256}\left(\frac{m_e}{m_\mu}Z\alpha\right)^3 + \dots,\right]$$

$$- \frac{2}{15}\frac{\alpha}{\pi}\frac{(Z\alpha)^6 m_e c^2}{n^3}\delta_{\ell 0}\left(\frac{\ln\left(\frac{1}{Z\alpha}\right)^2}{1-(Z\alpha)^2}\left[1 - 3(Z\alpha)^2\right] + 2(Z\alpha)^2\right)\frac{1}{\left[1-(Z\alpha)^2\right]^2}$$

(A2.15).

Appendix A.

References.

[1] G. Erickson. J. Phys. Chem. Ref. Data 6 831. (1977).

[2] T.W. Hänsch, S.A. Lee, R. Wallenstein, C. Wieman. Phys. Rev. Lett. 34 307. (1975).

[3] S.A. Lee, R. Wallenstein, T.W. Hänsch. Phys. Rev. Lett. 35 1262. (1975).

[4] C. Wieman, T.w. Hänsch. Phys. Rev. A. 22 192. (1980).

[5] S.R. Lunden, F.M. Pipkin. Phys. Rev. Lett. 46 232. (1981).

[6] Yu. Sokolov, V. Yakovlev. Sov. Phys. J.E.T.P. 56 7. (1982).

[7] G. Herzberg. Proc. Roy. Soc. 234A 516. (1956).

[8] P. Pellegrin, Y.El. Masri, L. Palffy. Phys. Rev. A. 31 5. (1985).

[9] P. Mohr. Phys. Rev. Lett. 34 1050. (1975).

[10] J. Saperstein. Phys. Rev. Lett. 47 1723. (1981).

Appendix A.

```
    1 REM J. Hey. 1983
    2 REM corrected and adapted
    3 REM by J.R.M. Barr. 1985
    5 MODE7
   10 CLS:PRINT'''
  100 PROCinit
  110 INPUT"H OR D":Y$=GET$:IF Y$<>"H" AND Y$<>"D" THEN 110

  120 IF Y$="H" THEN I1=1 ELSE I1=2
  125 PRINT
  130 INPUT"Principle Q.N "N:N=INT(N):IF N<1 OR N>7 THEN
130
  140 INPUT"Angular mom. "L:L=INT(L):IF L<0 OR L>N-1 THEN
140
  150 INPUT"Total Angular mom. "J:IF J<>L-.5 AND J<>L+.5
THEN 150
  155 N9=N:L9=L:J9=J
  160 PROCelecstr(N)
  170 PROCsum
  175 I=I1:N=N9:L=L9:J=J9
  176 IF J=ABS(L-.5) THEN K=1 ELSE K=2
  180 PROCdelta
  190 PROCrmn4
  200 PROCnucstr
  210 PROCirlog
  220 PROCrmbs
  225 PROCza
  230 PROCa
  240 PROChovp
  300 CLS:PRINT''
  310 PRINT"LAMB SHIFT    "
  320 @%=&00020103
  330 PRINT"Z=1.0 mass£="I" n="N" l="L" j="J
  335 @%=&0002050A
  340 PRINT'"Ir log  ",irlog/1E6*C
  350 PRINT"Magmom  ",magmom/1E6*C
  360 PRINT"Vacpol  ",vacpol/1E6*C
  370 PRINT" Za     ",za/1E6*C
  380 PRINT"Za LL   ",za2ll/1E6*C
  390 PRINT"Za L    ",za2l/1E6*C
  400 PRINT"ZaEtc   ",za2etc/1E6*C
  410 PRINT"(Htot)  ",htot/1E6*C
  420 PRINT"Ho Vp   ",hovp/1E6*C
  430 PRINT" A L    ",al/1E6*C
  440 PRINT" A MM   ",amm/1E6*C
  450 PRINT" A Vp   ",avp/1E6*C
  460 PRINT" Rm/N4  ",rmn4/1E6*C
  470 PRINT" Rm(bs) ",rmbs/1E6*C
  480 PRINT"Nucstr  ",nucstr/1E6*C
```

```
  500
shift=irlog+magmom+vacpol+htot+hovp+al+amm+avp+rmbs+nucstr
  510 PRINT"LAMB SHIFT ",shift/1E6*C
  520 END
  990 DEF PROCinit
 1000DIMB(7,7)
 1010DIMM(2),R2(2),C0(2)
 1020DIMC(7,7,2,5)
 1030READC,A,M,R1,R0,MU
 1031 PROCnucmass
 1032 PROCelecstrcoef
 1039 ENDPROC
 1040 DEF PROCnucmass
 1050FORI=1TO2
 1060READM(I),R2(I),C0(I)
 1070M(I)=M(I)/M
 1080R2(I)=R2(I)^2
 1090NEXTI
 1100 ENDPROC
 1110 DEF PROCelecstrcoef
 1120 FOR N=1 TO 7
 1130L0=N-1
 1140FORL=0TOL0
 1150IFN>5THEN1180
 1160READB(N,L)
 1170GOTO1280
 1180IFL>0THEN1210
 1190B(N,L)=-2.71631-0.02402*(5/N)^(3/2)
 1200GOTO1280
 1210IFL>1THEN1240
 1220B(N,L)=0.0525-0.00838*(5/N)^(3/2)
 1230GOTO1280
 1240IFL>2THEN1270
 1250B(N,L)=0.01148224*(1-(2/N)^(3/2))
 1260GOTO1280
 1270B(N,L)=0.1623834*((1/L)^(3/2)-(1/N)^(3/2))/(2*L+1)
 1280NEXTL
 1290NEXTN
 1300 ENDPROC
 1310 DEF PROCsum
 1320 W=0
 1330 FOR I0=1TON:W=W+1/I0:NEXTI0:ENDPROC
 1340 DEF PROCdelta:IFL=0 THEN D=1 ELSE D=0:ENDPROC
 1350 DEF PROCrmn4
 1360S1=M(I)^2/(1+M(I))^3
 1370X1=-R0*A^2/(4*N^4)
 1380 rmn4=X1*S1
 1390 PROCspinorbit
 1400 ENDPROC
 1410 DEF PROCnucstr
 1420S=32*PI^2/3
 1430X=R2(I)*R0^2/(R1*N^3)
 1440X=X*(1+C0(I))
 1450nucstr=S*X*D
```

```
1460 ENDPROC
1470 DEF PROCspinorbit
1480S=-R0*M(I)/(1+M(I))^3*A^2/N^3
1490IFL=0THEN1560
1500K1=J-L-1/2
1510IFK1=0THEN1540
1520X=-1/(L*(2*L+1))
1530GOTO1570
1540X=1/((L+1)*(2*L+1))
1550GOTO1570
1560X=0
1570rmn4=rmn4+S*X
1580 ENDPROC
1590 DEF PROCirlog
1600S=8*A^3*R0/(3*PI)*N^(-3)
1610X=(M(I)/(1+M(I)))^3
1620irlog=S*X
1630B=D*(LN(1/A^2)+11/24)+B(N,L)
1640F=D*(LN((1+M(I))/M(I)))
1650 vacpol=-1/5*D*irlog:magmom=3/8*D*irlog
1660irlog=irlog*(B+F)
1680S=A^3*R0/(PI*N^3)
1690S=S*(M(I)/(1+M(I)))^2
1700IFL=0THEN1770
1710K1=J-L-1/2
1720IFK1=0THEN1750
1730X=-1/(L*(2*L+1))
1740GOTO1780
1750X=1/((L+1)*(2*L+1))
1760GOTO1780
1770X=0
1780magmom=magmom+S*X
1790ENDPROC
1800 DEF PROCrmbs
1810S=8/(3*PI)*N^(-3)*A^3*R0
1820X=M(I)^2/(1+M(I))^3
1830rmbs=S*X
1840B0=2*((LN(1/A^2)+11/24)*D+B(N,L))
1850B=-D-7/2*D*(LN(N/(2*A))-W+(2*N)^(-1)-1)
1860IFL=0THEN1890
1870B1=-7/2*1/(2*L*(L+1)*(2*L+1))
1880GOTO1900
1890B1=0
1900B=B+B1+B0
1910F=D*(-3/2*1/(M(I)^2-1))
1920F=F*(M(I)^2*LN((1+M(I))/M(I))-LN(1+M(I)))
1930rmbs=rmbs*(B+F)
1940 ENDPROC
1950 DEF PROCa
1960avp=-D*164/81*A^4*R0/(PI^2*N^3)
1970a1=D*3.76*A^4*R0/(PI^2*N^3)
1980K1=J-L-1/2
1990IFK1=0THEN2020
2000X=-1/(L*(2*L+1))
```

```
 2010GOTO2030
 2020X=1/((L+1)*(2*L+1))
 2030S=1.285*(A/PI)^3-0.328*(A/PI)^2
 2040amm=2*S*A^2*R0*X*1/N^3
 2050ENDPROC
 2060 DEF PROCza
 2070S=8*A^4*R0/(3*PI*N^3)
 2080za=S*C(N,L,K,1):za211=S*A*(LN(1/A^2))^2*C(N,L,K,2):za2
1=S*A*LN(1/A^2)*C(N,L,K,3)
 2090za2etc=S*(A*C(N,L,K,4)+A^2*C(N,L,K,5))
 2100htot=za+za211+za21+za2etc
 2110 ENDPROC
 2120 DEF PROChovp
 2130MU=1/MU
 2140IF D=0 THEN hovp=0:GOTO2220
 2150S=4*R0*A^3/(PI*N^3)
 2160X=(LN((1/A)^2)*(1-3*A*A)/(1-A*A)+2*A*A)/((1-A*A)^2)
 2170 X=-X*S*A*A/15
 2180 Y=-MU*MU/15+5*PI/192*(MU^3+1)*A
 2190 Y=Y-3/35*(MU^4+1)*A*A+7*PI/256*(MU^5+1)*A^3
 2200 Y=Y*2*S
 2210 hovp=Y+X
 2220 ENDPROC
 2230 DEF PROCelecstr(N)
 2235 FOR N=1 TO 7
 2240L0=N-1
 2250FORL=0 TO L0
 2260J0=ABS(L-1/2)
 2270J1=L+1/2
 2280K=0
 2290FORJ=J0 TO J1
 2300K=K+1
 2310FORI=1 TO 5
 2320IFN>4THEN2350
 2330READC(N,L,K,I)
 2340GOTO2400
 2350IFL>0THEN2390
 2360IFI>1THEN2390
 2370C(N,L,K,I)=6.968
 2380GOTO2400
 2390C(N,L,K,I)=0
 2400NEXTI
 2410NEXTJ
 2420NEXTL
 2425 NEXT N
 2430 ENDPROC
 2440DATA2.99792458E10            :velocity of light
 2450DATA7.29735449E-3            :fine structure constant
 2460DATA5.44617082E-4            :mass ratio
 2470DATA2.4263089E-10            :Compton wavelength
 2480DATA109737.31521             :Rydberg constant
 2490DATA206.76865                :electron muon mass ratio
 2500DATA1.00,0.862E-13,-0.004 :proton mass,proton radius,Cstr
 2510DATA2.01355323474,2.096E-13,-0.0147:deuterium data
```

Appendix A.

```
2520DATA-2.9841285559           :Bethe logarithms
2530DATA-2.8117688932
2540DATA0.0300167089
2550DATA-2.7676990000
2560DATA0.0381885200
2570DATA0.0052321000
2580DATA-2.7498590000
2590DATA0.0419540000
2600DATA0.0074226551
2610DATA0.0015646821
2620DATA-2.7403300000
2630DATA0.0441200000
2640DATA0.0085774375
2650DATA0.0023895267
2660DATA0.0006415458
2670DATA6.968,-0.75,4.065,-24.9,30.04  :C5 ,C62 ,C61 ,C60 ,C7
2680DATA6.968,-0.75,4.448,-17.598,18.48
2690DATA0,0,0.429,-0.352,-1.28
2700DATA0,0,0.242,-0.438,-0.32
2710DATA6.968,-0.75,4.409,-17.339,17.18
2720DATA0,0,0.496,-0.396,-1.58
2730DATA0,0,0.274,-0.497,-0.36
2740DATA0,0,0.00741,-0.020,0.09
2750DATA0,0,0.00741,-0.02,-0.06
2760DATA6.968,-0.75,4.359,-17.268,17.00
2770DATA0,0,0.52,-0.412,-1.68
2780DATA0,0,0.285,-0.519,-0.37
2790DATA0,0,0.00833,-0.024,0.088
2800DATA0,0,0.00833,-0.024,-0.059
2810DATA0,0,0.00119,-0.0039,0.042
2820DATA0,0,0.00119,-0.0039,-0.031
2830END
```

Appendix B.

Interferometry.

It is well known that Fabry-Perot type resonators can be used as frequency selective elements. This appendix discusses the various uses made of spherical mirror interferometers in this experiment. The usefulness of this type of interferometer is emphasised [1,2,3,4,5].

The properties of the confocal interferometer are discussed in two ways. Firstly, Gaussian beams [1,3,6] which represent the fundamental field distributions within such a resonator are used to deduce the resonant frequencies and the transmission as a function of frequency. Another analysis of the confocal interferometer is also given in which off-axis ray paths are considered [2,4,5]. This analysis is suitable for considering the aberrations of spherical mirrors which are used sufficiently far off axis that the paraxial condition, for which Gaussian beams are valid, is broken. Using the results of this analysis the maximum useable aperture of a confocal resonator is derived.

B.1. Resonator analysis.

It can be shown that a resonator consisting of two mirrors of radius of curvature R_1 and R_2 can support electric fields whose spatial distribution is described by

$$E_{\ell m}(r,z) = E_0 \frac{\omega_0}{\omega(z)} H_\ell\left(\frac{\sqrt{2}\,x}{\omega(z)}\right) H_m\left(\frac{\sqrt{2}\,y}{\omega(z)}\right) \exp\left[-\frac{iKr^2}{q(z)} - iKz + i(\ell+m+1)\tan\left(\frac{z}{z_0}\right)\right]$$

(B1.0,1)

where

$$\omega^2(z) = \omega_0^2\left[1 + \left(\frac{z}{z_0}\right)^2\right]$$

$$\frac{1}{q(z)} = \frac{1}{R(z)} - \frac{i\lambda}{\pi\,\omega^2(z)\,n}$$

$$R(z) = z\left[1 + \left(\frac{z_0}{z}\right)^2\right]$$

$$r^2 = x^2 + y^2$$

$$K = \frac{2\pi n}{\lambda}$$

The beam is propagating along the z-axis. $\omega(z)$ is the radius of the fundamental l=m=0 Gaussian beam defined as the distance off-axis for which the electric field drops to $1/e$ of its axial value. ω_0 is the beam waist and occurs at z=0. It is the smallest value of the beam radius. z_0 is the distance over which $\omega(z)$ grows to $\sqrt{2}\,\omega_0$. A related quantity $b=2z_0$ is called the confocal parameter because it is the separation of two mirrors with radius of curvature $R_1 = R_2 = b$ which forms a confocal interferometer with a spot size ω_0.

$$z_0 = \frac{\pi \omega_0^2 n}{\lambda}$$

where n is the refractive index of the medium between the mirrors. $R(z)$ is the radius of curvature of the Gaussian beam wavefront at z. The complex beam parameter $q(z)$ enables the values of the spot size and radius of curvature to be calculated and transforms by the ABCD law [1,6] as

$$q_2 = \frac{Aq_1 + B}{Cq_1 + D}$$

(B1.0,2)

where A,B,C and D are elements of the transformation matrix calculated according to geometric optics [1,6] and q_1 is the complex beam parameter before transformation. The integers l and m define the order of the mode and through the Hermite polynomials H_l and H_m they describe the transverse energy distribution.

B1.1. Location and size of beam waists.

Consider a resonator formed by two mirrors of radius of curvature R_1 and R_2, separated by a distance $L=z_2-z_1$, where z_2 and z_1 are the mirror positions relative to the beam waists. It is possible to show that the condition that after one round trip round the resonator $q_1 = q_2$ and q_1 is imaginary is equivalent to $R(z_1) = R_1$ and $R(z_2) = R_2$ [1,3]. There is a sign convention that concave mirrors to the right of the beam waist have positive radius of curvature and to the left of the beam waist have negative radius of curvature. The result is

$$R_1 = z_1 + \frac{z_0^2}{z_1}$$

$$R_2 = z_2 + \frac{z_0^2}{z_2} \qquad \text{(B1.1,1)}$$

Thus

$$L = z_2 - z_1$$

$$z_1 = \frac{R_1}{2} \pm \frac{1}{2}\sqrt{R_1^2 - 4z_0^2}$$

$$z_2 = \frac{R_2}{2} \pm \frac{1}{2}\sqrt{R_2^2 - 4z_0^2} \qquad \text{(B1.1,2)}$$

and

$$\omega_0^4 = \left(\frac{\lambda}{\pi n}\right)^2 \frac{L(-R_1 - L)(R_2 - L)(R_2 - R_1 - L)}{(R_2 - R_1 - 2L)^2} \qquad \text{(B1.1,3)}$$

We note immediately that for some values of R_1, R_2 and L no solution exists and the resonator is unstable [1,3,5]. Also for a given spot size ω_0 there are two possible positions of each mirror or a total of four "different" resonators with respect to the $z=0$ plane. It is demonstrated in [2] that for given resonator length L and spot size ω_0 the two physically distinct resonators have similar diffraction losses. For a confocal resonator $R_1=R_2=2z_0$ the spot size is calculated using (B1.1,3) to be

$$\omega_0 = \sqrt{\frac{\lambda z_0}{\pi n}}$$

Also the resonator is very close to being unstable.

B1.2. Resonant frequencies.

The resonant frequencies are calculated by requiring that the round trip phase change of the electric field of (B1.0,1) is an integer multiple of 2π. This ensures that the electric field at the output remains in phase. The effect of relaxing this condition will be explored later. The reflectivity of each mirror will be written as $r_1 e^{i\phi}$ where ϕ is the phase change on reflection [8,9,10] and depends upon the material used to coat the mirror. Using (B.1.0,1) the phase change for one round trip is

$$\delta = 2\pi q = 2\left[k z_2 - (\ell+m+1)\tan^{-1}\left(\frac{z_2}{z_0}\right) - k z_1 + (\ell+m+1)\tan^{-1}\left(\frac{z_1}{z_0}\right)\right] + \phi_1 + \phi_2$$

The resonant frequencies $\nu_{q\ell m} = \frac{2\pi c n}{\lambda}$ are given by

Appendix B.

$$\nu_{q\ell m} = \left(\frac{c}{2Ln}\right)\left\{ q + \frac{1}{\pi}(\ell+m+1)\left[\tan^{-1}\left(\frac{z_2}{z_0}\right) - \tan^{-1}\left(\frac{z_1}{z_0}\right)\right] - \left(\frac{\phi_1+\phi_2}{2\pi}\right) \right\}$$

(B1.2,1)

By combining (B1.1,1) and (B1.1,3) this may be written in a more usual form as

$$\nu_{q\ell m} = \left(\frac{c}{2Ln}\right)\left\{ q + \frac{1}{\pi}(\ell+m+1)\cos^{-1}\sqrt{\left(1-\frac{L}{R_1}\right)\left(1-\left(\frac{L}{R_2}\right)\right)} - \left(\frac{\phi_1+\phi_2}{2\pi}\right) \right\}$$

(B1.2,2)

The form of this result arises from q , which is normally a large integer equal to the number of half wavelengths of a plane-plane cavity of length L . The second term corrects for the geometric phase shift which is different for Gaussian beams when compared with plane waves. The final term is the correction for the phase shift on reflection and makes the cavity appear shorter than its geometric length [10].

When the round trip phase change δ is not equal to an integer multiple of 2π , interference between successive round trips modifies the transmitted electric field. A Gaussian beam $E(r,z,t)$ incident upon the cavity is transmitted entirely, providing it matches one of the spatial and spectral cavity modes. If the frequency of the incoming beam does not match one of the resonant frequencies then part of the beam is reflected and the transmission reduced. Let t_1 and t_2 be the electric field transmission of the mirrors. The transmitted field is

$$E_T(r,z,t) = \sum_{n=0}^{\infty} E(r,z,t-n\tau)\, e^{in\delta}\, t_1 t_2 (r_1 r_2)^n$$

(B1.2,3)

where τ is the round trip time of the resonator $\tau = \frac{2L}{c}$ and n is the number of round trips. Assuming the input field is monochromatic then

$$E_T(r,z) = \frac{E(r,z)\, t_1 t_2}{1 - r_1 r_2 e^{i\delta}}$$

This results in the familiar result for the intensity transmission of a plane-plane Fabry-Perot modified for phase shifts on reflection and differing mirror reflectivities [10,11].

$$\frac{I_T}{I} = \frac{E_T E_T^*}{E\, E^*} = \frac{T_1 T_2}{(1-\sqrt{R_1 R_2})^2 \left\{ 1 + \frac{4\sqrt{R_1 R_2}}{(1-\sqrt{R_1 R_2})^2} \sin^2 \delta/2 \right\}}$$

(B1.2,4)

Here $T_1 = t_1^2$, $R_1 = r_1^2$. R_1 and R_2 in this context refer to mirror reflectivity and should not be confused with the mirror radius of curvature used elsewhere. Dimensional analysis should identify the relevant meaning. Maximum transmission occurs when $\frac{\delta}{2} = \pi q$ when the incoming light frequency matches one of the cavity longitudinal modes.

$$\frac{I_T}{I}\,(\delta = 2\pi q) = \frac{T_1 T_2}{\left(1 - \sqrt{R_1 R_2}\right)^2}$$

The intensity transmission and reflection coeffocients are related by

$$R_i + T_i + A_i = 1 \qquad i = 1,2$$

and A_i is the loss in the mirror coating. If there is no loss and $T_1 = T_2$, then the transmission is unity. In all other cases the maximum transmission is less than unity. As a function of cavity length or round trip phase change the transmitted light will appear to have a series of maxima which are separated by a phase change δ of 2π . This means that the inferometer can only unambiguously measure round trip phase differences which are less than 2π . This corresponds to a frequency difference

$$\nu_{FSR} = \nu_{q\ell m} - \nu_{q+1\,\ell m} = \frac{c}{2Ln}$$

where ν_{FSR} is the free spectral range of the cavity. The transmitted intensity drops to half its resonant value away from a maximum when

$$\frac{4\sqrt{R_1 R_2}}{\left(1 - \sqrt{R_1 R_2}\right)^2}\,\sin^2\frac{\left(2\pi q + \delta_{1/2}\right)}{2} = 1$$

Appendix B.

Making the assumption that $\delta_{1/2} << 2\pi$, the full width at half maxima is given by

$$2\delta_{1/2} = \frac{2(1-\sqrt{R_1R_2})}{(R_1R_2)^{1/4}}$$

The maximum number of such peaks that can be fitted into one free spectral range (F.S.R.) of the interferometer is

$$F = \frac{2\pi}{2\delta_{1/2}} = \frac{\pi(R_1R_2)^{1/4}}{1-\sqrt{R_1R_2}}$$

(B1.2,5)

The importance of this quantity F, known as the finesse, may be appreciated by considering a practical example. Interferometers are often used as spectrum analysers, for example to ensure a single frequency dye laser is indeed single frequency. Assume a beam containing two monochromatic frequency components separated by less than one free spectral range is incident on the interferometer. The interferometer length is scanned over a number of free spectral ranges using a mirror mounted on a piezo electric crystal, and the transmitted intensity is monitored. The minimum phase difference that can be resolved will then be $2\delta_{1/2}$ which is analogous to Rayleigh's criteria [6]. (This is an approximation since the resolution will depend on the relative heights of the transmitted components [7,11]). The minimum resolvable frequency or bandpass of the interferometer $\Delta\nu$ is calculated by

$$\Delta\nu = \nu_{FSR}\,\frac{\delta_{1/2}}{\pi} = \frac{\nu_{FSR}}{F}$$

(B1.2,6)

B1.3. Mode structure of confocal interferometers.

The resonant frequency for a confocal interferometer is given by (B1.2,2)

$$\nu_{q\ell m} = \frac{c}{2Ln}\left\{ q + \frac{1}{2}(\ell+m+1) - \left(\frac{\phi_1+\phi_2}{2\pi}\right)\right\}$$

Assuming that ϕ_1 and ϕ_2 do not depend strongly on frequency [10], then $\nu_{q00} = \nu_{q-1\,20} = \nu_{q-2\,40}$ and $\nu_{q10} = \nu_{q-1\,30} = \nu_{q-2\,50}$. That is, the resonant frequency spectrum of a confocal interferometer is degenerate. A monochromatic input beam which is not spatially modematched into a confocal interferometer will excite many transverse modes. However, scanning the interferometer length reveals that the transmitted spectrum remains simple with a free spectral range

$$\nu_{FSR} = \frac{c}{4Ln}$$

(B1.3,1)

The reason for this is that decreasing q by 1 may be compensated for by increasing the sum l+m by 2. The sum l+m may be odd, l+m=1,3,5.... or even, l+m=0,2,4.... and the separation $\nu_{q\,(l+m)_{even}} - \nu_{q\,(l+m)_{odd}}$ is a multiple of $\frac{c}{4Ln}$. Hence the free spectral range of a non modematched confocal interferometer is half of a modematched interferometer. The degeneracy explains why a confocal interferometer is so useful. The transverse modes do not have to be discriminated against, so complex positioning and focussing of the input beam are unnecessary.

B1.4. Geometric ray analysis of confocal interferometers.

A ray injected into a confocal interferometer parallel to and a distance r from the optic axis will form a closed path as illustrated in fig. B.1. The length of this ray if the mirrors are separated by a distance $R+\delta$ is

$$2\left[R+\delta-2x(r)\right] + 2\sqrt{4r^2+\left[R+\delta-2x(r)\right]^2}$$

(B1.4,1)

The path length correct to terms of order $\frac{\delta r^4}{R^4}$, $\frac{r^6}{R^5}$, $\frac{\delta^2 r^2}{R^3}$ is

Appendix B.

$$P.L. = 4(R+\delta) - \frac{4r^2\delta}{R^2} - \frac{r^4}{R^3} + \left(\frac{4r^2}{R} - 8x(r)\left(1 - \frac{r^2}{R^2}\right) - \frac{3r^4}{R^3}\right)$$

(B1.4,2)

If the mirrors are parabolic, ie. $x(r) = \frac{1}{2}\frac{r^2}{R}$ then

$$P.L. = 4(R+\delta) - \frac{4r^2\delta}{R^2}$$

A confocal mirror path length for $\delta = 0$ is independent of the radial distance off axis. This result implies that there is no aperture limitations on the use of a confocal interferometer with parabolic mirrors. The use of Gaussian beams which are valid for paraxial optics also assumes this result implicitly.

Further information may be obtained from this geometric analysis by choosing $x(r) = \frac{1}{2}\frac{r^2}{R} + \frac{1}{8}\frac{r^4}{R^3}$, in this case the bracketed term in (B1.4,2) vanishes and the path length is

$$P.L. = 4(R+\delta) - \frac{4r^2\delta}{R^2} - \frac{r^4}{R^3}$$

(B1.4,3)

which is given in [2,4,5]. This result is valid for spherical mirrors and spherical aberration has introduced an extra term for the off axis paths. If the interferometer is not illuminated close to the axis a reduction in resolution occurs due to spherical aberration. The round trip phase change δ_T neglecting the phase change on reflection is given by

$$\delta_T = \frac{2\pi}{\lambda}\left\{ 4(R+\delta) - \frac{4r^2\delta}{R^2} - \frac{r^4}{R^3} \right\}$$

$$= \delta_0 - \delta(r)$$

where $\delta(r)$ is the off axis change relative to the on axis phase change $\delta_0 = \frac{2\pi}{\lambda}(4(R+\delta))$. As in fig. B.1 the two possible output beams are labelled $\rho = 0,1$. An analysis similar to that leading to (B1.4,4) gives

$$\frac{I_T^\rho}{I} = \frac{T_1 T_2 \, (R_1 R_2)^\rho}{(1-R_1R_2)^2 \left\{ 1 + \frac{4(R_1R_2)}{(1-R_1R_2)^2} \sin^2\left(\frac{\delta_T}{2}\right) \right\}}$$

(B1.4,4)

and is valid providing the two beams $\rho = 0,1$ do not overlap otherwise a multiple beam interference pattern results. The finesse is given by

$$F = \frac{2\pi}{2\delta_{1/2}} = \frac{\pi (R_1R_2)^{1/2}}{(1-R_1R_2)}$$

(B1.4,5)

and the free spectral range corresponding to a change in δ_T of 2π is

Appendix B.

$$\nu_{FSR} = \frac{c}{4 L n}$$

(B1.4,6)

which agrees with the non modematched confocal case. It is important to know if the linewidth depends on whether the interferometer is modematched or not. This is found by forming the ratio

$$\frac{\Delta \nu_{\text{off axis}}}{\Delta \nu_{\text{mode matched}}} = \left(\frac{1}{2}\right) \frac{1-R^2}{R} \frac{\sqrt{R}}{1-R}$$

$$= \frac{1}{2} \frac{1+R}{\sqrt{R}} \sim 1$$

Here it has been assumed that $R_1 = R_2$, $T_1 = T_2$ and no losses. It can be seen that if $R>0.9$ then the bandwidth is effectively independent of the method of use of the interferometer.

The influence of the spherical aberration becomes important when $\delta_r \sim 2\delta_{1/2}$. In this case the difference in resonant frequencies between the on axis and off axis path may be resolved by the interferometer. For best resolution then

$$\frac{2\pi}{\lambda}\left(\frac{4r^2\delta}{R^2} + \frac{r^4}{R^3}\right) < \frac{2\pi}{F}$$

If the interferometer is confocal $\delta=0$, the maximum useable radius is given by

$$r_{max} = \left(\frac{R^3\lambda}{F}\right)^{1/4}$$

(B1.4,7)

Alternatively, if the detuning from the confocal condition is sufficiently large, the useable diameter is

$$r_{max} = \left(\frac{R^2\lambda}{4F\delta}\right)^{1/2} \qquad \delta > \frac{r^2}{4R}$$

(B1.4,8)

A connection between the geometric and the modematched pictures can be made at this point. This may be deduced by considering the detuning from the confocal condition in the modematched picture which can be tolerated before the degeneracy is broken in the sense that the frequencies of two nearly degenerate modes are separated by the minimum resolved frequency $\Delta\nu$.

The resonant frequencies are

$$\Delta\nu_{q\ell m} = \frac{c}{2n(R+\delta)}\left[q + \frac{1}{\pi}(\ell+m+1)\left(\frac{\pi}{2} + \frac{\delta}{R}\right)\right]$$

(B1.4,9)

which may be written in the form

$$\Delta\nu_{q'\ell m} = \frac{c}{4n(R+\delta)}\left[q' + (\ell+m+1)\left(\frac{2\delta}{R\pi}\right)\right]$$

where $q' = 2q + (\ell+m+1)$ is an integer. The frequency difference caused by the transverse mode structure is

Appendix B.

Figure B.1.

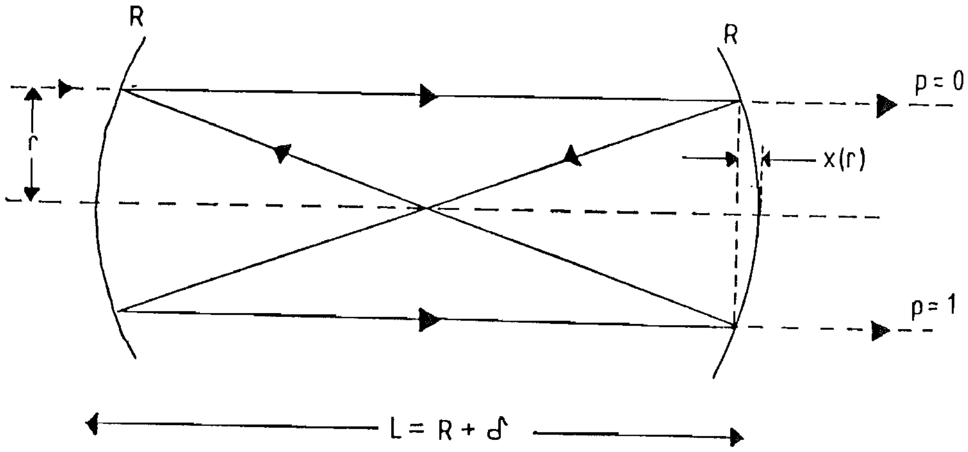

Figure B.1.

Notation for off-axis ray analysis in a slightly detuned confocal interferometer.

Figure B.2.

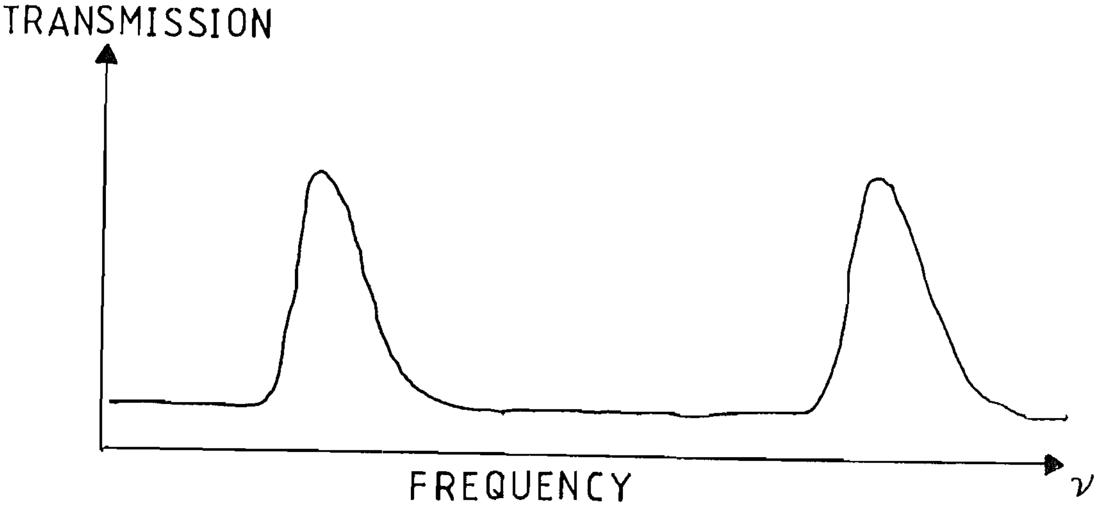

Figure B.2.

Transmission of a detuned confocal interferometer where

$$\delta > \frac{\pi R}{(\ell+m)2F}$$

$\nu_{q\ell m} - \nu_{q'00}$ and must be less than $\Delta\nu$

$$\frac{c}{4n(R+\delta)}\left[\frac{(\ell+m)2\delta}{\pi R}\right] < \frac{\nu_{FSR}}{F}$$

where $$\nu_{FSR} = \frac{c}{4(R+\delta)n}$$

so

$$\delta < \frac{\pi R}{2F(\ell+m)} \qquad \ell+m \neq 0$$

(B1.4,10)

Clearly for a modematched beam $\ell+m = 0$ and there is no limit to the detuning. This result indicates one method for obtaining the confocal condition by illuminating the interferometer with a large beam so that many transverse modes are excited. (B1.4,9) shows that if the resonator is longer than the confocal condition then the resulting transmission fringes will be broader on the high frequency side as illustrated in fig. B.2. By changing the cavity length so that the transmission fringes are symmetrical, the confocal condition may be achieved.

The spot size of a resonator of length $R+\delta$ in the electric field approach is approximately

$$w_0 = \left(\frac{(R+\delta)\lambda}{\pi}\right)^{\frac{1}{2}} \sim \left(\frac{R\lambda}{\pi}\right)^{\frac{1}{2}} \qquad \delta << R$$

By comparison with (B1.4,8) for $\sqrt{2}\, r_{max} \sim w_0$ it is necessary that $\frac{\delta F}{R\pi} \sim 1$. But from (B1.4,10) $(\ell+m)_{max} < \frac{\pi R}{\delta F}$ and the maximum number of transverse modes that may be excited is $(\ell+m) \leqslant 1$ for the detuning δ that corresponds to $\sqrt{2}\, r \sim w_0$. The factor of $\sqrt{2}$ relates the maximum radius of the intensity r_{max} to the maximum radius of the electric field. Clearly this picture should not be pressed too far. In particular the classical ray picture fails when diffraction effects are important.

B1.5. Phase shifts on reflection.

It is important to be able to determine whether the phase shift on reflection influences the resonator parameters. In the experiment described in this thesis a confocal resonator is used as a frequency marker. The free spectral range may be calculated using the following definition of the resonant frequency:

$$\nu_{q'} = \frac{c}{4Ln}\left[q' - \left(\frac{\phi_1+\phi_2}{2\pi}\right)\right] \tag{B1.5,1}$$

where $q' = 2q + (\ell+m+1)$.

Appendix B.

The free spectral range ν_{FSR} is defined as

$$\nu_{FSR} = \nu_{q'+1} - \nu_{q'}$$

and is

$$\nu_{FSR} = \frac{c}{4Ln}\left[1 + \frac{1}{2\pi}\left(\phi(q'+1) - \phi(q')\right)\right]$$

(B1.5,2)

where

$$\phi(q') = \phi_1(q') + \phi_2(q')$$

The free spectral range is frequency dependent through the phase shift term [10]. An estimate for the phase shift on reflection and the frequency dependence of the phase shift on reflection for aluminium coated mirrors may be found using data presented in [10]:

$$\phi_1(486\,\mathrm{nm}) = 15^\circ$$

$$\frac{d\phi_1}{d\lambda} = 0{\cdot}08^\circ\ \mathrm{nm}^{-1}$$

$$\frac{d\phi_1}{d\nu} = -\frac{\lambda}{\nu}\left(0{\cdot}08\times10^{9}\right)^\circ\ \mathrm{Hz}^{-1} \sim -6\times10^{-14}\ {}^\circ\ \mathrm{Hz}^{-1}$$

The magnitude of the correction for an interferometer with a 500 MHz free spectral range with aluminium mirrors operated near 486 nm is approximately $\frac{1}{\pi}\cdot\frac{d\phi}{d\nu}\cdot\nu_{FSR} \sim 10^{-5}$, and changes the F.S.R. from the value measured geometrically by 5 kHz. This is considerably smaller than the error in the length measurement (100 kHz) for the interferometer used in this experiment.

B1.6. Geometric phase shifts.

The geometric phase shift term which is

$$\frac{c}{2Ln}\left\{\frac{1}{\pi}(\ell+m+1)\cos^{-1}\sqrt{\left(1-\frac{L}{R_1}\right)\left(1-\frac{L}{R_2}\right)}\right\}$$

cancels out in calculating the free spectral range of the interferometer since it is frequency independent. This means that the usage of this interferometer solely as a frequency reference requires no information on the magnitude of the geometric phase shift correction or of the number of transverse modes excited, provided the transverse mode structure does not change during an experimental run. This change is only important when the maximum transverse mode order excited violates (B1.4,10) because in this case the interferometer fringes will be noticably asymmetric. If the shape changes during the scan then a change in transverse mode structure has occurred and the definition of the free spectral range (B1.5,2) is not independent of the mode structure.

B1.7. Interferometers used as filters.

It has been assumed that the proposed use of a confocal interferometer is to either analyse the frequency dependence of incoming light as a laser diagnostic tool, or to provide a frequency calibration for experimental purposes. It is also possible to use the light that has passed through the interferometer, as was done in this experiment, when the incoming light has too large a frequency bandwidth for the particular use in mind. The interferometer is being used as a frequency filter and the transmitted light acquires the frequency characteristics of the filter.

In the frequency domain the filtering action may be described by the transmission of the filter $g(\nu)$

$$g(\nu) = \frac{T^2}{(1-R)^2} \frac{1}{\left\{1 + \frac{4R}{(1-R)^2} \sin^2 \frac{\delta}{2}\right\}} \qquad (B1.7,1)$$

which is equivalent to (B1.2,4) for an interferometer with identical mirrors and

Appendix B.

$$\delta(\nu) = 2\pi \left\{ \frac{\nu_{q\ell m}}{\nu_{FSR}} - \frac{1}{\pi}(\ell+m+1)\cos^{-1}\left(1 - \frac{L}{R}\right) + \frac{\phi_1+\phi_2}{2\pi} \right\}$$

is the round trip phase change. Any input beam may be described by Fourier analysis as the sum of monochromatic beams with appropriate phases. If $h(\nu)$ is the frequency content of the incoming beams then the frequency content of the transmitted light is $h(\nu)\,g(\nu)$. The transmitted light will have the width

$$\frac{1}{\Delta\nu_T} = \sqrt{\frac{1}{(\Delta\nu_I)^2} + \frac{1}{(\Delta\nu_F)^2}}$$

assuming that the incoming light and the filter have spectral profiles which may be approximated by Gaussians of width $\Delta\nu_I$ and $\Delta\nu_F$ respectively.

A simple time domain analysis demonstrates intuitively how the filtering action applies to a pulsed input. Consider N_0 photons stored in a resonator of length L and mirror transmission $T = 1-R$. The number of photons lost in a time $\tau = \frac{L}{c}$ is

$$\frac{dN}{dt} = -\frac{(1-R)N}{L/c}$$

with solution $N = N_0 e^{-\frac{(1-R)ct}{L}}$. The transmitted photon number declines to $1/e$ of its original number in a time

$$\tau_F = \frac{L}{(1-R)c} = \frac{F}{2\pi\sqrt{R}\,\nu_{FSR}}$$

This is a measure of the reaction time of the cavity to an impulse. If the impulse is shorter than the cavity lifetime τ_F it is effectively stretched out to τ_F . Notice that τ_F is related to the cavity bandwidth $\Delta\nu = \frac{\nu_{FSR}}{F}$ implying the Fourier transform uncertainty relation

$$\Delta\nu\,\tau_L = \frac{1}{2\pi} \qquad \left(\sqrt{R} \sim 1\right) \tag{B1.7,2}$$

which is to be expected from the Fourier analysis of a single sided exponential. The reduction in bandwidth is achieved by averaging over a time corresponding to the cavity lifetime and thus reduces intensity fluctuations that occur on shorter time scales. This corresponds to a reduction in frequency bandwidth via the Fourier transform relation (B1.7,2).

Appendix B.

References.

[1] H. Kogelnik, T. Li. Applied Optics. 5 1550. (1966).

[2] M. Hercher. Applied Optics. 7 951. (1968).

[3] G.D. Boyd, H. Kogelnik. Bell Sys. Tech. J. 41 1347. (1962).

[4] D.J. Bradley, C.J. Mitchell. Phil. trans. Roy. Soc. A. 236 298. (1961).

[5] D.A. Jackson. Proc. Roy. Soc. A263 298. (1961).

[6] A. Yariv. "Introduction to Quantum Electronics". 2nd. ed. Wiley. (1976).

[7] E. Hecht, A. Zajac. "Optics". Addison-Wesley. (1979).

[8] L.G. Schulz. J.O.S.A. 44 357. (1954).

[9] C.J. Koester. J. Res. Nat. Bur. Stand. A64 191. (1960).

[10] J.M. Bennet. J.O.S.A. 54 612 (1964).

[11] M. Born, E. Wolf. "Principles of Optics". 6th. ed. Pergamon Press. (1980).

Appendix C.

Second Harmonic Generation in Urea and Lithium Formate Monohydrate.

The process of second harmonic generation using focussed Gaussian beams in anisotropic crystals is experimentally and theoretically well known [1,2,3,4]. This appendix outlines methods used to calculate the phasematching angles in uniaxial and biaxial crystals. Other factors which influence the doubling efficiency such as walk off angle and nonlinear coefficient are examined. Examples are given for the two nonlinear crystals used in this experiment.

C.1. Phasematching.

An electromagnetic wave propagating through a medium, which for the rest of this appendix will be assumed to be crystalline, induces a polarisation given by

$$P_i = \varepsilon_0 \left\{ \chi_{ij} E_j + d_{ijk} E_j E_k \right\} \qquad i,j,k \in x,y,z$$

This result is written in tensor form since the directions of the electric field components in an anisotropic media are important. The field and polarisation components E_i, P_i are referenced to the principle dielectric axis of the crystal x, y, z [5,6] the importance of which will be outlined later. This series has been truncated at the second term since only frequency doubling is of interest here. χ_{ij} is the linear dielectric tensor and d_{ijk} is the nonlinear coefficient. The nonlinear component oscillates as E^2 and so provides a D.C. term to the polarisation and, more importantly for this application, a term that oscillates at twice the frequency of the propagating electromagnetic wave. The nonlinear component can couple energy between the fundamental wave and the second harmonic. In order for efficient coupling to occur it is necessary that the fundamental and harmonic proqagate with the same phase velocity through the crystal so that the polarisations can add constructively. This is the reason why anisotropic crystals are used for frequency doubling, because for some directions of propagation it is possible to satisfy this phasematching requirement. As might be expected the phasematching direction is dependent on the wavelength. Also the form of the nonlinear dielectric tensor d_{ijk} may mean that phasematching is possible but the nonlinear component vanishes due to symmetry, so no coupling is possible for some propagation directions (see Section C.3).

The properties of the anisotropic crystals which permit phasematching will now be summarised:

(1). For any propagation direction in an isotropic crystal

Appendix C.

Figure C.1.

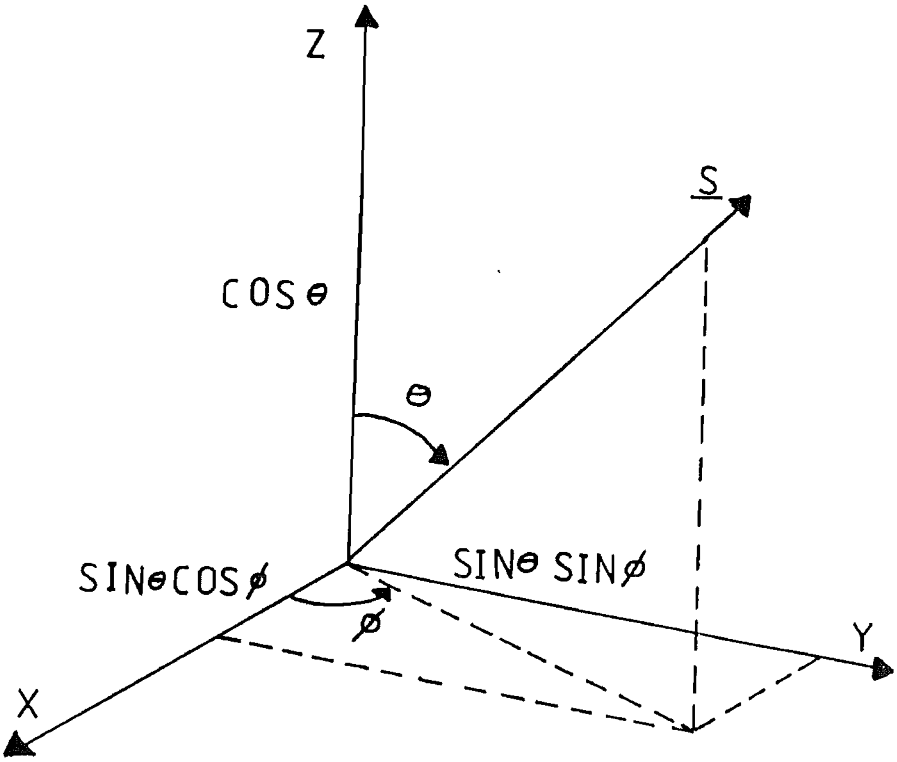

Figure C.1.

Spherical co-ordinate system used to relate the direction of propagation $\underline{S}$ to the principle dielectric axis.

there are two allowed linear polarisations which are orthogonal. The refractive index may be different for each polarisation. However, for uniaxial crystals there is one direction for which both refractive indices are equal, and for biaxial crystals there are two directions for which both refractive indices are equal. These directions are called the optic axis of the crystal.

(2). The refractive index for a given direction of propagation may be calculated using the principle dielectric axis which is a system for which the dielectric tensor ε_{ij} defined by

$$D_i = \varepsilon_0 \varepsilon_{ij} E_j \qquad i,j,k \in x,y,z$$

is diagonal so

$$D_i = \varepsilon_0 \varepsilon_{ii} E_i \qquad i \in x,y,z$$

The refractive index is $n_i = \sqrt{\varepsilon_{ii}}$. The solution of the Fresnel equation [5,6] for a direction of propagation $\underline{S}(S_x,$ $S_y, S_z)$

$$\frac{S_x^2}{\frac{1}{n^2} - \frac{1}{n_x^2}} + \frac{S_y^2}{\frac{1}{n^2} - \frac{1}{n_y^2}} + \frac{S_z^2}{\frac{1}{n^2} - \frac{1}{n_z^2}} = 0$$

(C1.0,1)

is [3]

$$\frac{2}{n_\pm^2} = \frac{1}{n_x^2}\left\{1 - S_x^2\right\} + \frac{1}{n_y^2}\left\{1 - S_y^2\right\} + \frac{1}{n_z^2}\left\{1 - S_z^2\right\}$$
$$\pm\sqrt{\left(\frac{1}{n_y^2}-\frac{1}{n_z^2}\right)^2\left\{1 - S_z^2\right\} + \left(\frac{1}{n_x^2}-\frac{1}{n_y^2}\right)^2\left\{1 - S_x^2\right\} - 2\left(\frac{1}{n_y^2}-\frac{1}{n_z^2}\right)\left(\frac{1}{n_x^2}-\frac{1}{n_y^2}\right)}$$

and

$$S_x = \sin\theta\cos\phi$$
$$S_y = \sin\theta\sin\phi$$
$$S_z = \cos\theta$$

$$S_x^2 + S_y^2 + S_z^2 = 1$$

where θ is the angle between the z-axis and the direction of propagation and ϕ is the angle between the projection of this direction onto the x-y plane and the x-axis as shown in fig C.1.

For uniaxial crystals where $n_y = n_x = n_o$ and $n_z = n_e$ (C1.0,1) gives

$$n_+ = n_o$$

$$\frac{1}{n_-^2} = \frac{\cos^2\theta}{n_o^2} + \frac{\sin^2\theta}{n_e^2}$$

(C1.0,2)

Thus for uniaxial crystals one of the allowed polarisations is always an ordinary polarisation with refractive index n_o. The direction of this polarisation n_o is easily found since it must lie in the x-y plane and also be orthogonal to $\underline{S}$. The other refractive index is intermediate between n_o and n_e and depends on the angle θ between $\underline{S}$ and the n_e

direction (the optic axis). The direction of this polarisation is easily found since it is orthogonal to the direction of propagation $\underset{\sim}{S}$ and to the other polarisation direction.

The directions of the polarisations in a biaxial crystal are less easily deduced without further analysis. Using the index ellipsoid [5,6] which is a surface defined by

$$\frac{x^2}{n_x^2} + \frac{y^2}{n_y^2} + \frac{z^2}{n_z^2} = 1$$

it is straightforward to show that the polarisation directions are given by the major and minor axis of the ellipse constructed by the intersection with the index ellipsoid of the plane passing through the origin which is normal to the propagation direction $\underset{\sim}{S}$. The lengths of the major and minor axis give the refractive indices of the two allowed polarisation directions. This ellipse is specified by points satisfying

$$x S_x + y S_y + z S_z = 0$$

$$\frac{x^2}{n_x^2} + \frac{y^2}{n_y^2} + \frac{z^2}{n_z^2} = 1$$

together with the condition that

$$n^2 = x^2 + y^2 + z^2$$

is an extremum, these values of n corresponding to the two allowed polarisations of propagation. Born and Wolf [5] show that x, y and z satisfy

$$x\left\{1 - \frac{n^2}{n_x^2}(1 - s_x^2)\right\} + n^2 s_x\left(\frac{y s_y}{n_y^2} + \frac{z s_z}{n_z^2}\right) = 0$$

together with two similar equations in y and z which enable x, y and z to be calculated for each value of n which can be found from (C1.0,1). The values of x, y and z give the spherical coordinates of the polarisation directions relative to the principle dielectric axis according to

$$\sin\theta' \cos\phi' = \frac{x}{n}$$
$$\sin\theta' \sin\phi' = \frac{y}{n}$$
$$\cos\theta' = \frac{z}{n}$$

(3). Frequency doubling can be viewed as the combination of two photons with wavevectors $\underline{k}_1$ and $\underline{k}_2$, and frequency ω to produce one photon with wavevector $\underline{k}_3$ and frequency 2ω. Energy and momentum conservation require

$$\underline{k}_3 = \underline{k}_1 + \underline{k}_2$$

$$\omega_3 = 2\omega$$

The momentum condition embodies the phasematching requirement that the polarisation component that oscillates at 2ω travels with the phase velocity of the second harmonic. This can be written as

$$\frac{2n_3}{\lambda_1} = \frac{n_1}{\lambda_1} + \frac{n_2}{\lambda_1}$$

where λ_1 is the vacuum wavelength of the fundamental. Thus the general phasematching condition for frequency doubling is found

Figure C.2.

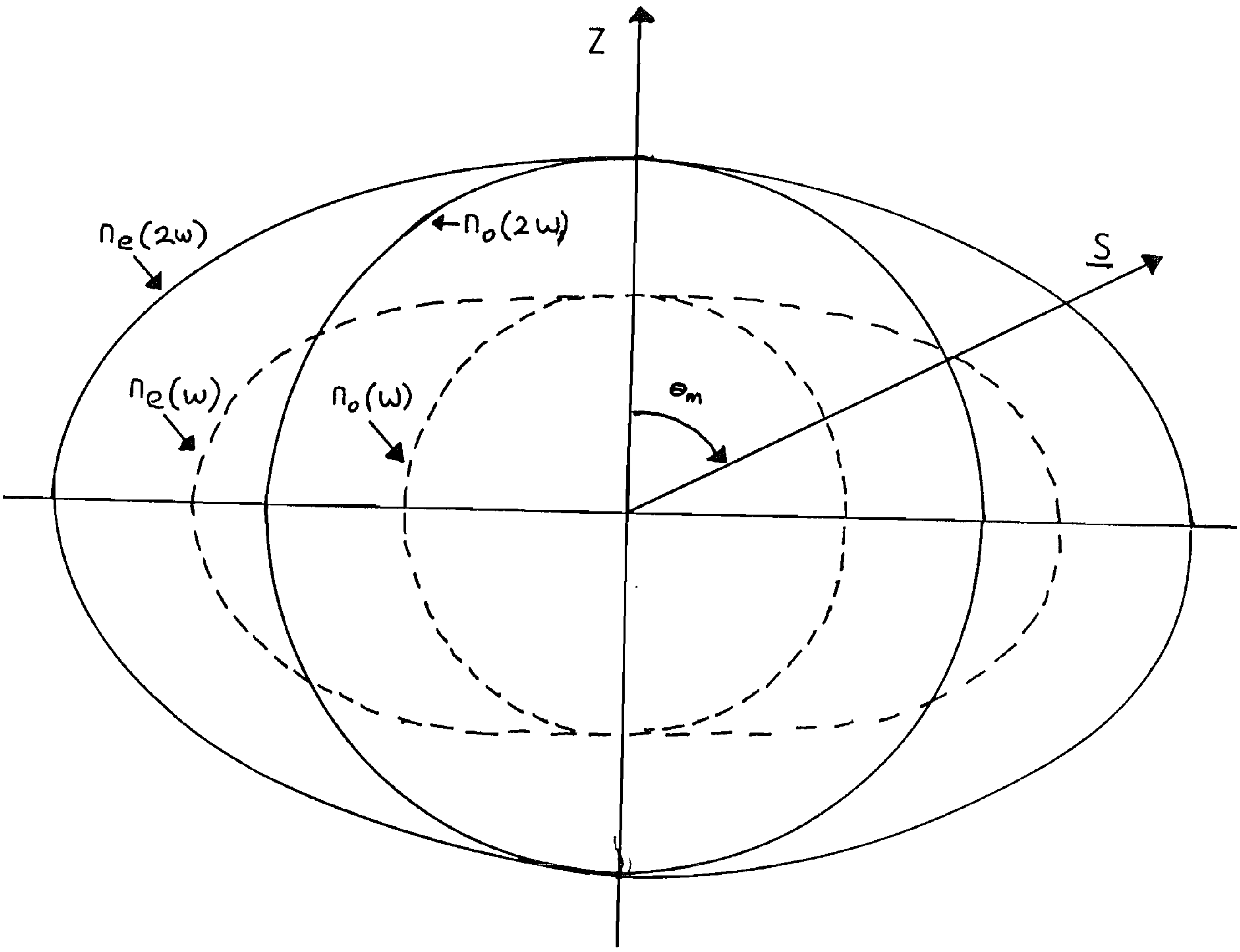

Figure C.2.

Normal surfaces showing the allowed refractive index as a function of direction for urea (which is a positive ($n_e > n_o$) uniaxial crystal).

Due to dispersion the refractive indices at 2ω are larger than at ω and if $n_o(2\omega) < n_e(\omega)$ then at some angle $\theta = \theta_m$ then $n_e(\omega, \theta_m) = n_o(2\omega)$, and the type I phasematching condition is satisfied. The dispersion and the extraordinary eccentricities have been exaggerated for clarity.

Figure C.3.

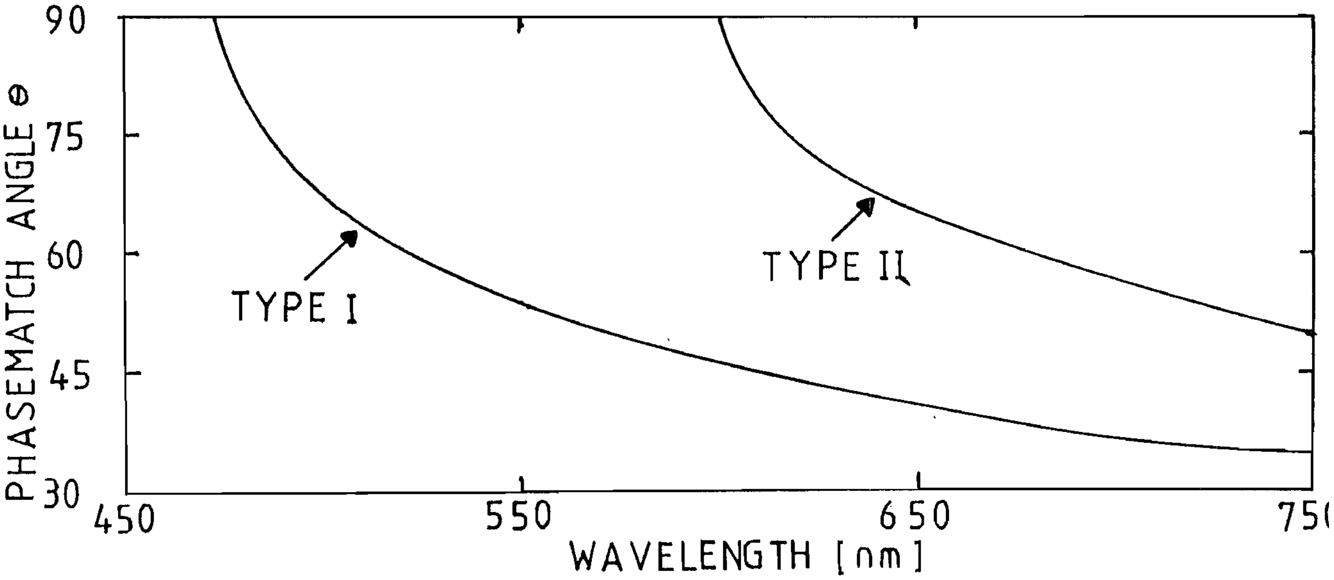

Figure C.3.

Type I and II phasematch angle in urea.

$$n_3 = \frac{1}{2}(n_1 + n_2)$$

(C1.0,3)

There are two possible refractive indices for the fundamental because of the two allowed polarisation modes. If only one polarisation of the fundamental is excited then the process is referred to as type I phasematching with the condition $n_3 = n_1$. Type II phasematching requires both polarisation modes to be excited and (C1.0,3) is the phasematching condition.

In most media the refractive index increases with frequency, a property known as normal dispersion. In some anisotropic media and over a restricted wavelength region it is possible to take advantage of the natural birefringence and normal dispersion and satisfy the phasematching conditions. Urea and lithium formate monohydrate will be used to demonstrate this for uniaxial and biaxial crystals respectively.

Urea [7,8,9,10] is a positive uniaxial crystal ($n_e > n_o$). The refractive index as a function of θ for two different wavelengths in a positive uniaxial crystal is drawn in fig. C.2. It is apparant that it is possible to select a direction specified by θ_m for which light propagating as an extra-ordinary ray has the same refractive index as its second harmonic propagating as an ordinary ray. The polarisation of the harmonic is orthogonal to its fundamental (type I phasematching). The type I and type II phasematching angle as a function of fundamental wavelengths are shown in fig.C.3. Note that the phasematching condition is independent of ϕ so that directions satisfying (C1.0,3) are rotationally symmetrical about the optic axis.

Lithium formate monohydrate is a biaxial crystal and both allowed refractive indices are in general dependent on direction. A simplification is possible when propagation direction lies in one of the principle planes. In this case the polarisation component normal to the plane has the value of refractive index of the principle dielectric axis parallel to it. The other refractive index is dependent on the direction in the plane. For example, propagation in the x-y plane ($\theta = \pi/2$) gives the following refractive indices (see C1.0,1)

$$n_+ = n_z$$

$$\frac{1}{n_-^2} = \frac{\sin^2\phi}{n_x^2} + \frac{\cos^2\phi}{n_y^2}$$

the phasematching problem is similar to urea. Moving off the principle axis planes the problem is more difficult, with both refractive indices dependent on direction. An example of the phasematching conditions in lithium formate is shown on a stereographic projection at $\lambda = 486$ nm in fig. C.4. The wavelength dependence of the θ phasematching angle for light propagating in the x-z plane ($\phi = 0$) is also shown in fig. C.5 for type I phasematching.

Figure C.4.

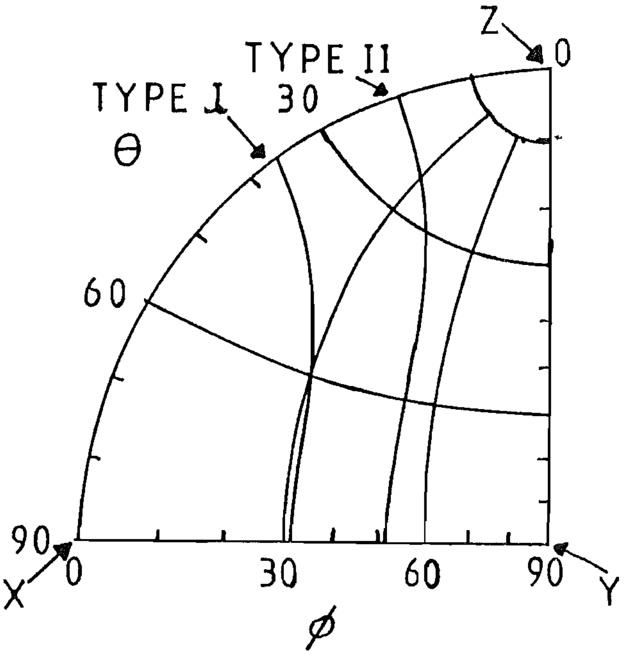

Figure C.4.

Stereographic plot of the type I and II phasematched directions in LFM at 486 nm.

Figure C.5.

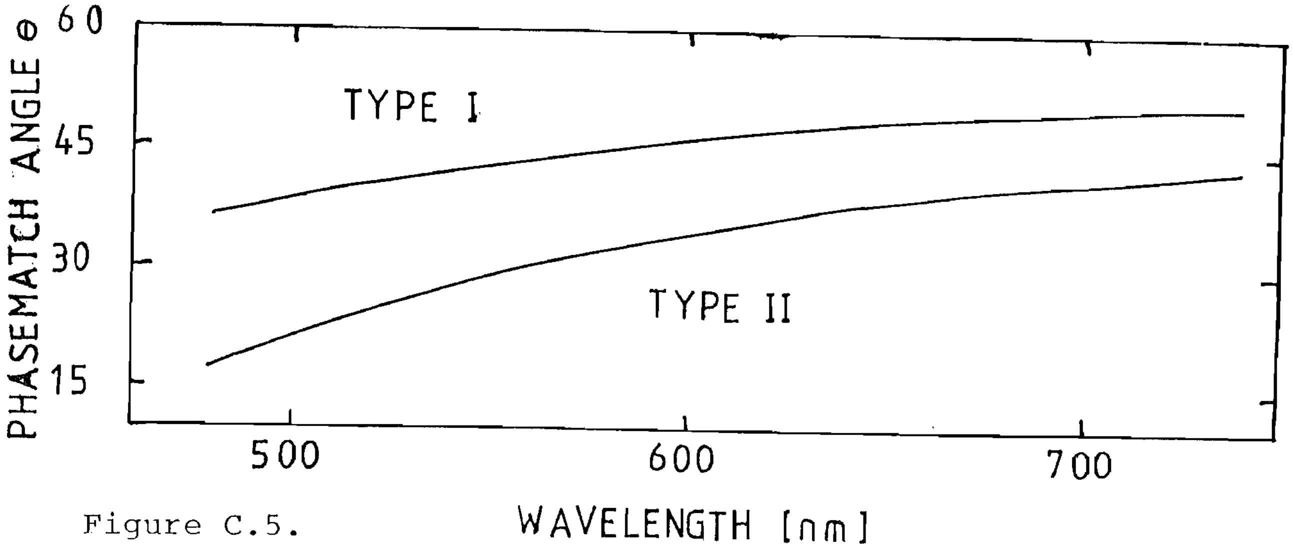

Figure C.5.

Phasematching in the x-z plane as a function of fundamental wavelength. Below 480 nm the use of lithium formate is prevented due to low damage thresholds caused by U.V. absorbtion bands.

C.2. Energy walk off.

In anisotropic media the energy flow is not necessarily in the propagation direction $\underline{S}(S_x, S_y, S_z)$. This is a consequence of the fact that $\underline{D}$ is not parallel to $\underline{E}$ and can be predicted from Maxwell's equations. The walk off angle is easily calculated using some results derived in Born and Wolf [5]. Born and Wolf derive the two equations

$$n_r = n \cos \rho$$

$$V_p^2 (V_r^2 - V_p^2) = \frac{1}{\frac{S_x^2}{(V_p^2 - V_x^2)^2} + \frac{S_y^2}{(V_p^2 - V_y^2)^2} + \frac{S_z^2}{(V_p^2 - V_z^2)^2}}$$

(C2.0,1)

where n is the refractive index for the polarisation and direction of propagation, and $V_p = \frac{c}{n}$ is the phase velocity. r is the ray refractive index and $V_r = \frac{c}{n_r}$ is the ray velocity and is equal to the energy crossing unit area in unit time divided by the stored energy per unit volume. Combining (C2.0,1), the walk off angle ρ is given by

$$\tan^2 \rho = \frac{n^4}{\frac{S_x^2}{\left(\frac{1}{n^2} - \frac{1}{n_x^2}\right)^2} + \frac{S_y^2}{\left(\frac{1}{n^2} - \frac{1}{n_y^2}\right)^2} + \frac{S_z^2}{\left(\frac{1}{n^2} - \frac{1}{n_z^2}\right)^2}}$$

(C2.0,2)

For a uniaxial crystal: $n_x = n_y = n_o$, $n_z = n_e$ (C.2,2) reduces to

$$\rho(n=n_o) = 0$$

$$\tan\rho = \frac{\pm(n_o^2-n_e^2)\sin\theta\cos\theta}{n_e^2\cos^2\theta + n_o^2\sin^2\theta} \qquad (C2.0,3)$$

The normal ray does not walk off whereas the extra-ordinary ray does. This is the origin of double refraction. The second equation of (C2.0,3) can be written in standard form as

$$\tan(\theta+\rho) = \frac{n_o^2}{n_e^2}\tan\theta \qquad (C2.0,4)$$

which is given in the literature [14]. In biaxial crystals both the extra-ordinary and ordinary rays walk off for propagation out of the planes containing the principle dielectric axis. Within the principle axis planes the walk off is similar to the uniaxial case. In the x-z plane the walk off angle is described by (C2.0,3) with the walk off for rays polarised normal to the x-z plane being zero and the walk off for the rays polarised in the x-z plane being given by

$$\tan(\theta+\rho) = \frac{n_x^2}{n_z^2}\tan\theta$$

C.3. The effective nonlinear coefficient.

The form of the nonlinear coefficient tensor depends on the crystal structure. For many media the crystal symmetry means many d_{ijk} are zero and others may be equal in magnitude. The nonlinear polarisation relative to the dielectric axis is

$$P_i^{NL} = \epsilon_0 d_{ijk} E_j E_k \qquad i, j, k \in x, y, z.$$

(Einstein summation convention)

Since there can be no physical significance in interchanging j and k, $d_{ijk} = d_{ikj}$ and the twenty seven components of d_{ijk} may be reduced to eighteen independent components often written as

$$\begin{bmatrix} d_{11} & d_{12} & d_{13} & d_{14} & d_{15} & d_{16} \\ d_{21} & d_{22} & d_{23} & d_{24} & d_{25} & d_{26} \\ d_{31} & d_{32} & d_{33} & d_{34} & d_{35} & d_{36} \end{bmatrix}$$

and the associated column vector $E_i E_j$ is

$$\begin{bmatrix} E_1^2 \\ E_2^2 \\ E_3^2 \\ 2E_2E_3 \\ 2E_1E_3 \\ 2E_1E_2 \end{bmatrix}$$

The Kleinman condition [15] states that if the three interacting frequencies $\omega_1, \omega_2, \omega_3$ are on the same side of

Figure C.6.

(a). Urea.

$$\begin{bmatrix} 0 & 0 & 0 & d_{14} & 0 & 0 \\ 0 & 0 & 0 & 0 & d_{14} & 0 \\ 0 & 0 & 0 & 0 & 0 & d_{14} \end{bmatrix}$$

$d_{14} = 1.4 \pm 0.1\ 10^{-12}$ m/v [8].

(b). Lithium formate monohydrate.

$$\begin{bmatrix} 0 & 0 & 0 & 0 & d_{31} & 0 \\ 0 & 0 & 0 & d_{32} & 0 & 0 \\ d_{31} & d_{32} & d_{33} & 0 & 0 & 0 \end{bmatrix}$$

$d_{31} = 0.11 \pm 0.02 \times 10^{-12}$ m/v [16]

$d_{32} = 1.27 \pm 0.09 \times 10^{-12}$ m/v

$d_{33} = 1.86 \pm 0.11 \times 10^{-12}$ m/v

Figure C.6.

Forms of the nonlinear tensor d_{ijk} for urea and lithium formate.

Where the coefficients are equal eg. $d_{14} = d_{25}$ only one of them is mentioned by name, in this case d_{14}.

the electronic resonances then all the indices of d_{ijk} may be permuted at will so $d_{ijk} = d_{ikj} = d_{kij}$ etc. This leaves only ten independent coefficients. The form and values of the d_{ijk} are shown in fig. C.6 for lithium formate monohydrate and urea.

The object is to calculate the effective nonlinear coefficient d_{eff} which for type I frequency doubling is the component of the polarisation in the harmonic polarisation direction due to the fundamental [17]. Formally the solution is found by calculating the fundamental field $E(\omega)$ in terms of the principle dielectric axis so

$$E_i = a_i E(\omega) \qquad i \in x, y, z.$$

where a_i is the appropriate direction cosine to be calculated later [3]. The induced polarisation is

$$P_i = \varepsilon_0 d_{ijk} a_j a_k E^2(\omega)$$

Finally the induced polarisation in the harmonic direction may be calculated from the P_i :

$$P_{2\omega} = \beta_i P_i = \varepsilon_0 E^2(\omega) \{ \beta_i d_{ijk} a_j a_k \}$$

β_i are the direction cosines appropriate to the harmonic polarisation direction. Again the right hand side is to be summed over all possible i,j,k combinations. The quantity in

$\{\}$ is referred to as the effective nonlinear coefficient. For type II doubling it is easy to show d_{eff}^{II} is given by

$$d_{eff}^{II} = \beta_i d_{ijk} \beta_j \alpha_j = \beta_i d_{ijk} \alpha_j \beta_k$$

The analysis which gives the direction cosines α_i, β_i is of interest since it provides an alternative derivation of the two refractive indices for a direction $\underline{S}(S_x, S_y, S_z)$. These are given by the lengths of the major and minor axis of the ellipse defined by the intersection of the plane which passes through the origin normal to S with the index ellipsiod:

$$\frac{x^2}{n_x^2} + \frac{y^2}{n_y^2} + \frac{z^2}{n_z^2} = 1 \qquad \text{(C3.0,1)}$$

(see Section C.1). In matrix form (C3.0,1) is represented by

$$X^T H X = 1$$

where

$$X = \begin{pmatrix} x \\ y \\ z \end{pmatrix} \qquad X^T = (x, y, z) \qquad H = \begin{bmatrix} \frac{1}{n_x^2} & 0 & 0 \\ 0 & \frac{1}{n_y^2} & 0 \\ 0 & 0 & \frac{1}{n_z^2} \end{bmatrix}$$

The convention $n_x < n_y < n_z$ is assumed. A new axis system is chosen x', y', z' where z' is parallel to $\underline{S}$ and x' and y' are the minor and major axis of the ellipse respectively. The values of x' and y' give the refractive

Appendix C.

Figure C7.

(a). Rotation by an angle ϕ about z .

$$\begin{bmatrix} \cos\phi & \sin\phi & 0 \\ -\sin\phi & \cos\phi & 0 \\ 0 & 0 & 1 \end{bmatrix}$$

(b). Rotation by an angle θ about the new y axis.

$$\begin{bmatrix} \cos\theta & 0 & -\sin\theta \\ 0 & 1 & 0 \\ \sin\theta & 0 & \cos\theta \end{bmatrix}$$

(c). Rotation by an angle ψ about $\underline{S}$.

$$\begin{bmatrix} \cos\psi & -\sin\psi & 0 \\ \sin\psi & \cos\psi & 0 \\ 0 & 0 & 1 \end{bmatrix}$$

Figure C7.

Rotations used to diagonalise T which is defined in the text prior to (C3.03).

indices of the allowed polarisations. The new frame of reference is obtained by the following series of rotations with matrices given in fig. C.7

(a). Rotate by an angle ϕ about $\mathbf{z}$.

(b). Rotate by an angle θ about the new y axis.

(c). Rotate by an angle ψ about $\underline{S}$.

This composite is represented by the matrix

$$M = \begin{bmatrix} \cos\theta\cos\phi\cos\psi + \sin\phi\sin\psi & \cos\theta\sin\phi\cos\psi - \cos\phi\sin\psi & -\sin\theta\cos\psi \\ \cos\theta\sin\psi\cos\phi - \sin\phi\cos\psi & \cos\phi\cos\psi + \cos\theta\sin\psi\sin\phi & -\sin\theta\sin\psi \\ \cos\phi\sin\theta & \sin\theta\sin\phi & \cos\theta \end{bmatrix}$$

This rotation transforms the vectors X into W :

$$W = MX$$

and the equation of the ellipse is

$$W^T (M^{-1})^T H (M^{-1}) W = 1$$

where the only parts of interest of the matrix $T = MHM^{-1}$ are the components T_{11} , T_{12} , T_{21} and T_{22} . The reason for this is that the ellipse is in the plane $x'y'$ so $z' = 0$.

The angle ψ is chosen so that x' lies along the minor axis of the ellipse, while y' lies along the major axis. This ensures that $n_x' < n_y'$ in agreement with the chosen convention. Set $\psi = 0$ in M and the matrix $T(\psi = 0)$ is

$$T(\psi=0) = \begin{bmatrix} \frac{\cos^2\theta\cos^2\phi}{n_x^2} + \frac{\cos^2\theta\sin^2\phi}{n_y^2} + \frac{\sin^2\theta}{n_z^2} & \cos\theta\sin\phi\cos\phi\left[\frac{1}{n_y^2} - \frac{1}{n_x^2}\right] & X \\ \cos\theta\sin\phi\cos\phi\left[\frac{1}{n_y^2} - \frac{1}{n_x^2}\right] & \frac{\sin^2\phi}{n_x^2} + \frac{\cos^2\phi}{n_y^2} & X \\ X & X & X \end{bmatrix}$$

$$= \begin{bmatrix} A & B & C \\ D & E & F \\ G & H & I \end{bmatrix}$$

where X = don't care. Applying the rotation about ψ gives

$$\begin{bmatrix} A\cos^2\psi + E\sin^2\psi - (B+D)\sin\psi\cos\psi & B\cos^2\psi - D\sin^2\psi + (A-E)\sin\psi\cos\psi & X \\ D\cos^2\psi - B\sin^2\psi + (A-E)\sin^2\psi & A\sin^2\psi + E\cos^2\psi + (B+D)\cos\psi\sin\psi & X \\ X & X & X \end{bmatrix}$$

Since $B = D$ this is a symmetric matrix.

It is straightforward to show that the values of ψ for which the off diagonal elements of $T(\psi)$ vanish are given by

$$\tan 2\psi = \frac{2B}{E-A} = \frac{\cos\theta \sin 2\theta \left[\frac{1}{n_y^2} - \frac{1}{n_x^2}\right]}{\left\{\frac{1}{n_y^2} - \frac{1}{n_x^2}\right\}(\cos^2\theta\cos^2\phi - \sin^2\phi) - \left\{\frac{1}{n_z^2} - \frac{1}{n_y^2}\right\}\sin^2\theta} \qquad (C3.0,2)$$

If ψ is a solution of (C3.0,2) then $\psi + 90^\circ$ is also a solution. The diagonal elements of $\mathcal{T}$ give the allowed refractive indices:

$$\frac{1}{n_{x'}^2} = A\cos^2\psi + E\sin^2\psi + 2B\cos\psi\sin\psi$$

$$\frac{1}{n_{y'}^2} = A\sin^2\psi + E\cos^2\psi - 2B\cos\psi\sin\psi$$

(C3.0,3)

Using (C1.0,1) the solutions may be written as

$$\frac{2}{n_{x'}^2} = \alpha + \beta \qquad \frac{2}{n_{y'}^2} = \alpha - \beta$$

It is a simple matter to show

$$\alpha = A + E \qquad \beta = \sqrt{(E-A)^2 + (2B)^2}$$

where (C3.0,2) has been used. Substitution for A, E and B from $\mathcal{T}(\psi=0)$ demonstrates that (C3.0,3) indeed gives the correct refractive indices for a direction of propagation $\underline{S}$.

The object of this analysis is to provide the direction cosines $\alpha_i \beta_i$, which are obtained from the matrix $\mathcal{M}$. Given an electric field propagating with a y'

polarisation,

$$W = \begin{pmatrix} 1 \\ 0 \\ 0 \end{pmatrix} \qquad X = (m^{-1})W = \begin{pmatrix} \cos\theta\cos\phi\cos\psi + \sin\phi\sin\psi \\ \cos\theta\sin\phi\cos\psi - \cos\phi\sin\psi \\ -\sin\theta\cos\psi \end{pmatrix} = (\alpha_i)$$

is the direction cosine for the larger refractive index. Also

$$(\beta_i) = \begin{pmatrix} \cos\theta\sin\psi\cos\phi - \sin\phi\cos\psi \\ \cos\phi\cos\psi + \cos\theta\sin\psi\sin\phi \\ \sin\theta\sin\phi \end{pmatrix}$$

gives the direction cosines for light polarised in the x' direction. (smaller refractive index).

In the case of urea which is a positive uniaxial crystal, $n_e > n_o$ and $n_x = n_y = n_o$, $n_z = n_e$ so (C3.0,2) gives $\tan\psi = 0$, $\psi = 0°$ or $90°$. In this case ψ is chosen so that the smaller of the two solutions for the refractive index is independent of angle. Thus $\psi = 90°$ and

$$(\alpha_i) = \begin{pmatrix} \cos\theta\cos\phi \\ \cos\theta\sin\phi \\ -\sin\theta \end{pmatrix} \qquad (\beta_i) = \begin{pmatrix} -\sin\phi \\ \cos\phi \\ 0 \end{pmatrix}$$

The only nonvanishing component of the nonlinear tensor is the $d_{14} = d_{25} = d_{36}$ component. For a fundamental beam propagating as an extra-ordinary ray $E_{y'}$, the electric fields in terms of the principle dielectric axis are

$$E_x = E_{y'} \cos\theta \cos\phi$$

$$E_y = E_{y'} \cos\theta \sin\phi$$

$$E_z = -E_{y'} \sin\theta$$

and the polarisations are

$$P_x = -d_{14} \sin 2\theta \sin\phi \, (E_{y'})^2$$

$$P_y = -d_{14} \sin 2\theta \cos\phi \, (E_{y'})^2$$

$$P_z = d_{14} \cos^2\theta \sin^2\phi \, (E_{y'})^2$$

And the polarisation in the x' direction is

$$P_{eff} = d_{14} \sin 2\theta (\sin^2\phi - \cos^2\phi)(E_{y'})^2 = -d_{14} \sin 2\theta \cos 2\theta (E_{y'})^2$$

so the effective nonlinear component for type I doubling is $d_{eff} = d_{14} \sin 2\theta \cos 2\phi$. Remembering that for uniaxial crystals the phasematch condition is independent of ϕ the optimum direction is given by $\phi = 0$.

For completeness, the effective nonlinear coefficient for type I doubling in a negative uniaxial crystal is found by setting $\Psi = 0$ in the above analysis and is

$$d_{eff} = d_{14} \sin\theta \sin 2\phi$$

The effective nonlinear coefficient for lithium formate monohydrate is more complex since the angle Ψ does not necessarily take on simple values as it did for urea. The complete form for the nonlinear coefficient is given in

[4]. In the x-z plane $\phi = 0^\circ$ so $\psi = 0^\circ, 90^\circ$. The fundamental propagates as an ordinary ray so the refractive index that is independent of angle is n_y. From (C3.0,3) it may be found that $\psi = 0$. The direction cosines are

$$(\beta_i) = \begin{pmatrix} \cos\theta \\ 0 \\ -\sin\theta \end{pmatrix} \qquad (\alpha_i) = \begin{pmatrix} 0 \\ 1 \\ 0 \end{pmatrix}$$

and

$$d_{eff} = d_{32} \sin\theta.$$

Propagation in the x-y plane gives $\psi = 0^\circ, 90^\circ$ again and direction cosines become with $\psi = 90^\circ$:

$$(\beta_i) = \begin{pmatrix} -\sin\phi \\ \cos\phi \\ 0 \end{pmatrix} \qquad (\alpha_i) = \begin{pmatrix} 0 \\ 0 \\ 1 \end{pmatrix}$$

The polarisation due to the fundamental is in the z direction. However, the nonlinear tensor indicates that the induced polarisation is also in the z direction; thus the component in the x-y plane is zero and the nonlinear coefficient vanishes.

C.4. Frequency doubling.

So far the properties of the crystals which enable efficient frequency doubling to occur have been discussed.

Appendix C.

This section outlines the Boyd and Kleinman [1] theory of frequency doubling using focussed Gaussian beams, which enables the efficiency of the conversion process to be calculated. Also a figure of merit is defined for nonlinear crystals, which includes the influence of energy walk off and the effective nonlinear coefficient thus enabling different crystals to be compared.

Boyd and Kleinman show that the second harmonic power $P_{2\omega}$ generated in a positive or negative uniaxial crystal is given by

$$P_{2\omega} = K L k_1 e^{-\alpha' L} h(\sigma, \beta, \kappa, \xi, \mu) P_\omega^2 \qquad (C4.0,1)$$

which shows the characteristic quadratic dependence of the generated second harmonic power on the fundamental power. The fundamental beam is assumed to be Gaussian with a confocal parameter in the crystal given by

$$b = \omega_0^2 k_1 = \frac{2\pi \omega_0^2 n_1}{\lambda_1}$$

where λ_1 is the vacuum wavelength of the fundamental, n_1 is its refractive index within the media, ω_0 is the $1/e$ radius of the electric field beam waist and $k_1 = 2\pi n_1/\lambda_1$ is the wavevector within the media. The second harmonic beam shape will not in general be Gaussian since the energy walk off distorts the beam shape. The proportionality constant K in S.I. units is [18]

Appendix C.

$$K = \frac{2\,\omega_1^2\, d_{eff}^2}{\pi \varepsilon_0 c^3 n_1^2 n_2}$$

The second harmonic power is quadratically dependent on the nonlinear coefficient d_{eff} defined in C.3. n_2 is the refractive index of the second harmonic beam. Normally $n_1 = n_2$ under properly phasematched conditions. The differential absorbtion per unit length α' is

$$\alpha' = \alpha_1 + \frac{1}{2}\alpha_2$$

where α_1 is the absorbtion of the fundamental and α_2 the absortion of the harmonic. L is the crystal length. The dependence of the second harmonic process on focussing, phasematching and walk off is contained within $h(\sigma, \beta, \kappa, \xi, \mu)$ which is a numerically evaluated function. The parameters $\sigma, \beta, \kappa, \xi, \mu$ are given by

$$\sigma = \frac{1}{2} b \Delta k \qquad \Delta k = k_2 - 2k_1$$

$$\xi = \frac{L}{b}$$

$$\mu = \left[\frac{L - 2f}{L}\right]$$

$$B = \frac{\beta}{\xi^{1/2}} = \frac{\rho}{2}\left(L k_1\right)^{1/2}$$

$$\kappa = \frac{1}{2} \alpha b$$

Normally the losses may be neglected so $\kappa = 0$. The optimum doubling efficiency occurs when the fundamental is focussed at the crystal centre $\mu = 0$. The phasematching parameter σ

is generally optimised experimentally so, as shown in Boyd and Kleinman, the important function is $h_m(\beta, \xi)$ where the subscript m indicates that the phasematching has been optimised. The value of $h_m(\beta,\xi)$ drops off rapidly for values of the walk off parameter much greater than 1. Also the value of the function is rather insensitive to the focussing parameter for the typical range $1<\xi<6$. The optimum value of ξ lies in the range 2.84 (for $\beta=0$) to 1.39 (for $\beta>6$). The maximum value of $h_m(\beta,\xi)$ is 1.068.

A figure of merit which depends solely on the material parameters for doubling a particular wavelength is given by

$$\frac{d_{eff}^2}{n_1^2 n_2} h_{mm}(\beta)$$

where $h_{mm}(\beta)$ is also defined by Boyd and Kleinman and is the function $h_m(\beta,\xi)$ evaluated using the optimum focussing parameter. The ratio of this figure of merit gives the relative quantity of harmonic generation at a particular wavelength. For urea, lithium formate monohydrate and potassium pentaborate [18] the ratios are given by 1400 : 340 : 1 respectively. The relevant quantities are summarised in Table C.1.

The reason that urea is more efficient than lithium formate monohydrate is solely due to the large walk off experienced by the harmonic. The effective nonlinear coefficients are roughly of the same size. Potassium pentaborate is a nonlinear crystal often used to generate U.V. in the 217-250 nm region. However, its nonlinear coefficient is rather small and this is the reason it is so inefficient in comparison with urea and lithium formate monohydrate. It remains the only crystal at present available for frequency doubling light to the region 238-217 nm, 238 nm is the 90° phasematch angle for urea but its non linear coefficient vanishes at this point. Lithium formate monohydrate is phasematcheable to below 480 nm but is limited to harmonic wavelengths greater than 240 nm due to U.V. absorbtion induced damage to the crystal.

Appendix C.

Table C.1. Properties of urea, LFM and KPB at 486 nm.

	Urea	LFM	KPB	Units
phasematch	74.1°	36.8°	57.3°	degrees
energy walk off	0.0382	0.137	0.0339	radians
refractive index	1.5907	1.4876	1.4758	
effective non linear coefficient	7.4×10^{-13}	7.6×10^{-13}	1.7×10^{-14}	m/v
proportionality constant	5.45×10^{-9}	7.0×10^{-9}	3.1×10^{-12}	w^{-1}
walk off parameter $B^{(1)}$	8.66	30.0	7.4	
$h_{mm}(B)$	0.08	0.015	0.1	
figure of merit	1.3×10^{-26}	0.26×10^{-26}	7.6×10^{-30}	$m^2\,v^{-2}$

(1) Assuming a crystal length l=0.01 m.

References.

[1] G.D. Boyd, D.A.Kleinman. J. Appl. Phys. 39 3597. (1968).

[2] M.V. Hobden. J. Appl. Phys. 38 4365. (1967).

[3] W.P. Mason. Bell Sys. Tech. J. 29 161. (1950).

[4] H. Ito, H. Naito, H. Inaba. J. Appl. Phys. 46 3992. (1975).

[5] M. Born, E. Wolf. "Principles of Optics". 6th ed. Pergamon. (1980).

[6] A. Yariv. "Introduction to Quantum Electronics" 2nd. ed. Wiley. (1976).

[7] C. Cassidy, J.M. Halbout, W. Donaldson, C.L. Tang. Opt. Comm. 29 243. (1979).

[8] J.M. Halbout, S. Blit, W. Donaldson, C.L. Tang. IEEE J. Quant. Elect. QE-15 1176. (1979).

[9] K. Kato. IEEE J. Quant. Elect. QE-16 810. (1980).

[10] W. Donaldson, C.L. Tang. Appl. Phys. Lett. 44 25. (1984).

[11] F.B. Dunning, F.K. Tiltel, R.F. Stubbings. Opt. Comm. 7 181. (1972).

[12] C. Gabel, M. Hercher. IEEE J. Quant. Elect.(1972).

[13] H. Naito, H. Inaba. Opto-electronics. 5 256. (1973).

[14] T.J. Nelson. Bell Syst. Tech. J. 43 821. (1964).

[15] D.A. Kleinman. Phys. Rev. 126 1977. (1962).

[16] S. Singh, W.A. Bonner, J.R. Potopowics, L.G. Van

Vitert. Appl. Phys. Lett. 17 292. (1970).

[17] J.E. Midwinter, J. Warner. Brit. J. Appl. Phys. 16 1135. (1963).

[18] S. Singh. "Handbook of Lasers". C.R.C. Press. (1971).

[19] C.F. Dewey, W.R. Cook, R.T. Hodgeson, J.J. Wynne. Appl. Phys. Lett. 26 714. (1975).

Appendix D. Relevant publications.

Copies of the two papers published during the course of this work are included here. The refences are:

J.R.M. Barr, J.M. Girkin, A.I. Ferguson, G.P. Barwood, P. Gill, W.R.C. Rowley, R.C. Thompson. Opt. Comm. 54 217. (1985).

J.R.M. Barr, J.M. Girkin, J.M. Tolchard, A.I. Ferguson. Phys. Rev. Lett. 56 580. (1986).

Appendix D.

Volume 54, number 4 OPTICS COMMUNICATIONS 15 June 1985

INTERFEROMETRIC FREQUENCY MEASUREMENTS OF $^{130}Te_2$ TRANSITIONS AT 486 nm

J.R.M. BARR, J.M. GIRKIN, A.I. FERGUSON
Physics Department, The University, Southampton, UK

G.P. BARWOOD, P. GILL, W.R.C. ROWLEY and R.C. THOMPSON
National Physical Laboratory, Teddington, Middlesex, UK

Received 18 February 1985

Doppler-free spectra of $^{130}Te_2$ have been investigated in the region of 486 nm, close to the Balmer-β transitions in atomic hydrogen and deuterium. The frequency ratios between a 633 nm He-Ne laser stabilized to the 11-5 R(127) "i" transition in $^{127}I_2$ and two of these $^{130}Te_2$ Doppler-free components have been measured interferometrically to a precision of 2 parts in 10^{10} (one standard deviation). These measured components constitute useful transfer standards for the measurement of absolute frequencies of both the Balmer-β transitions and the 243-nm two-photon 1S 2S transitions in hydrogen and deuterium.

1. Introduction

There has been considerable effort in recent years to observe the two-photon 1S–2S transition in atomic hydrogen. The narrow linewidth of this transition offers potential for high accuracy verification of atomic structure theory. Early work at Stanford [1,2] compared the ($1S_{1/2}-2S_{1/2}$) and Balmer-β transitions. This made possible measurements of the ground-state Lamb shift and the hydrogen-deuterium isotope shift. To our knowledge an accurate measurement of the absolute frequencies of these transitions using Doppler-free laser techniques has not been reported. Such a measurement would enable the Rydberg constant to be determined to a precision better than that previously achieved with the Balmer-α transition [3–6]. As a step towards this goal we have undertaken the frequency measurement of two Doppler-free transitions in $^{130}Te_2$. These transitions lie close to Balmer-β and within a few GHz of the frequencies corresponding to a quarter of the (1S 2S) transition energies in hydrogen and deuterium. The tellurium, contained within a cell, is easily transportable for use as a frequency transfer standard.

2. Doppler-free $^{130}Te_2$ spectra

The Doppler-limited tellurium absorption spectrum between 420 nm and 540 nm has previously been published [7]. Laser-induced fluorescence in tellurium has also been reported at 514 nm and 488 nm [8]. More recently saturated tellurium spectra at 486 nm have been reported [9]. The Doppler-free $^{130}Te_2$ spectra reported here were obtained using the saturated absorption configuration shown in fig. 1. The cw laser used was a Coumarin 102 standing-wave dye laser (Coherent 599-21) pumped by 2.5 W of violet light from a krypton ion laser. With fresh dye this provided ~50 mW of single mode dye laser output at 486 nm. The saturation arrangement was optically isolated using a 40 MHz acousto-optic modulator in order to prevent feedback to the dye laser.

Tellurium of 99.3% isotopic purity was contained in an evacuated fused silica cell (65 mm long X 25 mm diameter) with normal incidence windows [10]. The cell had been baked to 1100°C and evacuated to 10^{-5} Pa prior to filling. No detailed information regarding the level of contaminants within the cell following the filling and sealing, or during any subse-

0 030-4018/85/$03.30 © Elsevier Science Publishers B.V.
(North-Holland Physics Publishing Division)

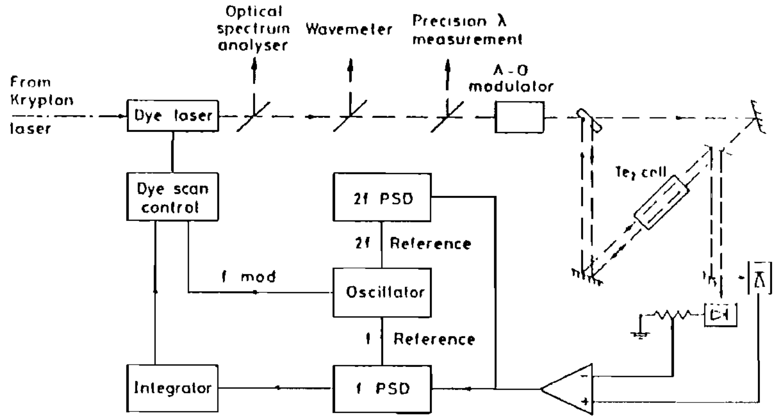

Fig. 1. Experimental arrangement for dye laser stabilization to saturated spectra in tellurium.

quent heating, was available. The cell wall was heated to 643°C via a 10 Ω nichrome heater wire which was non-inductively wound. The temperature was monitored by a cold junction compensated chromel/alumel thermocouple fixed to the thermally insulated outer wall of the cell body. It was presumed that the tellurium equilibrium vapour pressure in the cell was determined by the temperature of the cell windows, since these were not lagged, and there was no "cold finger" side-arm. This premise was in agreement with the observation of tellurium condensate there. An estimate of the differential between the monitored wall temperature and that at the windows was made by observing the known tellurium melting point and assuming a proportional variation of this differential with respect to the measured temperature above ambient. This differential was thus estimated to be −18°C at normal operating temperatures, with an estimated standard deviation of 6°C.

The saturated tellurium spectra in the vicinity of the deuterium and hydrogen transitions are shown in fig. 2. These were produced by overlapping a 6 mW chopped saturating beam with a 0.4 mW probe beam counter-propagating through the cell. The beams were focused to waists outside the cell, and the saturating and probe beam radii (1/e amplitude point) in the cell ranged from 0.28 mm to 0.24 mm, and 0.20 mm to 0.13 mm respectively. An identical but displaced second probe beam was used to subtract off the laser in-

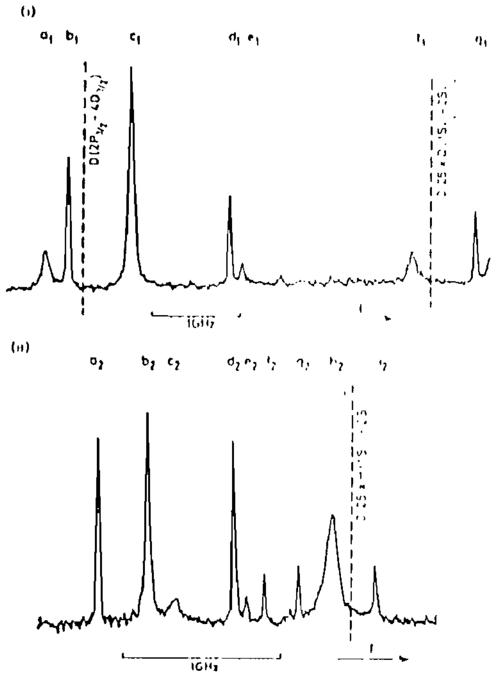

Fig. 2. Doppler-free spectra in $^{130}Te_2$ at 486 nm close to the frequency equal to a quarter of the $(1S_{1/2}-2S_{1/2})$ transition frequency in (i) deuterium and in (ii) hydrogen. The indicated frequency relevant to the hydrogen transition is the hyperfine centroid value.

Appendix D.

tensity noise and linear absorption background from the detected probe signal. The Doppler-free spectra were then recovered using standard lock-in techniques. The probe beams were slightly smaller than the saturating beam. This was necessary due to convection-induced probe beam wander relative to the saturating beam, which otherwise resulted in a variation of the saturated signal amplitude. The frequency scales for the spectral scans of fig. 2 were determined using a confocal interferometer of 75 MHz free spectral range.

Careful consideration was given to the choice of which tellurium saturated components should be used for the frequency ratio measurements. Use of saturated features with the narrowest linewidths should optimize the short-term stability of a tellurium-stabilized dye laser. The spectra of fig. 2 exhibited linewidths (fwhm) in the range 20 -100 MHz. By comparison linewidths of 1–5 MHz are typical for saturated absorptions in iodine [11]. Further, good long-term reproducibility is required. As a result, some of the observed features in fig. 2 were deemed to be unsuitable due to unexpected temperature behaviour (e.g. fig. 2, component labelled h_2) or to magnetic field dependence. In this latter case, an inductive heater winding used in a preliminary study resulted in an axial field induced 100 Hz modulation to the a_2 and d_2 features. These were thus discounted, although the heater was subsequently wound non-inductively. The components chosen were b_1 and b_2 (fig. 2) which lie roughly 4.2 GHz and 1.3 GHz respectively below the frequencies equal to a quarter of the deuterium and hydrogen (1S–2S) transitions. The fwhm linewidths were measured to be 20 MHz and 34 MHz (±10%) for components b_1 and b_2 respectively.

3. $^{130}Te_2$-stabilized dye laser operation

During the frequency ratio measurements, the dye laser light at 486 nm was stabilized to the appropriate tellurium components. The laser was frequency modulated at 500 Hz to a depth of 5 MHz peak-to-peak and stabilized via a first derivative lock after subtracting off the intensity noise and linear absorption in the manner already described. Frequent readjustment of the differential gain and lock-in offsets randomized the residual error from the linear absorption and contributed significantly to the scatter of the interferometric measurements. A third derivative lock was not used in this instance because the large modulation depth required for ~20 MHz linewidths would have presented problems to interferometer operation. A second derivative signal was also detected via another lock-in amplifier to check that the laser frequency remained in lock.

The mean tellurium cell "cold point" temperature under normal operation was 625(±6)°C, which corresponds to a tellurium vapour pressure of 1.30 kPa [12]. The normal saturating power of 6 mW corresponded to an axial power density of 6×10^4 Wm^{-2}.

4. Interferometric frequency ratio measurements

Preliminary frequency measurements of the dye laser stabilized at 486 nm to the chosen tellurium components were made using an NPL-designed wavemeter [13]. This was modified with a phase-locked-loop to flywheel over possible dye laser "drop out" periods due to air bubbles in the dye jet. The estimated uncertainty of these measurements was ±5 in 10^8 (30 MHz). This was within the accuracy necessary to determine unambigously the correct order number at 486 nm for the 1-m evacuated Fabry-Perot interferometer (150 MHz free spectral range). The stabilized light was transmitted to this remote interferometer via a multi-mode graded index optical fibre. An acousto-optic modulator (not shown in fig. 1) was used to prevent scattered light from the fibre back-coupling to the dye laser.

The stabilized dye laser frequencies, when locked to the transitions marked b_1 and b_2 in fig. 2, were determined by interferometric comparison with the 633 nm light from a He-Ne laser stabilized to component "i" of the 11-5 R(127) transition in $^{127}I_2$. This iodine-stabilized laser was an NPL reference laser, and it was operated under the preferred reference conditions [14]. It has a resettability of about 1 part in 10^{11}, and its frequency is within 4×10^{-11} of the mean of a number of lasers from other national laboratories with which it has been compared. The 1-m Fabry-Perot interferometer system and its operating characteristics have been described in earlier publications [15–17]. The frequency modulation of the dye laser (5 MHz peak-to-peak) that was necessary for stabilization was sufficient to cause appreciable broadening of the Fabry-Perot interference rings. This effect was cancelled by modulating the etalon length in synchronism, with carefully adjusted amplitude and phase. The 633-nm laser that was locked to the etalon, was similarly modulated in frequency so as to match the etalon modulation and give an unbroadened interference pattern.

Comparative measurements were carried out over a period of 10 days, during which fifteen independent frequency determinations were made for each of the two radiations. The statistical variations were significantly greater than those previously observed with this interferometer, implying that the resettability of the frequency lock to the tellurium cell contributed a standard deviation of 2 parts in 10^{10}. The frequency ratio results for the tellurium cell, with a 625°C cold-point, were:

$$f(b_1)/f_i = 1.302\ 075\ 4917 \times (1 \pm 2 \times 10^{-10}) ,$$

$$f(b_2)/f_i = 1.301\ 727\ 1874 \times (1 \pm 2 \times 10^{-10}) .$$

The uncertainties of these values correspond to the estimated standard deviation, as detailed in table 1. The most significant contribution to the uncertainty arose from the correction for the phase shift at the etalon plates, which was determined by extrapolation from previous measurements. These measurements comprised 9 values between 514 nm and 670 nm which fitted a cubic curve with an rms error corresponding to only 5 parts in 10^{11} frequency uncertainty. The assigned error is due mainly to the difference in the extrapolation to 486 nm by means of exponential or 4th order polynomial curves, which fitted the 9 data values almost equally well as did the cubic curve.

By combining the above ratio measurements with the currently accepted frequency value [14] of the 633 nm laser (under its reference operating conditions) of 473 612 214.8 MHz, with a relative standard deviation of 3.4×10^{-10}, the following frequency values may be calculated for this tellurium cell with a 625°C cold point:

$$f(b_1) = 616\ 678\ 857.5 \pm 0.25\ \text{MHz} ,$$

$$f(b_2) = 616\ 513\ 896.3 \pm 0.25\ \text{MHz} ,$$

where the uncertainties quoted correspond to the estimated standard deviations.

The most significant factor affecting the stabilized frequency values is the vapour pressure of the tellurium. Fig. 3 shows the observed change of locked frequency for the b_1 component, as a function of vapour pressure [12], when the cold point temperature was raised to 722°C. The gradient of the fitted line is 0.31 ± 0.03 MHz/kPa, where the uncertainty is due mainly to the temperature uncertainty.

It is possible that the stabilized frequency value could be dependent on the amplitude of the frequency modulation, due, for example, to the unlikely overlap of a weak, underlying transition. The signal-to-noise ratio limited the ability to measure any asymmetry in the first derivative discriminant, which would have enabled this effect to be determined. Thus only

Table 1
Frequency ratio measurement uncertainties

Source of uncertainty	Standard deviation ($\times 10^{-11}$)
Observation statistics	8
Phase shift extrapolation	16
Flatness and illumination	3
Prismatic imbalance	6
Diffraction effects	2
Servo errors	2
Cell temperature	7
633 nm reproducibility	4
Total (root sum of squares)	21

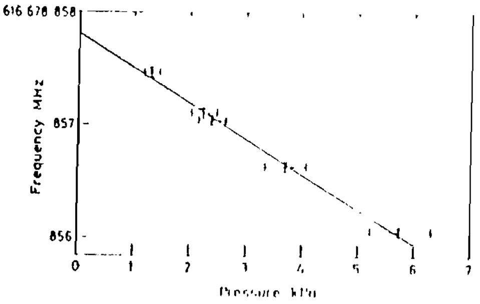

Fig. 3. Pressure shift of the b_1 component. The error bars on the pressure axis correspond to the systematic temperature uncertainty; those on the frequency axis correspond to the relative uncertainty of the observations, and omit the contribution in respect of the absolute frequency calibration.

Appendix D.

an upper limit estimate, of 50 kHz shift per MHz of modulation, could be made, and a modulation amplitude within 1 MHz of that used here is recommended in subsequent experiments.

The variation of the stabilized frequency with saturating power level was investigated by measurements with the power alternated between 3 mW and 9 mW. The difference corresponded to 9×10^{-11} of the frequency, the lower power giving the higher frequency value. However, the result was not statistically significant. Also, any frequency shift due to stray magnetic field was estimated to be less than 2×10^{-11} of the laser frequency.

Ultimately, serious consideration of frequency shifts due to possible foreign gas contaminants in the cell needs to be made. This is especially significant for the comparison of laser frequencies stabilized to different tellurium cells. A method of linewidth assessment such as one used to determine the purity of iodine cells [18] is clearly desirable.

In conclusion, the frequencies of a dye laser stabilized to certain saturated components in $^{130}Te_2$ at 486 nm, under particular operating conditions, have been measured to an accuracy of 4 parts in 10^{10} (one standard deviation). Such Doppler-free tellurium spectra can now be used as known reference frequencies in the absolute frequency measurement of the two-photon 1S–2S transitions in hydrogen and deuterium.

Acknowledgements

The authors would like to thank Dr. B.W. Petley for his encouragement of the work, and his critical reading of the manuscript. The financial support of the SERC is gratefully acknowledged. J.R.M.B. and J.M.G. would like to acknowledge SERC and SERC CASE studentships respectively.

References

[1] S.A. Lee, R. Wallenstein and T.W. Hänsch, Phys. Rev. Lett. 35 (1975) 1262.

[2] C. Wieman and T.W. Hänsch, Phys. Rev. A22 (1980) 192.

[3] T.W. Hänsch, M.H. Nayfeh, S.A. Lee, S.M. Curry and I.S. Shanin, Phys. Rev. Lett. 32 (1974) 1336.

[4] J.E.M. Goldsmith, E.W. Weber and T.W. Hänsch, Phys. Rev. Lett. 41 (1978) 1525.

[5] B.W. Petley, K. Morris and R.E. Shawyer, J. Phys. B: Atom. Molec. Phys. 13 (1980) 3099.

[6] R. Amin, C.D. Caldwell and W. Lichten, Phys. Rev. Lett. 47 (1981) 1234.

[7] J. Cariou and P. Luc, Atlas du spectre d'absorption de la molecule de tellure, Lab. Aime-Cotton C.N.R.S., Orsay, France (1980).

[8] T.J. Stone and R.F. Barrow, Can. J. Phys. 53 (1975) 1976.

[9] S. Chu and A.P. Mills Jr., Phys. Rev. Lett. 52 (1984) 1689.

[10] Opthos Instruments Inc., Maryland, MD 20855, USA.

[11] G.R. Hanes and C.E. Dahlstrom, Appl. Phys. Lett. 14 (1969) 362.

[12] R.E. Honig and D.A. Kramer, RCA Review 30 (1969) 285.

[13] S.J. Bennett and P. Gill, J. Phys. E: Sci. Instrum. 13 (1980) 174.

[14] Metrologia 19 (1984) 163.

[15] P.T. Woods, K.C. Shotton and W.R.C. Rowley, Appl. Optics 17 (1978) 1048.

[16] G.P. Barwood and W.R.C. Rowley, Metrologia 20 (1984) 19.

[17] G.P. Barwood, W.R.C. Rowley and P.T. Woods, Metrologia 20 (1984) 157.

[18] W.R.C. Rowley and B.R. Marx, Metrologia 17 (1981) 65.

Appendix D.

VOLUME 56, NUMBER 6 PHYSICAL REVIEW LETTERS 10 FEBRUARY 1986

Interferometric Measurement of the $1S_{1/2}$-$2S_{1/2}$ Transition Frequency in Atomic Hydrogen

J. R. M. Barr,(a) J. M. Girkin,(b) J. M. Tolchard, and A. I. Ferguson
Department of Physics, University of Southampton, Southampton S09 5NH, United Kingdom

(Received 24 October 1985)

The $1S_{1/2}$-$2S_{1/2}$ transition frequency in atomic hydrogen has been interferometrically measured by comparison with a reference line in $^{130}Te_2$ by Doppler-free two-photon laser spectroscopy. The measured $1S_{1/2}$-$2S_{1/2}$ transition frequency of 2 466 061 397(25) MHz is in good agreement with the theoretical predictions of Erickson modified to take account of recent measurements of the Rydberg constant. This measurement can be used to deduce a value for the ground-state Lamb shift and gives the result of 8182(25) MHz which compares with a value of 8173.248(81) MHz predicted by Erickson.

PACS numbers: 32.30.Jc, 06.20.Jr

In recent years atomic hydrogen has attracted the attention of laser spectroscopists in a number of experiments designed to measure fundamental constants[1-5] or to test theoretical calculations.[6] These experiments have been motivated by the existence of highly accurate theoretical calculations[7-9] and the development of new nonlinear laser-spectroscopic techniques which may enable discrepancies between these theoretical predictions to be tested. The wavelength of the Balmer-α transition has been determined many times[1-3] by Doppler-free techniques with the aim of measuring the Rydberg constant (R_∞). Although excellent accuracies were achieved (1 part in 10^9), the experimental resolution was limited to approximately 50 MHz. Narrower linewidths (~ 2 MHz) are expected to be achieved by use of double-quantum excitation of the $2S_{1/2}$-$3S_{1/2}$ transition[4] or two-photon excitation of the $2S_{1/2}$-$8S_{1/2}$, $8D_{3/2,5/2}$ transitions.[5] Previous investigations of the $1S_{1/2}$-$2S_{1/2}$ transition[6] have concentrated on measuring the ground-state Lamb shift by interferometrically comparing one quarter of the $1S_{1/2}$-$2S_{1/2}$ frequency with one of several Balmer-β components. In these experiments the ground-state Lamb shift was measured to an accuracy of 0.4%; however, no attempt to measure the transition energy of the lines involved was reported. In this Letter we report what we believe to be the first measurement of the absolute transition frequency of the $1S_{1/2}$-$2S_{1/2}$ transition in atomic hydrogen by Doppler-free techniques. If the current best value for the Rydberg constant is used to predict the $1S_{1/2}$-$2S_{1/2}$ energy separation, the measurement reported here can be interpreted as a measurement of the difference in Lamb shifts for the $1S_{1/2}$ and $2S_{1/2}$ levels. This can then be used to deduce a value for the ground-state Lamb shift. We refer to Lamb shifts as any correction, other than hyperfine structure and reduced-mass effects, which has to be applied to the Dirac expression for the hydrogen energy levels. If it is assumed that the theoretical predictions are correct, this measurement can be used as a measurement of the Rydberg constant. As such it is the first laser-spectroscopic measurement of the Rydberg constant on any transition other than Balmer-α. Further extensions of the techniques reported here will make possible improved measurements of the Rydberg constant, and may enable the ground-state Lamb shift to be measured to an accuracy which will distinguish between the different theoretical predictions.

The $1S_{1/2}$-$2S_{1/2}$ transition frequency has been measured by interferometrically comparing one quarter of the $1S_{1/2}$-$2S_{1/2}$ transition frequency with a reference line in $^{130}Te_2$ vapor which was previously calibrated by Doppler-free saturation spectroscopy to an absolute accuracy of 4 parts in 10^{10}.[10] The experimental system used in this measurement consisted of a coumarin 102 (C102) continuous-wave (cw) dye laser (Coherent 699-21), used in a standing-wave configuration. This laser was pumped by the violet lines of a krypton-ion laser (Coherent 3000K) and typically provided 10-70 mW in a 1-2-MHz linewidth near 486 nm. All frequency measurements were made in the blue so that the measured frequencies and hyperfine separations appeared to be one quarter of the atomic value.

The relative frequency calibration was provided by the transmission fringes of a confocal interferometer with a quartz spacer and a measured free spectral range of 497.96(10) MHz. The interferometer temperature was actively stabilized to ± 0.01 °C and was placed inside a second enclosure which was temperature stabilized to ± 0.5 °C. The residual drift of the interferometer frequency was less than 20 MHz/h. The aluminum mirror coatings gave rise to a correction for the phase shift on reflection of less than 1 kHz near 486 nm for the tuning range used in these experiments.[11] Dispersion of air could be neglected since the interferometer was evacuated to 10^{-6} Torr and sealed off. A Doppler-free saturated-absorption experiment on $^{130}Te_2$ vapor enabled the absolute frequency to be determined under experimental conditions described by Barr *et al.*[10] In order to prevent optical feedback an acousto-optic modulator (Isomet) was inserted between the dye laser and the saturation spectrometer.

VOLUME 56, NUMBER 6 PHYSICAL REVIEW LETTERS 10 FEBRUARY 1986

This shifted up the light used for this part of the experiment by 80.00 MHz.

The tunable 243-nm light required to excite the $1S_{1/2}$-$2S_{1/2}$ transition was generated by frequency doubling of the 486-nm radiation. In order to increase the doubling efficiency the low-power cw radiation was amplified with a pulsed, single-pass, four-stage, traveling-wave C102 dye amplifier pumped by a frequency-tripled Nd-doped yttrium-aluminum-garnet laser (Quanta Ray DCR 2). The output was 1.0–1.5 mJ in a 5-ns pulse with a 150–200-MHz linewidth which is approximately 2–2.5 times the Fourier-transform limit. The amplification process not only broadened the linewidth but also shifted the pulse spectrum up relative to the cw laser by 35–55 MHz due to pulse chirping.[6] This was observed with a confocal interferometer of 300-MHz free spectral range and 2-MHz linewidth.

Frequency doubling in urea (Quantum Technology 8×8×8 mm^3) yielded up to 0.2 mJ at 243 nm. This was sufficient to enable the laser linewidth to be reduced by filtering with a confocal interferometer. The interferometer was 25 cm long with a mirror reflectivity of 90%. The linewidth was measured to be 25 MHz by use of a narrow-linewidth cw dye laser. A transmission maximum of the interferometer was maintained coincident with the cw-laser frequency by modulation of the interferometer length and use of standard first-derivative locking techniques. The length was modulated at 600 Hz over a length change corresponding to 7 MHz which broadened the linewidth of the interferometer to 30 MHz. The average interferometer pass-band frequency was locked to the cw frequency to better than 5×10^{-3} of the interferometer linewidth. The pulsed blue light was mode matched into the interferometer giving a free spectral range of 600 MHz. For mode matching, the interferometer must be aligned with its optic axis parallel to the laser beam to a measured angle of less than $\pm5\times10^{-4}$ rad. As the cw light and the pulsed light could be mode matched simultaneously, the angle between them must have been smaller than this limit. Consequently the difference in resonance frequency between the cw and pulsed light due to alignment effects could be made negligibly small. However, the frequency spectrum of the transmitted pulsed light was found to have a linewidth of 35–40 MHz and to be shifted up by 12.3(5.2) MHz relative to the cw frequency. This is related to the amplifier shift since the frequency spectrum of the light being filtered had a nonzero gradient at the cw frequency. The filtering process stretched the pulse length from 5 to 12 ns and changed the temporal profile from a Gaussian to a single-sided exponential. The peak power was reduced from 260 to 10 kW. High conversion to the uv was maintained by focusing to a beam radius of 50 μm in the urea crystal, yielding up to 20 μJ with a pulse duration of 6 ns.

Molecular hydrogen was obtained by electrolysis of a weak NaOH solution. Dissociation of H_2 was achieved in a microwave discharge (Microtron 200) with typical microwave powers of 6–10 W. The observation cell (50 mm×25 mm diameter) was equipped with Spectrosil windows and two plane-parallel stainless-steel ionization detection plates (10×50 mm^2) separated by 15 mm. The pressure in the cell was monitored with a capacitive manometer (Baratron 222BA) and was varied in the region 0.1–1.5 Torr. Most measurements were taken at a pressure of 0.18 Torr. In recent high-resolution experiments, atomic beams have been used to avoid broadening and shifts due to discharge electric fields and pressure effects.[3,4] For the pressures and resolution used in this experiment it was found that the pressure shifts were negligible and so an atomic beam was not used.

The 243-nm light was focused onto a mirror 1–2 cm behind the cell with a 10-cm focal length fused-silica lens and a 15-cm focal length cylindrical fused-silica lens. The latter compensated for the distorted uv beam profile caused by walkoff in the doubling crystal. The spot radius of the uv was 100 μm and energies in the range 0.7–3 μJ were used. The ions produced by Doppler-free two-photon–resonant three-photon ionization were collected by a small electric field (5 V cm^{-1}) between the metal plates. The Stark shift caused by this field can be calculated to be less than 8 kHz.[12] The collected current was amplified by a detector with a sensitivity of 13 V pC^{-1} and a noise level corresponding to 10^4 electrons/pulse. Typical signal levels were several volts corresponding to the production of 10^6 electron-proton pairs per pulse.

The spectra shown in Fig. 1 were obtained by scanning the dye laser over a 2-GHz interval in 200 s. The

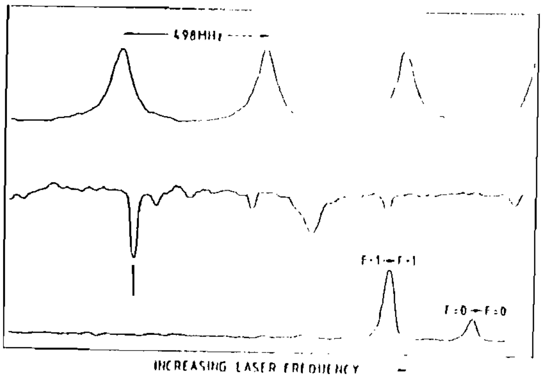

FIG. 1. A typical series of spectra. The top trace shows the interferometer fringes used as frequency markers. The middle trace shows a portion of the $^{130}Te_2$ spectrum, where the intermediate transition used as a transfer line is indicated by an arrow. The bottom trace shows the hydrogen $1S_{1/2}$-$2S_{1/2}$ spectrum.

data from the pulsed part of the experiment were collected on a pulse-to-pulse basis with no averaging while the data from the saturation spectrometer were smoothed by the 0.1-s time constant on a phase-sensitive detector. The confocal filter could only be locked over a limited scan range and so it was convenient to use another $^{130}Te_2$ line as a transfer standard.

The data were analyzed as follows. The centers of the interferometer peaks were found on the computer by numerical differentiation of data which had been smoothed by the carrying out of a moving average over thirty points. The zero crossing gave the positions of the extrema. For the hydrogen data and the $^{130}Te_2$ data the smoothing was over ten points. Only in the case of the hydrogen data did varying of the number of points cause a change in the centroid of each component. However, the shift was smaller than the statistical uncertainties and could be neglected. The separations of the various lines were found in terms of the reference interferometer by interpolation. It was found that small nonlinearities in the laser scan produced slight variations in the interferometer peak separations which required a quadratic fit to be taken into account. The success of this correction was observed by our measuring the known hyperfine splitting in hydrogen and ensuring that it was within the experimental error of the accepted value. The magnitude of the correction was about ±1% of the interferometer free spectral range. Eleven scans were used to obtain the separation between the calibrated $^{130}Te_2$ line and the transfer line with use of the cw laser. The transfer line was found to be 549.1(1.7) MHz higher in frequency than the calibrated line. Thirty scans were used to obtain the $^{130}Te_2$ line to H $F=1\rightarrow 1$ hyperfine-component separation.

To arrive at the final energy measurement several corrections have to be taken into account. These are shown in Table I and are explained as follows, where all corrections are applied in terms of the frequency scale of the 486-nm radiation.

(1) The amplifier shift was measured at the start and finish of each sequence of spectra and used to correct the average value of the separation between the transfer $^{130}Te_2$ line and the H $F=1\rightarrow 1$ hyperfine component. The error of 5.9 MHz represents one standard deviation and includes the uncertainty of the amplifier shift (5.2 MHz) and statistical uncertainties (2.8 MHz).

(2) +77.678 MHz is the separation between the $F=1\rightarrow 1$ hyperfine component and the centroid of the hyperfine levels.

(3) −80.00 MHz comes from the frequency shift caused by the acousto-optic modulator.

(4) The pressure shift was monitored over the range 0.2–1.5 Torr. The measured shift was +3(6) MHz/Torr to higher frequencies. Hence a correction of −0.6(1.2) MHz at the operating pressure of 0.2 Torr is included.

TABLE I. Theoretical predictions of the $1S_{1/2}$-$2S_{1/2}$ energy separation using the calculations of Erickson (Ref. 7) modified by use of the weighted mean value of the Rydberg constant [see Taylor (Ref. 13)] together with the predicted $1S_{1/2}$ Lamb shift. The measured frequencies and corrections to these frequencies are also shown in the table, and refer to the visible laser frequency. The final $1S_{1/2}$ to $2S_{1/2}$ transition frequency is 4 times the laser frequency. All values are in megahertz.

Theory	
Dirac contribution	−2 467 411 574.203
Reduced mass	1 343 062.867
Nuclear recoil	−22.325
$1S_{1/2}$ Lamb shift	8173.248(81)
$1S_{1/2}$-$2S_{1/2}$ frequency	2 466 061 405.5(2.9)
Experiment	
Calibrated $^{130}Te_2$ frequency[a]	616 513 896.30(25)
Intermediate $^{130}Te_2$ offset	+549.1(1.7)
$^{130}Te_2-H(F=1\rightarrow 1)$	+907.4(5.9)
$H(F=1\rightarrow 1)$, centroid	+77.678
Acousto-optic shift	80.00
Pressure shift	−0.6(1.2)
ac Stark shift	−0.6(0.6)
Interferometer free spectral range	0.0(0.1)
Total	616 515 349.3(6.3)
Measured $1S_{1/2}$-$2S_{1/2}$ frequency	2 466 061 397(25)
Deduced $1S_{1/2}$ Lamb shift	8182(25)

[a] Reference 8.

(5) The ac stark shift can be calculated[6] to be 0.6(0.2) MHz, and increases the separation between the levels. This shift was below the resolution of this experiment and is included as a correction of −0.6(0.6) MHz.

The predicted value of the $1S_{1/2}$-$2S_{1/2}$ transition frequency is a sensitive function of the assumed value of the Rydberg constant. There have been several recent measurements of the Rydberg constant. These are shown in Table II where the data have been modified to take account of changes in these measurements due to the redefinition of the meter, small changes in the fine-structure constant, and the electron-to-proton mass ratio.[13] The prediction of the Erickson[7] theory for the $1S_{1/2}$ to $2S_{1/2}$ transition frequency using these values for the Rydberg constant is also shown in Table II together with our experimental measurement of this transition frequency.

If the Dirac and relativistic nuclear-recoil contributions calculated with the weighted mean value of the Rydberg constant in Table II are subtracted from the measured value of the $1S_{1/2}$-$2S_{1/2}$ transition frequency a value of 7137(25) MHz is obtained for the difference

TABLE II. Comparison of some recently measured values of the Rydberg constant adjusted by Taylor (Ref. 13) together with the weighted mean. The resulting $1S_{1/2}$ to $2S_{1/2}$ transition frequency based on Erickson's theory is also shown. Our experimental measurement of this frequency and the Rydberg constant are shown for comparison. The tabulated quantities are $\Delta R := R_\infty - 10\,973\,731$ m^{-1} and $\Delta E := E_{1S\text{-}2S} - 2\,466\,061\,000$ MHz.

	ΔE	ΔR
Goldsmith *et al.*[a]	0.500(32)	397.8(7.2)
Petley *et al.*[b]	0.521(64)	402.6(14.4)
Amin *et al.*[c]	0.539(12)	406.6(2.7)
Weighted mean[d]	0.534(13)	405.5(2.9)
This work	0.50(11)	397(25)

[a] Reference 1.
[b] Reference 2.
[c] Reference 3.
[d] Reference 13.

in $1S_{1/2}$ and $2S_{1/2}$ Lamb shifts. This compares with a theoretical value of 7128.171(81) MHz predicted by Erickson.[7] If the theoretical value for the $2S_{1/2}$ Lamb shift predicted by Erickson (excluding recoil) of 1045.077(0.010) MHz is accepted then we obtain an experimental value for the ground-state Lamb shift of 8182(25) MHz compared with a theoretical value of 8173.248(81) MHz.

An alternative interpretation of this experiment is that it is a measurement of the Rydberg constant. As such it is the first measurement of this important constant in a transition other than Balmer-α. The present work gives a value for the Rydberg constant of 10 973 731.50(11) m^{-1} which is consistent with other measurements but with a somewhat larger uncertainty.

The methods described in this paper offer a potential for significant improvements in the measurement of the Rydberg constant and the Lamb shifts in atomic hydrogen. The principal uncertainties are due to linewidths of the resonances obtained and uncertainties in the frequency shift between the cw dye laser and the amplified beam. Both of these problems could be reduced by reducing the linewidth of the filter interferometer. We estimate that the linewidth could be realistically reduced to the region of 3 MHz without significant loss of signal-to-noise ratio. We would then expect the accuracy of our measurements to improve to about 300 kHz. At this level of accuracy an improved measurement of the Rydberg constant should prove possible. This will make an interesting test of systematic errors since all other accurate measurements of the Rydberg constant have been on Balmer-α. It should also be possible to make an improved measurement of the $1S_{1/2}$ Lamb shift by comparing the $1S_{1/2}$-$2S_{1/2}$ transition frequency directly with a component in Balmer-β. A metastable beam suitable for making this measurement has been constructed in our laboratory. This next generation of experiment may enable the differences between the Erickson,[7] Mohr,[8] and Sapirstein[9] theories, which amount to about 300 kHz in the ground-state Lamb shift, to be tested.

The authors gratefully acknowledge the support of Science and Engineering Research Council for this work in the form of research grants, an Advanced Fellowship (A.I.F.), research studentships (J.R.M.B., J.M.T.), and a CASE studentship (J.M.G.) in conjunction with the National Physical Laboratory. We also thank Dr. B. W. Petley for many useful discussions.

(a) Present address: Central Laser Facility, Rutherford Appleton Laboratory, Oxford, United Kingdom.

(b) Present address: Photon Control Limited, Cambridge, United Kingdom.

[1] J. E. M. Goldsmith, E. W. Weber, and T. W. Hänsch, Phys. Rev. Lett. 41, 1525 (1978).

[2] B. W. Petley, K. Morris, and R. E. Schawyer, J. Phys. B **13**, 3099 (1980).

[3] S. R. Amin, C. D. Caldwell, and W. Lichten, Phys. Rev. Lett. **18**, 1234 (1981).

[4] D. Shiner and C. Wieman, in *Precision Measurement and Fundamental Constants II*, edited by B. N. Taylor and W. D. Phillips, National Bureau of Standards Special Publication No. 617 (U.S. GPO, Washington, D.C., 1984), p. 123.

[5] F. Biraben and L. Julien, Opt. Commun. 53, 319 (1985).

[6] C. Wieman and T. W. Hänsch, Phys. Rev. A 22, 192 (1980).

[7] G. W. Erickson, J. Phys. Chem. Ref. Data 6, 831 (1977).

[8] P. J. Mohr, Ann. Phys. (N.Y.) 88, 52 (1974).

[9] J. Sapirstein, Phys. Rev. Lett. 47, 1723 (1981).

[10] J. R. M. Barr, J. M. Girkin, A. I. Ferguson, G. P. Barwood, P. Gill, W. R. C. Rowley, and R. C. Thomson, Opt. Commun. 59, 217 (1985).

[11] J. M. Bennet, J. Opt. Soc. Am. 54, 612 (1964).

[12] J. A. Blackman and G. W. Series, J. Phys. B 6, 1090 (1973).

[13] B. N. Taylor, private communication of work carried out in connection with the 1985 least squares adjustment of the fundamental constants. Other values used are $\alpha^{-1} = 137.035\,988(<10)$ and $m_p/m_e = 1836.152\,701(37)$.